

# Numerička analiza točkastih zavora u tankostijenim konstrukcijama izloženim mehaničkom šoku i vibracijskim opterećenjima

---

Vrgoč, Ana

Master's thesis / Diplomski rad

2019

*Degree Grantor / Ustanova koja je dodijelila akademski / stručni stupanj:* **University of Zagreb, Faculty of Mechanical Engineering and Naval Architecture / Sveučilište u Zagrebu, Fakultet strojarstva i brodogradnje**

*Permanent link / Trajna poveznica:* <https://urn.nsk.hr/urn:nbn:hr:235:426661>

*Rights / Prava:* [In copyright](#) / [Zaštićeno autorskim pravom.](#)

*Download date / Datum preuzimanja:* **2024-04-23**

*Repository / Repozitorij:*

[Repository of Faculty of Mechanical Engineering and Naval Architecture University of Zagreb](#)



UNIVERSITY OF ZAGREB  
FACULTY OF MECHANICAL ENGINEERING AND NAVAL  
ARCHITECTURE

# **MASTER'S THESIS**

**Ana Vrgoč**

Zagreb, 2019

UNIVERSITY OF ZAGREB  
FACULTY OF MECHANICAL ENGINEERING AND NAVAL  
ARCHITECTURE

# **MASTER'S THESIS**

**NUMERICAL ANALYSIS OF SPOT WELDS IN SHEET METAL  
STRUCTURES EXPOSED TO MECHANICAL SHOCK AND VIBRATION  
LOADING**

Mentor:

Full Prof. Zdenko Tonković, PhD

Student:

Ana Vrgoč

Zagreb, 2019

## IZJAVA

*Pod punom moralnom odgovornošću izjavljujem da sam ovaj rad izradila samostalno, koristeći se znanjem stečenim tijekom studija te navedenom literaturom.*

## STATEMENT

*I hereby declare that this thesis is entirely the result of my own work. The research has been conducted employing the knowledge obtained during my undergraduate and graduate studies, except where otherwise indicated. All used sources are given in the list of referenced literature.*

# ACKNOWLEDGMENT

*Foremost, I would like to express my deepest gratitude and thanks to my Thesis supervisor, Prof. DSc. Zdenko Tonković, for the guidance, support, encouragement and suggestions he generously offered not only during the research phase, but also throughout my entire graduate studies.*

*Secondly, I would like to thank MPhil Nikola Naranča for granting me the opportunity to write this thesis in collaboration with companies AVL-AST d.o.o and AVL List GmbH.*

*Further, my sincere appreciation goes to MSc Roman Baranja for his enormous effort, guidance and daily discussions, which helped me resolve many of the theoretical and numerical issues I have stumbled upon. Most importantly, I would like to thank Roman for the patience he showed and the encouragement and support he offered during the thesis work period.*

*A very special thanks goes to MSc Damjan Čakmak for being a true friend in need and friend indeed. Damjan, thank you for your valuable advice, long discussions (which helped me not only in research, but in life as well) and for finding time to review my thesis. Finally, thank you for the moral support, especially in the final period of thesis writing.*

*I would also like to extend my gratitude to my best friends Dejan-Josip Tretnjak and Martina Šimag. Dejan, thank you for always being by my side for the past 10 years. Martina, thank you for your constant support and encouragement and for teaching me how to always look on the bright side of life.*

*My enormous thanks goes to my closest friends Petra Adamović and Andrija Zaplatić for unconditional support, for believing in me and always lifting my spirits.*

*To Boris and Sonja, thank You for Your unselfish support and kindness You provided during my studies. You put my needs in front of Yours and provided the calm environment I needed to study.*

*My very special thanks goes to my parents, Mirjana and Zoran, to my brothers, Bruno, Sven and Niko, and to my sister Kaja-Pavla. You have been there for me my entire life, helping and guiding me and always wishing me all the happiness in the world. I would not be here without you!*

*And last, but not least...My enormous thanks goes to my boyfriend Bojan. For the past six years, you showed me unconditional support, encouragement and patience. Thank you for always believing in me, although at times it was hard. During my studies and especially during the period of thesis work, you have always motivated me to work even harder. Bojan, "you have, that is, let it go and even encouraged my devotion to it...I do not know how to give you thanks." (Thomas S. Kuhn, The Structure of scientific revolutions)  
I dedicate this thesis to my sister Kaja-Pavla.*

*Ana Vrgoč*



SVEUČILIŠTE U ZAGREBU  
FAKULTET STROJARSTVA I BRODOGRADNJE



Središnje povjerenstvo za završne i diplomske ispite  
Povjerenstvo za diplomske ispite studija strojarstva za smjerove:  
procesno-energetski, konstrukcijski, brodstrojarski i inženjersko modeliranje i računalne simulacije

Sveučilište u Zagrebu Fakultet strojarstva i brodogradnje	
Datum: 1. 03. 2019.	Prilog
Klasa: 02-01/19-013	
Ur.broj: 15-1703-19-182	

## DIPLOMSKI ZADATAK

Student: Ana Vrgoč

Mat. br.: 0035196045

Naslov rada na  
hrvatskom jeziku:

**Numerička analiza točkastih zavara u tankostijenim konstrukcijama  
izloženim mehaničkom šoku i vibracijskim opterećenjima**

Naslov rada na  
engleskom jeziku:

**Numerical Analysis of Spot Welds in Sheet Metal Structures Exposed  
to Mechanical Shock and Vibration Loading**

Opis zadatka:

Spot weld technology is present in automobile manufacturing industry for many years. It is a process in which the contacting sheet metal surfaces are joined together by the heat obtained from resistance to electric current. In the past, the process was mainly used for building the body of the car, with automated industrial robots found on the assembly lines. Nowadays, with the strong growing development of the hybrid and electric powertrains, spot welds are widely used in the battery pack assemblies and power electronic components carriers, attached to the body of a car. These components are exposed to shock loads (mechanical shock, e.g. crash, foreign object impact) and vibrational loads (harmonic or random, e.g. road excitation) during the development and testing phase. The applied loads are designed to simulate and predict vehicle real life conditions. Therefore, it is crucial to understand damage and failure mechanisms of the components and joints for successful life prediction.

This master thesis will focus on the spot welds evaluation methods and criteria in vehicle powertrain applications. Based on everything said above in this study it is necessary to:

1. Study available literature on the finite element modeling of spot welds, spot weld damage mechanisms and spot weld fatigue.
2. Investigate available finite element methods and tools for the spot weld fatigue analysis (e.g. FEMFAT SPOT and nCode DesignLife).
3. Investigate finite element procedures for the quasi-static spot weld damage analysis.
4. Apply studied spot weld analysis procedures and compare to the experimental results.

During thesis preparation one must comply with the standard rules for preparation of master thesis. It is necessary to list all literature used and received assistance.

Zadatak zadan:

17. siječnja 2019.

Rok predaje rada:

21. ožujka 2019.

Predviđeni datumi obrane:

27., 28. i 29. ožujka 2019.

Zadatak zadao:

Prof. dr. sc. Zdenko Tonković

Predsjednica Povjerenstva:

Prof. dr. sc. Tanja Jurčević Lulić

# Contents

<b>Contents</b>	<b>II</b>
<b>List of Figures</b>	<b>V</b>
<b>List of Tables</b>	<b>VII</b>
<b>List of Symbols and Units</b>	<b>IX</b>
<b>List of Abbreviations</b>	<b>X</b>
<b>Sažetak (Abstract in Croatian)</b>	<b>XI</b>
<b>Abstract</b>	<b>XII</b>
<b>Prosireni sažetak</b>	<b>XIII</b>
<b>1 Introduction</b>	<b>1</b>
1.1 Motivation . . . . .	3
1.2 Thesis structure overview . . . . .	3
<b>2 Fatigue of spot welded joints</b>	<b>4</b>
2.1 Introduction . . . . .	4
2.2 Experimental evaluation of the fatigue behavior of spot welded specimens [14]	5
2.3 Numerical methods for spot weld fatigue life assessment . . . . .	9
2.3.1 Rupp/LBF method [18, 19] . . . . .	9
2.3.2 Force-based spot fatigue life prediction based on [21] . . . . .	14
<b>3 Fatigue life assessment of spot-welded specimens using finite element analysis</b>	<b>18</b>
3.1 Effect of weld geometry and sheet thickness on fatigue life of spot-welded specimens . . . . .	25
3.2 Conclusions . . . . .	27
<b>4 Random vibration fatigue analysis</b>	<b>29</b>
4.1 Introduction . . . . .	29

4.2	Signal processing . . . . .	30
4.3	Random vibration fatigue analysis . . . . .	32
4.4	Random vibration fatigue of spot welds using <i>nCode DesignLife</i> . . . . .	37
<b>5</b>	<b>Damage analysis of spot welded joints</b>	<b>41</b>
5.1	Introduction . . . . .	41
5.2	Spot weld failure modeling . . . . .	43
5.3	Quasi-static analysis using <i>Abaqus/Explicit</i> [41] . . . . .	44
5.4	Quasi-static damage analysis of spot-welded specimens based on [71] . . . . .	47
5.4.1	Determination of parameters defining connector element behavior [71]	53
5.5	Numerical results . . . . .	56
5.5.1	Tensile shear specimen . . . . .	57
5.5.2	Coach peel specimen . . . . .	65
<b>6</b>	<b>Conclusions</b>	<b>75</b>
6.1	Summary and main conclusions . . . . .	75
6.1.1	Findings related to research objectives I and II . . . . .	75
6.1.2	Findings related to the research objective III . . . . .	76
6.1.3	Findings related to the research objective IV . . . . .	77
6.2	Recommendations for future work . . . . .	78
	<b>Bibliography</b>	<b>80</b>
<b>A</b>	<b>Appendix: Effect of spot weld model, mesh refinement and mesh alignment on fatigue behavior of spot-welded specimens</b>	<b>86</b>
<b>B</b>	<b>Appendix: Effect of restraint diameter in <i>FEMFAT Spot</i></b>	<b>95</b>



# List of Figures

Figure 1.1:	a) Schematic of spot welding process [1], b) Cycles of spot welding process [2] . . . . .	1
Figure 1.2:	Weld nugget microstructure and hardness distribution [10] . . . . .	2
Figure 2.1:	Spot weld failure modes under cyclic loading [15] . . . . .	4
Figure 2.2:	Spot-welded specimens used for experimental testing [14] . . . . .	6
Figure 2.3:	Effect of base material and load ratio on the fatigue behavior of spot-welded specimens [14] . . . . .	6
Figure 2.4:	Mean stress effect and effect of sheet thickness [14] . . . . .	8
Figure 2.5:	Circular plate model with a rigid kernel at the centre [14] . . . . .	10
Figure 2.6:	Generic $S - N$ curve for failure occurring in steel sheets [19] . . . . .	12
Figure 2.7:	Generic $S - N$ curve for failure through the nugget for spot-welded steel sheets [19] . . . . .	13
Figure 2.8:	Generic aluminum $S - N$ curve [19] . . . . .	13
Figure 2.9:	Forces acting on weld nugget [21] . . . . .	14
Figure 2.10:	Circular plate subjected to $F_z$ and $M_y$ [21] . . . . .	15
Figure 2.11:	Infinite plate subjected to $F_x$ and $M_z$ [21] . . . . .	16
Figure 2.12:	Local loading direction [24] . . . . .	17
Figure 3.1:	Structural elements representing the weld nugget . . . . .	19
Figure 3.2:	Numerical models of tensile shear and coach peel specimen for the force-based fatigue analysis . . . . .	20
Figure 3.3:	Numerical models of tensile shear and coach peel specimen for stress-based fatigue analysis . . . . .	21
Figure 3.4:	HSLA340 . . . . .	22
Figure 3.5:	DP600 . . . . .	22
Figure 3.6:	DP800 . . . . .	23
Figure 3.7:	Comparison between the numerical results and the experimental data [14] . . . . .	23
Figure 3.8:	Comparison between the experimental [14] and numerical results obtained with <i>FEMFAT Spot</i> . . . . .	24
Figure 3.9:	Effect of base material on fatigue life of spot-welded specimens using force-based approach implemented in <i>FEMFAT Spot</i> . . . . .	24

Figure 3.10:	The effect of nugget diameter on the fatigue life of spot-welded specimens- <i>nCode DesignLife</i> . . . . .	25
Figure 3.11:	Interfacial failure - <i>nCode DesignLife</i> . . . . .	26
Figure 3.12:	Effect of sheet thickness on the fatigue life of spot-welded specimens . .	26
Figure 3.13:	Interfacial failure - <i>nCode DesignLife</i> . . . . .	26
Figure 4.1:	Signal classification [33] . . . . .	30
Figure 4.2:	Time domain waveform and probability density function of random excitation [35] . . . . .	30
Figure 4.3:	Calculation of spectral moments [44] . . . . .	34
Figure 4.4:	Comparison of narrow band and broad band time signal [19] . . . . .	36
Figure 4.5:	Schematic representation of random vibration fatigue life evaluation procedure of spot-welded structures . . . . .	37
Figure 4.6:	Analysis model . . . . .	38
Figure 4.7:	Input acceleration spectral density . . . . .	38
Figure 4.8:	Location of critical spot weld . . . . .	40
Figure 5.1:	Schematic representation of pullout failure [53] . . . . .	42
Figure 5.2:	Energy absorption during pullout and interfacial failure [54] . . . . .	42
Figure 5.3:	Forces acting on weld nugget [65] . . . . .	43
Figure 5.4:	Energy balance in quasi-static analysis [41] . . . . .	46
Figure 5.5:	Specimen geometry [71] . . . . .	47
Figure 5.6:	Spot weld connection orientation and derived components [72] . . . . .	49
Figure 5.7:	Schematic representation of stiffness degradation upon damage initiation [41] . . . . .	51
Figure 5.8:	Fastener definition [41] . . . . .	52
Figure 5.9:	Structural elements representing spot weld nugget . . . . .	53
Figure 5.10:	Numerical model of tensile shear and coach peel specimens used for quasi- static damage analysis . . . . .	53
Figure 5.11:	Arcan clamping device [71] . . . . .	54
Figure 5.12:	Experimental results obtained with Arcan clamping device [71] . . . . .	54
Figure 5.13:	Schematic representation of an algorithm to define appropriate loading rate, which ensures the quasi-static response . . . . .	56
Figure 5.14:	Tensile shear specimen discretized with S4R element of different size . .	57
Figure 5.15:	First eigenfrequency vs. number of S4R elements . . . . .	58
Figure 5.16:	Energy distribution during the analysis of tensile shear specimen . . . .	59
Figure 5.17:	Stress distribution around the nugget circumference . . . . .	60
Figure 5.18:	Equivalent plastic deformation around the nugget circumference . . . .	60
Figure 5.19:	Reaction force vs. displacement at tension node . . . . .	61
Figure 5.20:	a) Connector equivalent force, b) Connector derived loading components	62
Figure 5.21:	a) Connector equivalent force, b) Connector derived loading component	63

Figure 5.22:	Reaction force vs. displacement at tension node . . . . .	63
Figure 5.23:	Coach peel specimen discretized with S4R element of different size . . .	65
Figure 5.24:	First eigenfrequency vs. number of S4R elements . . . . .	66
Figure 5.25:	Energy distribution during analysis of coach peel specimen . . . . .	67
Figure 5.26:	Stress distribution around the nugget circumference . . . . .	68
Figure 5.27:	Equivalent plastic deformation around the nugget circumference . . . .	68
Figure 5.28:	Reaction force vs. displacement at tension node . . . . .	69
Figure 5.29:	a) Connector equivalent force, b) Connector derived loading component	70
Figure 5.30:	a) Connector equivalent force, b) Connector derived loading component	71
Figure 5.31:	Reaction force vs. displacement at tension node . . . . .	71
Figure 5.32:	Reaction force vs. displacement at tension node . . . . .	73
Figure A.1:	Specimen FE model: Effect of mesh refinement around the nugget perimeter . . . . .	87
Figure A.2:	Specimen FEA model: Rectangular shell element meshes . . . . .	88
Figure A.3:	Specimen FE model: Effect of mesh refinement around the nugget circumference . . . . .	93
Figure A.4:	Effect of mesh refinement on the stress-based fatigue life prediction . . .	94
Figure B.1:	Effect of restraint diameter on the fatigue life of spot-welded specimens	95

# List of Tables

Table 2.1:	Generic mechanical properties employed in the definition of steel $S - N$ curves in <i>nCode DesignLife</i> [19] . . . . .	13
Table 2.2:	Generic mechanical properties employed in the definition of Al $S - N$ curve in <i>nCode DesignLife</i> [19] . . . . .	14
Table 2.3:	Properties of the master $S - N$ curve [23] . . . . .	17
Table 2.4:	Properties of $S - N$ curves for stress-based fatigue analysis [23] . . . . .	17
Table 3.1:	Mechanical properties employed in the fatigue analysis using <i>FEMFAT Spot</i> . . . . .	22
Table 3.2:	Comparison of methods implemented in <i>FEMFAT Spot</i> and <i>nCode DesignLife</i> . . . . .	28
Table 4.1:	Comparison of results for $X$ -axis direction test . . . . .	39
Table 4.2:	Comparison of results for $Y$ -axis direction test . . . . .	39
Table 4.3:	Comparison of results for $Z$ -axis direction test . . . . .	39
Table 4.4:	Comparison of cumulative damage values . . . . .	40
Table 5.1:	Properties of base material following Ludwik's hardening law [71] . . . . .	55
Table 5.2:	The change in the first eigenfrequency of tensile shear specimen . . . . .	58
Table 5.3:	Comparison of numerical results with experimental data [71] . . . . .	61
Table 5.4:	Comparison between numerical and experimental data [71] for the modified failure initiation criterion . . . . .	64
Table 5.5:	The change in the first eigenfrequency of coach peel specimen . . . . .	66
Table 5.6:	Comparison of numerical results with experimental data [71] . . . . .	69
Table 5.7:	Comparison of numerical results with experimental data [71] . . . . .	72
Table 5.8:	Comparison between numerical results obtained using optimized spot weld stiffness and experimental data [71] . . . . .	73
Table A.1:	The effect of mesh refinement around the nugget circumference on the fatigue life of tensile shear specimen using <i>nCode DesignLife</i> . . . . .	89
Table A.2:	Comparison of obtained results ( <i>nCode DesignLife</i> ) . . . . .	89
Table A.3:	The effect of mesh alignment on the fatigue life of tensile shear specimen using <i>nCode DesignLife</i> . . . . .	89

Table A.4:	Comparison of obtained results ( <i>nCode DesignLife</i> ) . . . . .	89
Table A.5:	Comparison of obtained results ( <i>nCode DesignLife</i> ) . . . . .	90
Table A.6:	Comparison of obtained results ( <i>nCode DesignLife</i> ) . . . . .	90
Table A.7:	The effect of mesh refinement around the nugget circumference on the fatigue life of coach peel specimen using <i>FEMFAT Spot</i> . . . . .	90
Table A.8:	Comparison of obtained results ( <i>FEMFAT Spot</i> force-based approach) .	91
Table A.9:	Effect of mesh alignment on fatigue life of coach peel specimen ( <i>FEMFAT</i> <i>Spot</i> force-based approach) . . . . .	91
Table A.10:	Comparison of obtained results ( <i>FEMFAT Spot</i> force-based approach) .	91
Table A.11:	Comparison of obtained results ( <i>FEMFAT Spot</i> force-based approach) .	92
Table A.12:	Comparison of obtained results ( <i>FEMFAT Spot</i> force-based approach) .	92
Table A.13:	Effect of mesh refinement on the stress-based fatigue life prediction of tensile shear specimen . . . . .	93

# List of Symbols and Units

Latin symbols		
Symbol	Unit	Description
$a$	mm	Crack length
$a$	mm	Edge length of the hexahedral element
$b$	-	Material fatigue exponent
$b$	-	Rate of change of the connector yield surface
$c_d$	m/s	Dilatational wave speed
$C$	-	Material-dependent constant
$\mathbf{C}$	N·s/m	Damping matrix
$d$	mm	Diameter of spot weld nugget
$d_i$	-	Connector element scalar damage variable
$D$	mm	Restraint diameter of annular plate
$D$	-	Cumulative damage variable
$D_{HAZ}$	mm	Diameter of the heat affected zone
$E$	J	Energy
$E$	N/mm <sup>2</sup>	Modulus of elasticity
$E[0]$	Hz	Expected number of zero crossings per unit time
$E[P]$	Hz	Expected number of peaks per unit time
$f$	Hz	Frequency
$f_s$	N	Connector shear derived loading component
$F_N$	N	Spot weld tensile strength
$F_S$	N	Spot weld shear strength
$F_H$	N	Force describing connector isotropic hardening
$\bar{F}$	N	Connector equivalent force
$F_0$	N	Connector yielding force
$\mathbf{F}$	N	Force vector
$\mathbf{H}$	-	Frequency response function matrix
$I$	mm <sup>4</sup>	Area moment of inertia
$\mathbf{I}$	N	Vector of internal forces

$J$	$\text{mm}^4$	Polar moment of inertia
$k$	-	Material strength coefficient
$K$	$\text{MPa}\sqrt{\text{mm}}$	Stress intensity coefficient
$L$	$\text{mm}$	Length of element representing spot weld
$L_{min}$	$\text{mm}$	The smallest element length
$m$	-	Material-dependent coefficient
$m_b$	$\text{Nmm}$	Connector bending loading component
$m_n$	-	Spectral moment
$M_B$	$\text{Nmm}$	Connector bending strength
$M_T$	$\text{Nmm}$	Connector torsional strength
$\mathbf{M}$	$\text{kg}$	Mass matrix
$N$	-	Number of cycles to failure
$\mathbf{P}$	$\text{N}$	Vector of external forces
$Q$	-	Maximum change of the connector yield surface
$R$	-	Load ratio
$S$	$\text{mm}^2$	Cross-section area
$S(\omega)$	$\text{x}^2/\text{Hz}$	Power spectral density
$t$	$\text{mm}$	Sheet thickness
$\mathbf{u}$	$\text{mm}$	Displacement vector
$\dot{\mathbf{u}}$	$\text{mm/s}$	Vector of nodal velocities
$\ddot{\mathbf{u}}$	$\text{mm/s}^2$	Vector of nodal accelerations

#### Greek symbols

Symbol	Unit	Description
$\alpha$	-	Irregularity factor
$\beta$	-	Parameter defining spot weld failure surface
$\kappa$	-	Material-dependent geometry factor
$\nu$	-	Poisson ratio
$\sigma_a$	$\text{N/mm}^2$	Stress amplitude
$\sigma_{eq}$	$\text{N/mm}^2$	Equivalent structural stress
$\sigma_N$	$\text{N/mm}^2$	Endurance limit
$\sigma_r$	$\text{N/mm}^2$	Radial stress
$\sigma_{UTS}$	$\text{N/mm}^2$	Ultimate tensile strength
$\sigma_Y$	$\text{N/mm}^2$	Yield strength
$\tau$	$\text{N/mm}^2$	Shear stress
$\Phi$	-	Shape function vector

# List of Abbreviations

Abbreviation	Description
ACM	Area Contact Method
AHSS	Advanced high strength steel
BM	Base material
DOF	Degree of freedom
DP	Dual phase steel
FFT	Fast Fourier Transformation
FE	Finite element
FRF	Frequency response function
FZ	Fusion zone
HAZ	Heat affected zone
HCF	High cycle fatigue
HSLA	High strength low alloying steel
IF	Interfacial failure
MDOF	Multiple degree of freedom system
NVH	Noise, vibration and harshness
P2P	Point-to-point connection
PDF	Probability density function
PIF	Partial interfacial failure
POF	Pullout failure
PSD	Power spectral density
RMS	Root mean square
RSW	Resistance spot welding
SSD	Steady-state dynamics
SW	Spot weld



# Sažetak (Abstract in Croatian)

Automobilska industrija jedna je od najvećih svjetskih industrija koja godišnje proizvodi otprilike 50 milijuna vozila. U novije vrijeme se, zbog ograničenja emisija ispušnih plinova te zahtjeva za povećanjem sigurnosti cestovnog prometa, ali i zahtjeva kupaca, suvremena autoindustrija suočava s izazovima smanjenja mase vozila, poboljšanja ekonomičnosti potrošnje goriva te optimiranja u svrhu povećanja kompatibilnosti tijekom sudara. Elektrootporno točkasto zavarivanje je najzastupljeniji postupak spajanja metalnih limova u autoindustriji, a zavar nastaje uslijed topline koja se razvija prolaskom struje kroz elektrode te otpora materijala koji se zavaruje. Dakle, točkasti zavar nastaje kao rezultat kompleksnog međudjelovanja topline, pritiska elektroda i naglih faznih pretvorba u materijalu. Budući da točkasti zavar predstavlja geometrijski i materijalni diskontinuitet, oko zavarenog spoja javlja se koncentracija naprezanja, što ima negativan utjecaj na pojavu pukotina uslijed cikličkih opterećenja te na integritet konstrukcije tijekom dinamičkih opterećenja, tj. sudara. Nadalje, numerička analiza pomoću metode konačnih elemenata te razvoj metoda za proračun zavara na temelju sila omogućuju brz i jednostavan proračun točkasto zavarenih spojeva uslijed cikličkih i dinamičkih opterećenja, čime se smanjuju troškovi i vrijeme eksperimentalnih ispitivanja u fazi izrade prototipa i konstruiranja. Stoga je cilj ovog diplomskog rada razviti numeričke procedure za proračun točkasto zavarenih spojeva uslijed cikličkih opterećenja s konstantnim amplitudama i stohastičkih uzbuda te uslijed dinamičkog šoka.

**Ključne riječi:** točkasti zavar, metoda konačnih elemenata, stohastička uzbuda, oštećenje

# Abstract

Occupant safety, weight reduction, fuel efficiency and vehicle crashworthiness remain the most challenging design objectives of the modern automotive industry. Recent improvements in sheet metal joining processes and the use of advanced high strength steels have increased fuel-efficiency and enhanced vehicle durability, as well as the integrity of passenger compartment, simultaneously increasing weight reduction. Resistance spot welding is the most widely used metal joining process in automotive industry intended for joining of light gauge overlapping metal sheets. Although resistance spot welding includes complex interaction between mechanical loading, heating generated by the electric current and rapid microstructural transformations, compared to other joining processes, resistance spot welding is fast, easily automated and does not require the additional filler material. Since the material heterogeneity and geometric discontinuity around the weld nugget circumference cause stress concentration, spot-welded components are prone to premature failure under fatigue and crash loading conditions. Hence, it is crucial to understand the welded region microstructure and the mechanical behavior of spot-welded joints to balance competing design objectives and thus enhance vehicle durability and crashworthiness.

In recent times numerical analyses have had a major impact on design optimization and cost reduction of full-scale experiments during prototype testing. Moreover, various numerical methods have been proposed to evaluate the fatigue strength of spot welds under constant amplitude loading. Generally, the fatigue analysis of spot-welded joints is classified into stress-based and force-based approaches. In comparison with the stress-based method, the force-based approach offers a quick solution and an accurate fatigue life estimation. Therefore, one of the objectives of the conducted research was to evaluate the existing methods for the fatigue analysis of spot-welded structures under constant amplitude loading and to study the effect of geometric characteristics on the fatigue behavior of spot-welded specimens. However, vehicle components are seldom subjected to the constant amplitude cyclic loading, thus the method of random vibration fatigue life prediction for spot-welded structures is evaluated. Finally, quasi-static damage analysis of spot-welded specimens is performed to evaluate the coupled force-based damage initiation criterion, which captures the complex behavior of spot-welded joints under general loading conditions, yet greatly simplifying the analysis.

**Keywords:** spot weld, finite element method, fatigue, random excitation, damage

# Prošireni sažetak

Ovaj rad izrađen je u suradnji s tvrtkom AVL-AST d.o.o iz Zagreba i austrijskom tvrtkom AVL List GmbH. AVL je automobilska tvrtka koja se bavi razvojem pogonskih sklopova pokretanih motorima s unutarnjim izgaranjem i električnih pogonskih sklopova te razvojem različite mjerne opreme i testnih stanica za automobilsku industriju.

Elektrootporno točkasto zavarivanje najzastupljeniji je postupak spajanja limova u suvremenoj autoindustriji. Također, proces točkastog zavarivanja uključuje kompleksno međudjelovanje topline koja se razvija prolaskom struje kroz elektrode, mehaničkog opterećenja uslijed pritiska elektroda te naglih temperaturnih promjena i faznih pretvorba materijala koji se zavaruje. Budući da točkasti zavari predstavljaju geometrijski i materijalni diskontinuitet, oko zavarenog spoja javlja se koncentracija naprezanja, što ima negativan utjecaj na pojavu pukotina uslijed cikličkih opterećenja te na integritet konstrukcije tijekom dinamičkih opterećenja. Stoga se područje istraživanja ovog diplomskog rada može podijeliti u četiri cjeline:

1. Utvrditi proceduru numeričkog proračuna točkasto zavarenih spojeva opterećenih cikličkim opterećenjem s konstantnim amplitudama u programskim paketima *nCode Design Life* i *FEMFAT Spot*,
2. Istražiti utjecaj geometrijskih karakteristika zavara, tj. promjera zavara i debljine zavarenih limova na životni vijek točkasto zavarenih uzoraka,
3. Utvrditi proceduru numeričkog proračuna točkasto zavarenih spojeva uslijed stohastičkih opterećenja u programskom paketu *nCode DesignLife*,
4. Utvrditi proceduru numeričke simulacije iniciranja oštećenja točkasto zavarenih spojeva uslijed kvazistatičkog opterećenja te verificirati postojeći kriterij iniciranja oštećenja.

U prvom, uvodnom dijelu ukratko je opisan proces elektrootpornog točkastog zavarivanja te mikrostruktura zavarenog spoja.

Drugo poglavlje opisuje problem zamora točkasto zavarenih spojeva te su prikazane metode proračuna točkasto zavarenih spojeva uslijed cikličkih opterećenja s konstantnim amplitudama. Postojeće metode dijele se na metode koje životni vijek točkasto zavarenih spojeva određuju na temelju naprezanja u konačnim elementima oko ruba zavarenog spoja te metode koje životni vijek točkasto zavarenih spojeva određuju pomoću sila u čvorovima konačnih elemenata koji predstavljaju zavar.

U trećem poglavlju prikazani su rezultati provedenih analiza zamora točkasto zavarenih uzoraka te su dobiveni rezultati uspoređeni s eksperimentalnim podacima iz literature. Nadalje, ispitan je utjecaj povećanja gustoće mreže konačnih elemenata te utjecaj modeliranja točkastih zavora na životni vijek točkasto zavarenih uzoraka. Također, ispitan je utjecaj promjera zavora te debljine zavarenih limova na životni vijek točkastih zavora, a analizom rezultata utvrđeno je da porast navedenih geometrijskih karakteristika uzrokuje produljenje životnog vijeka točkasto zavarenih uzoraka.

U četvrtom poglavlju ukratko je prikazan proces obrade stohastičkih signala te proračun zamora konstrukcija uslijed nedeterminističke uzbude. Spektralna analiza zamora u frekvencijskoj domeni može se podijeliti u četiri koraka: određivanje opterećenja modela, izračun prijenosnih funkcija odziva konstrukcije, određivanje vjerojatnosti raspona vršnih vrijednosti naprezanja te izračun kumulativnog zamornog oštećenja. Nadalje, utvrđena je procedura numeričkog proračuna točkasto zavarenih spojeva uslijed stohastičkih opterećenja u programskom paketu *nCode DesignLife*. Također, uspoređene su različite statističke metode za procjenu vjerojatnosti raspona vršnih vrijednosti naprezanja te su prikazani rezultati provedenih analiza.

Peto poglavlje opisuje načine popuštanja, odnosno iniciranja te propagiranja oštećenja u točkasto zavarenim spojevima. Također, u ovom je poglavlju opisan i verificiran kriterij iniciranja oštećenja u točkastim zavarima te je opisana eksperimentalna procedura određivanja parametara potrebnih za opisivanje deformabilnog ponašanja konačnih elemenata koji predstavljaju točkasti zavar. Nadalje, rezultati provedenih analiza uspoređeni su s eksperimentalnim podacima iz literature.

Konačno, u šestom poglavlju istaknuti su zaključci provedenog istraživanja te su dani prijedlozi za daljnji rad.

# 1 | Introduction

Due to increasing limitations in terms of pollution, performance, energy consumption reduction and safety, the goal of the modern automotive industry is to produce lightweight, fuel-efficient and reliable vehicles. Recent improvements in the use of advanced high strength steels (AHSS), such as high strength low alloying (HSLA) and dual phase steels (DP), have increased weight reduction, improved fuel efficiency and enhanced vehicle crashworthiness. Alternatively, weight reduction can be achieved by using more efficient metal joining processes, such as resistance spot welding (RSW), which is one of the most widely used sheet metal joining technique in the automotive industry. Compared to other joining processes, resistance spot welding is fast, easily automated and does not require additional filler material. Furthermore, RSW includes complex interaction between mechanical loading, heating caused by the resistance of electrodes and materials to be welded, rapid thermal changes and metallurgical phase transformations [1–9]. The process is carried out in four cycles, as depicted in Figure 1.1.

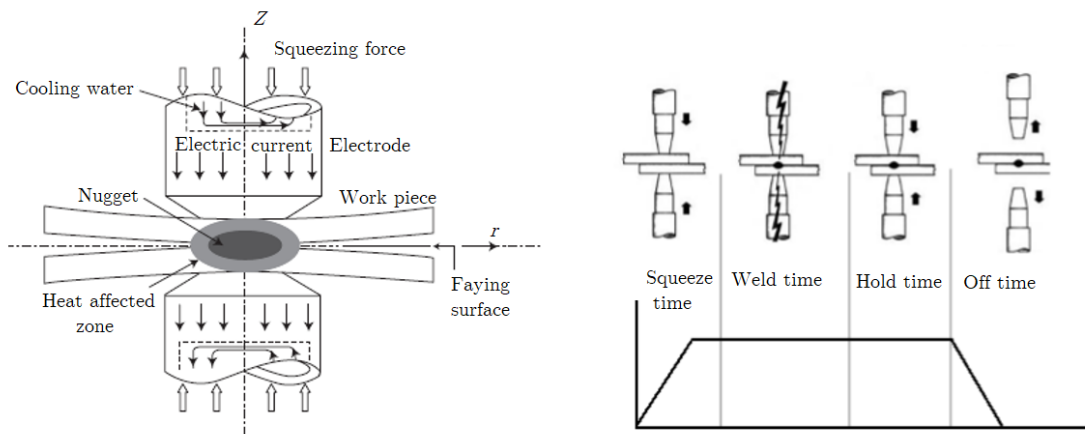
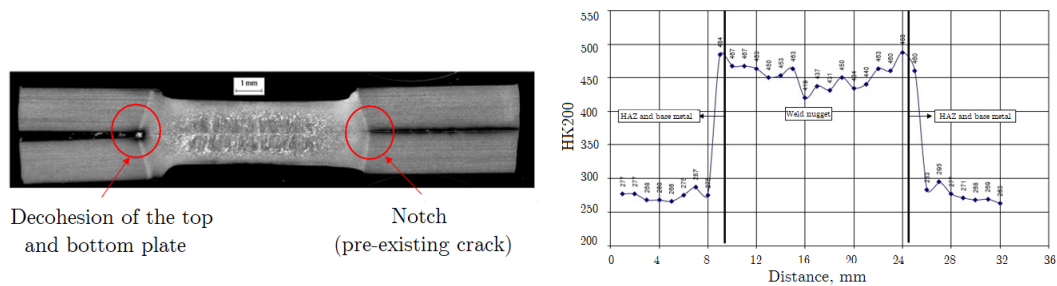


Figure 1.1: a) Schematic of spot welding process [1], b) Cycles of spot welding process [2]

During the squeeze cycle, water-cooled electrodes exert pressure on two or more sheets to be joined, thus producing mechanical loading. In the next cycle, electric current flows through electrodes and it is the resistance of metal sheets and the contact resistance at the faying interface that produces local heat sufficient to cause the weld nugget formation [1-5]. The electric current is then turned off and the weld nugget is allowed to cool down and to solidify under electrode pressure.

Since metal materials undergo drastic microstructural changes during resistance spot welding process [6–9], there has been a focus on understanding the weldability of AHSS and the microstructure of the welding region. Generally, spot welds consist of three distinct regions with different materials properties, which depend upon hardness distribution along the spot welded region. In addition, the typical hardness distribution profile and the microstructure after welding are shown in Figure 1.2.



**Figure 1.2: Weld nugget microstructure and hardness distribution [10]**

The fusion zone (FZ) or the weld nugget represents the melted and resolidified region, which exhibits the highest hardness. The heat affected zone (HAZ) is the region surrounding the weld nugget in which the material to be welded does not reach the melting temperature but undergoes microstructural changes, whereas the base material (BM) is unaffected by the welding heat. As shown in Figure 1.2, the spot welded region encounters steep hardness gradients, which indicates that weld nuggets exhibit brittle behavior. Generally, resistance spot welding produces an external crack at the faying interface caused by the heat input and the electrode pressure, which induces large stress concentration. Additionally, the electrode pressure causes a slight separation of welded sheets and a surface indentation. Therefore, RSW results both in material and geometric discontinuity. The aforementioned microstructural and geometrical changes modify the mechanical behavior of spot-welded structures. Hence, it is crucial to understand the physical phenomena occurring during resistance spot welding to achieve design optimization and thus enhance vehicle durability and crashworthiness.

## 1.1 Motivation

The automotive industry is facing the challenge of producing fuel-efficient, durable and lightweight vehicles, at the same time trying to reduce costs and keep the performance quality demanded by customers. Lightweight design can be achieved by the use of AHSS and RSW, which is one of the primary metal joining processes. Due to the stress concentration around the nugget periphery, spot welds are prone to premature fatigue failure, as well as to the failure under dynamic loading conditions. Therefore, it is important to understand the phenomena occurring during the RSW process and their effects on welded structures to optimize the design, thus improving the vehicle durability and crashworthiness.

In recent times, numerical simulations have had a major impact on improving the design and reducing the time and cost of prototype testing. It is therefore crucial to verify existing methods of spot weld fatigue life estimation and damage analysis under dynamic loading conditions using spot weld finite element models, which are simple and easily created, but can capture the complex spot weld microstructure and behaviour.

## 1.2 Thesis structure overview

The aim of this thesis is to define a procedure for the fatigue life assessment and damage analysis of spot welded structures. The first, introductory chapter briefly addresses the description of the resistance spot welding process and the microstructure of the welded region.

Chapter 2 discusses failure mechanisms of spot welds subjected to cyclic loading and methodologies for fatigue life assessment of spot welded structures implemented in fatigue solvers *FEMFAT Spot* and *nCode DesignLife*. The results obtained using the aforementioned fatigue solvers are presented in Chapter 3.

Chapter 4 covers the basic concepts of stochastic signal processing and the procedure of random vibration fatigue analysis. Additionally, the results of the performed finite element analyses are presented at the end of the chapter.

Chapter 5 deals with spot weld failure mechanisms under dynamic loading conditions and discusses the existing coupled force-based damage initiation criterion. Moreover, the results of the performed analyses and verification of the failure criterion are presented.

Finally, Chapter 6 briefly outlines the conclusions drawn from the conducted research and recommendations for future work.

## 2 | Fatigue of spot welded joints

### 2.1 Introduction

During the operational time, vehicle components experience cyclic or fatigue loading. It has been observed that the most durability issues of vehicle components are related to spot welds [11–13]. Therefore, the primary requirement for achieving the desired durability is the understanding of fatigue failure mechanisms and their prevention. Due to the existence of a notch or a pre-existing crack, spot weld fatigue is a crack propagation dominated phenomenon [14]. The two primary failure modes under cyclic loading conditions are interfacial (IF) and pullout failure (POF), as shown in Figure 2.1.

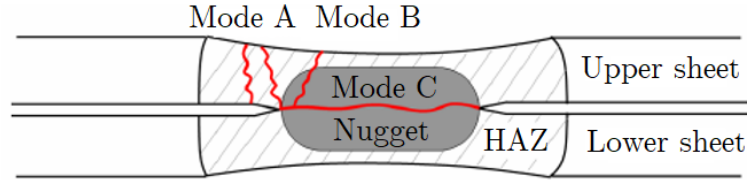


**Figure 2.1: Spot weld failure modes under cyclic loading [15]**

The interfacial failure (Mode C) occurs due to the propagation of a pre-existing crack into the weld nugget parallel to the spot welded sheets. As the spot-welded region is continuously loaded, the crack eventually cuts through the weld nugget, thus indicating poor weld quality and low load carrying capability. In contrast, the first stage of the pullout failure (Mode A) is the propagation of a pre-existing crack (or a crack initiated in HAZ) approximately perpendicular to the welded sheets. As the cyclic loading continues, the crack eventually emerges from one side, leaving the weld nugget intact. Hence, the pullout failure represents the failure of the material surrounding the weld nugget and it is common for larger weld diameters, due to the increased overall bond area, strength and load required to cause failure.





SVEUČILIŠTE U ZAGREBU  
FAKULTET STROJARSTVA I BRODOGRADNJE



Središnje povjerenstvo za završne i diplomске ispite  
Povjerenstvo za diplomске ispite studija strojarstva za smjerove:  
procesno-energetski, konstrukcijski, brodstrojarski i inženjersko modeliranje i računalne simulacije

Sveučilište u Zagrebu Fakultet strojarstva i brodogradnje	
Datum: 1. 03. 2019.	Prilog
Klasa: 02-01/19-013	
Ur.broj: 15-1703-19-182	

## DIPLOMSKI ZADATAK

Student: Ana Vrgoč

Mat. br.: 0035196045

Naslov rada na  
hrvatskom jeziku:

**Numerička analiza točkastih zavara u tankostijenim konstrukcijama  
izloženim mehaničkom šoku i vibracijskim opterećenjima**

Naslov rada na  
engleskom jeziku:

**Numerical Analysis of Spot Welds in Sheet Metal Structures Exposed  
to Mechanical Shock and Vibration Loading**

Opis zadatka:

Spot weld technology is present in automobile manufacturing industry for many years. It is a process in which the contacting sheet metal surfaces are joined together by the heat obtained from resistance to electric current. In the past, the process was mainly used for building the body of the car, with automated industrial robots found on the assembly lines. Nowadays, with the strong growing development of the hybrid and electric powertrains, spot welds are widely used in the battery pack assemblies and power electronic components carriers, attached to the body of a car. These components are exposed to shock loads (mechanical shock, e.g. crash, foreign object impact) and vibrational loads (harmonic or random, e.g. road excitation) during the development and testing phase. The applied loads are designed to simulate and predict vehicle real life conditions. Therefore, it is crucial to understand damage and failure mechanisms of the components and joints for successful life prediction.

This master thesis will focus on the spot welds evaluation methods and criteria in vehicle powertrain applications. Based on everything said above in this study it is necessary to:

1. Study available literature on the finite element modeling of spot welds, spot weld damage mechanisms and spot weld fatigue.
2. Investigate available finite element methods and tools for the spot weld fatigue analysis (e.g. FEMFAT SPOT and nCode DesignLife).
3. Investigate finite element procedures for the quasi-static spot weld damage analysis.
4. Apply studied spot weld analysis procedures and compare to the experimental results.

During thesis preparation one must comply with the standard rules for preparation of master thesis. It is necessary to list all literature used and received assistance.

Zadatak zadan:

17. siječnja 2019.

Rok predaje rada:

21. ožujka 2019.

Predviđeni datumi obrane:

27., 28. i 29. ožujka 2019.

Zadatak zadao:

Prof. dr. sc. Zdenko Tonković

Predsjednica Povjerenstva:

Prof. dr. sc. Tanja Jurčević Lulić



SVEUČILIŠTE U ZAGREBU  
FAKULTET STROJARSTVA I BRODOGRADNJE



Središnje povjerenstvo za završne i diplomske ispite  
Povjerenstvo za diplomske ispite studija strojarstva za smjerove:  
procesno-energetski, konstrukcijski, brodstrojarski i inženjersko modeliranje i računalne simulacije

Sveučilište u Zagrebu Fakultet strojarstva i brodogradnje	
Datum: 1. 03. 2019.	Prilog
Klasa: 02-01/19-013	
Ur.broj: 15-1703-19-182	

## DIPLOMSKI ZADATAK

Student: Ana Vrgoč

Mat. br.: 0035196045

Naslov rada na  
hrvatskom jeziku:

**Numerička analiza točkastih zavara u tankostijenim konstrukcijama  
izloženim mehaničkom šoku i vibracijskim opterećenjima**

Naslov rada na  
engleskom jeziku:

**Numerical Analysis of Spot Welds in Sheet Metal Structures Exposed  
to Mechanical Shock and Vibration Loading**

Opis zadatka:

Spot weld technology is present in automobile manufacturing industry for many years. It is a process in which the contacting sheet metal surfaces are joined together by the heat obtained from resistance to electric current. In the past, the process was mainly used for building the body of the car, with automated industrial robots found on the assembly lines. Nowadays, with the strong growing development of the hybrid and electric powertrains, spot welds are widely used in the battery pack assemblies and power electronic components carriers, attached to the body of a car. These components are exposed to shock loads (mechanical shock, e.g. crash, foreign object impact) and vibrational loads (harmonic or random, e.g. road excitation) during the development and testing phase. The applied loads are designed to simulate and predict vehicle real life conditions. Therefore, it is crucial to understand damage and failure mechanisms of the components and joints for successful life prediction.

This master thesis will focus on the spot welds evaluation methods and criteria in vehicle powertrain applications. Based on everything said above in this study it is necessary to:

1. Study available literature on the finite element modeling of spot welds, spot weld damage mechanisms and spot weld fatigue.
2. Investigate available finite element methods and tools for the spot weld fatigue analysis (e.g. FEMFAT SPOT and nCode DesignLife).
3. Investigate finite element procedures for the quasi-static spot weld damage analysis.
4. Apply studied spot weld analysis procedures and compare to the experimental results.

During thesis preparation one must comply with the standard rules for preparation of master thesis. It is necessary to list all literature used and received assistance.

Zadatak zadan:

17. siječnja 2019.

Rok predaje rada:

21. ožujka 2019.

Predviđeni datumi obrane:

27., 28. i 29. ožujka 2019.

Zadatak zadao:

Prof. dr. sc. Zdenko Tonković

Predsjednica Povjerenstva:

Prof. dr. sc. Tanja Jurčević Lulić

Moreover, most spot welds in automotive components are designed to fail in pullout mode, thus the nugget diameter sufficient to ensure the pullout [16, 17] failure is equal to:

$$\text{AWS}^1 : d = 4\sqrt{t}, \text{JISZ3140}^2 : d = 5\sqrt{t}, \quad (2.1)$$

where  $t$  is the sheet thickness. In addition, advanced high strength steels commonly fail in partial interfacial mode (Mode B), which is propelled by the growth of a pre-existing crack into the weld nugget. As the fluctuating loading continues, the crack redirects its path perpendicular to joined metal sheets and eventually emerges from one side, as shown in Figure 2.1.

## 2.2 Experimental evaluation of the fatigue behavior of spot welded specimens [14]

The fatigue performance of spot-welded joints depends on various factors, such as temperature-dependent material properties, welding parameters, weld nugget geometry, base material properties etc. The aim of the modern automotive industry is to ensure sufficient fatigue performance of spot welded structures throughout the anticipated operational time. Therefore, numerous experiments were conducted to determine the fatigue properties of spot-welded joints. In this thesis, the experimental results provided by Bonnen *et al.* [14] are used to validate the numerical procedure for spot weld fatigue analysis under constant amplitude cyclic loading. Bonnen *et al.* carried out numerous experiments to determine the effect of base material properties, sheet thickness, nugget diameter, load ratio etc. on the fatigue life of spot-welded specimens. Moreover, the specimen geometry is presented in Figure 2.2, whereas Figure 2.3 shows the load amplitude with respect to the number of cycles to failure <sup>3</sup> for spot-welded specimens ( $d=7$  mm) of various high strength steel materials. It is important to emphasize that data labels ending with 01 indicate the load ratio equal to 0.1, whereas data labels 03 indicate the load ratio corresponding to 0.3.

---

<sup>1</sup>American Welding Society

<sup>2</sup>Japanese Industrial Standard - Method of inspection and acceptance levels for resistance spot welds

<sup>3</sup>Failure is defined as a complete separation of the welded sheets.

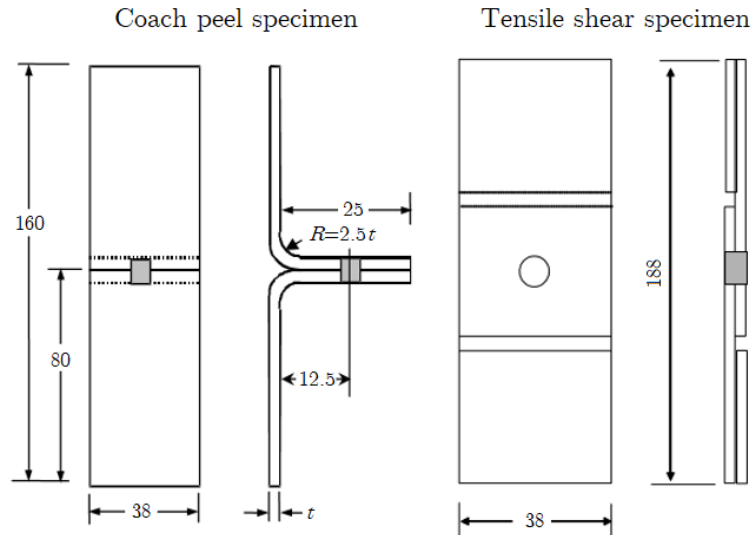


Figure 2.2: Spot-welded specimens used for experimental testing [14]

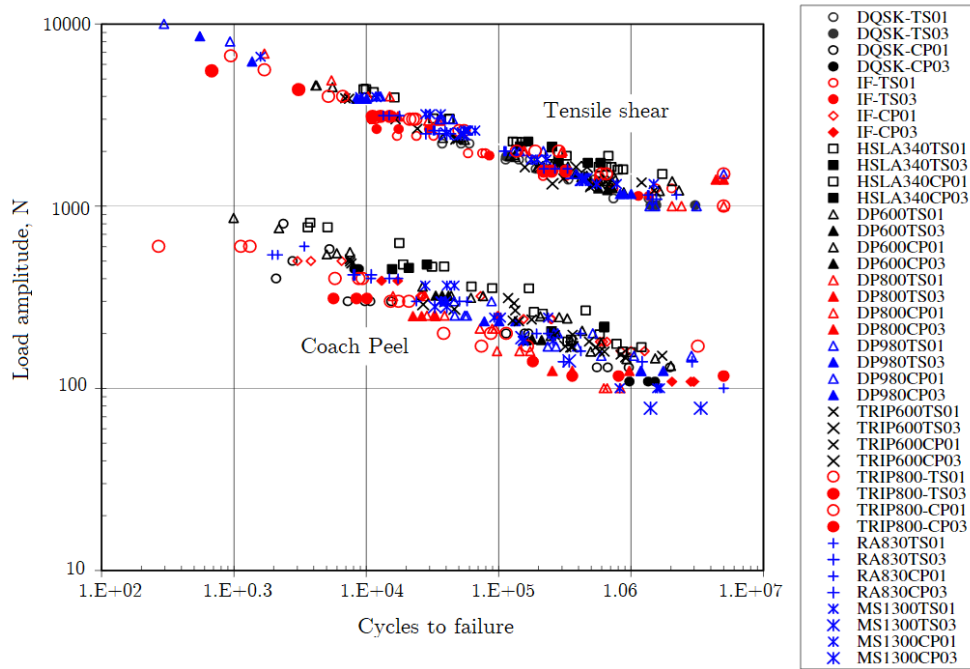


Figure 2.3: Effect of base material and load ratio on the fatigue behavior of spot-welded specimens [14]

From the results displayed above, it can be observed that in the case of tensile shear specimen, the fatigue data fall within a narrow band, indicating no significant influence of base material properties on the fatigue behavior of spot-welded specimens. This phenomenon can best be explained by the existence of a crack-like notch at the faying interface. Bonnen *et al.* [14] observed that under cyclic loading conditions, the pre-existing crack propagates approximately perpendicular to the imposed loading direction through the heat affected zone. Thus, the crack nucleation stage typically observed in metal materials is completely omitted.

Moreover, the crack propagation stage under constant amplitude cyclic loading is most frequently described with the Paris-Erdogan law:

$$\frac{da}{dN} = C(\Delta K)^m, \quad (2.2)$$

where  $\frac{da}{dN}$  is the crack growth rate,  $\Delta K$  represents the range of the stress intensity factor during the loading cycle, whereas  $C$  and  $m$  are material-dependent constants. Furthermore, Basquin proposed the following relationship between the stress amplitude and fatigue life:

$$\sigma_a = \sigma'_f (2N_f)^b, \quad (2.3)$$

where  $\sigma_a$  is the stress amplitude, whereas  $\sigma'_f$  and  $b$  are respectively the fatigue strength coefficient and the fatigue strength exponent. According to Bonnen *et al.* [14], the fatigue strength exponent is approximately equal to  $-1/m$ . Since for most metal materials the value of the crack propagation constant  $m$  varies between 3 and 5, the fatigue response of tensile shear specimen, regardless of the base material properties, is as expected.

Furthermore, due to the presence of residual stresses induced by the resistance spot welding process, the fatigue results indicate no significant influence of mean stress on the fatigue behavior of tensile shear specimen. In addition, Bonnen *et al.* [14] observed that the existing scatter of the tensile shear fatigue data results from the inability of the testing machine to consistently grip all specimens at the same location.

However, the experimental fatigue results for coach peel specimen exhibit greater scatter, owing to the specific specimen geometry, which tends to excessively deform at higher loads. Bonnen *et al.* [14] reported that there was variability in the manufactured specimen geometry. Namely, in the case of coach peel specimen the distance between the weld nugget centerline and the gripped flanges varied from specimen to specimen. Additionally, the flanges of coach peel specimen tend to excessively bend and rotate around the spot weld nugget, which led to the great scatter of the coach peel fatigue results. Nonetheless, the increase of the base material strength results in a higher resistance to excessive deformation and thus an improved durability. In addition, from the results shown in Figure 2.3, it can be observed that the coach peel specimen fatigue data indicate no significant influence of mean stress as well.

Furthermore, Figure 2.4 displays the mean stress effect and the effect of sheet thickness on the fatigue behavior of spot-welded specimens.

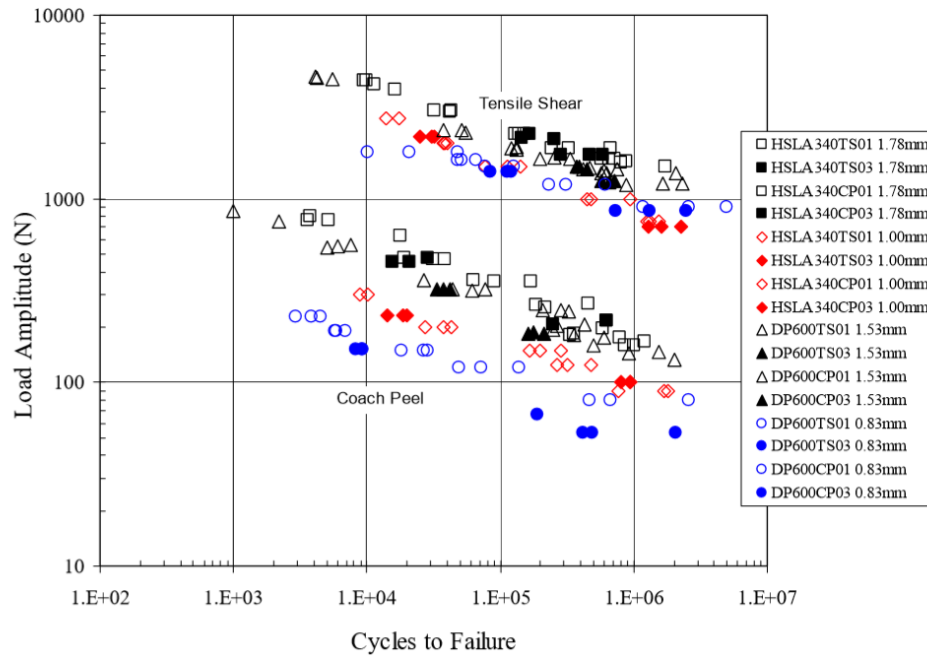


**Figure 2.4: Mean stress effect and effect of sheet thickness [14]**

Two material grades with different sheet thicknesses were compared, whereas the nominal nugget diameter is 7 mm. In addition, the fatigue tests were performed under constant amplitude loading with two different loading ratios, i.e.  $R=0.1$  and  $R=0.3$ . As evident, the fatigue results for tensile shear specimen indicate the significant influence of sheet thickness. Namely, the increase of sheet thickness leads to lower levels of stress, which results in the extended fatigue life. However, the coach peel fatigue data exhibit yet again greater scatter, which indicates that the fatigue life of coach peel specimen is greatly influenced by the gauge variation.

Based on the previously presented experimental results, the following conclusions are drawn [14]:

- The fatigue behavior of tensile shear specimen is independent of base metal material properties, for the studied steel grades. However, the coach peel fatigue results exhibit greater scatter, owing to the specific specimen geometry.
- Spot weld fatigue behavior of the studied AHSS, HSLA and low carbon steel is mean stress insensitive, for the mean stresses examined.
- Spot weld fatigue performance is largely controlled by the weld geometry (weld nugget diameter and sheet thickness).

## 2.3 Numerical methods for spot weld fatigue life assessment

Various numerical and analytical spot weld high cycle fatigue (HCF) prediction methods have been proposed in the literature, which indicates the importance of fatigue life assessment of spot welds in the early design stage. The existing methods for fatigue life assessment of spot-welded structures can be categorized into two main classes [12, 13]:

1. Stress-based approach, which estimates the fatigue life based on the stresses in shell elements surrounding the weld nugget,
2. Force-based approach, which extracts the forces and moments transferred through structural elements representing weld nuggets and calculates the stress history around the spot weld circumference, thus providing the basis for estimating the accumulated fatigue damage.

The stress-based approach was initially adopted by the automotive industry. However, it is now being replaced by force-based approaches, due to the complex stress state around the spot weld circumference and the inability to accurately calculate stresses in the spot-welded region [18]. The force-based methods offer a quick solution and a more accurate fatigue life prediction, since the forces and moments are more accurately estimated using finite element method compared to the stress determination in the spot-welded region. The following subsections deal with the two most commonly used force-based approaches implemented in software packages *nCode DesignLife* and *FEMFAT Spot*.

### 2.3.1 Rupp/LBF method [18, 19]

Rupp *et al.* [18] concluded that the detailed finite element estimation of stresses occurring in the spot-welded area is too complex, due to the considerable local plastic deformation and inability to accurately determine the weld nugget geometry. Hence, the detailed analysis of spot-welded structures is impractical for automotive applications regarding the corresponding computational expenses [18]. Moreover, both the application of fracture mechanics principles and notch-root analysis do not reflect the actual stress-strain state around the spot-welded region. Thus, the Rupp/LBF method is based on the calculation of structural stresses around the nugget circumference. Generally, the structural stress approach characterizes the stress state at the crack initiation location of

the spot-welded region. In addition, the estimated stress state is the basis for estimating the accumulated damage, whereas the main assumption of the aforementioned approach is that the structural stresses and thus the fatigue strength of spot-welded joints are directly related to the loading mode and the weld geometry. Therefore, the Rupp/LBF method neglects the local stress concentration caused by the weld nugget geometry and local material heterogeneity. The following assumptions are employed in the process of method development:

- Linear elastic material properties,
- Contact between spot-welded sheets is neglected,
- Torsional loading is neglected.

The Rupp/LBF method extracts nodal forces and moments from elements representing spot welds to calculate structural stresses around the nugget periphery both in the spot-welded sheets and the weld nugget. In addition, Figure 2.5 presents the circular plate model of a spot-welded specimen.

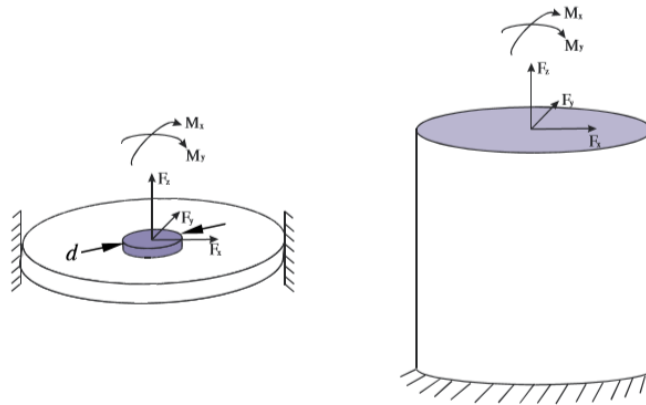


**Figure 2.5: Circular plate model with a rigid kernel at the centre [14]**

Structural stresses occurring in sheet metals are calculated using the following equations:

$$\sigma_{r,\max} = \frac{F_{x,y}}{\pi dt}, \quad \sigma_r = \frac{\kappa F_z}{t^2}, \quad \sigma_{r,\max} = \frac{\kappa M_{x,y}}{dt^2}, \quad (2.4)$$

where  $t$  represents the sheet thickness,  $d$  is the nugget diameter,  $F_{x,y}$ ,  $F_z$  and  $M_{x,y}$  are forces and moments acting on the weld nugget, whereas  $\kappa^4$  is the 'material-dependent geometry factor' [14].

---

<sup>4</sup> $\kappa$  is introduced in the equations that estimate the contribution of tensile force and bending moments to stresses calculated around the nugget circumference. Moreover,  $\kappa$  reduces the sensitivity of the aforementioned stress components to the sheet thickness [20].



Structural stresses occurring in the weld nugget are estimated as follows:

$$\sigma_n = \frac{4F_z}{\pi d^2}, \quad \sigma_b = \frac{32M_{x,y}}{\pi d^3}, \quad \tau_{\max} = \frac{16F_{x,y}}{3\pi d^2}. \quad (2.5)$$

As evident from Equations (2.4) and (2.5), there are three main contributions to structural stresses calculated around the nugget periphery: stress due to the in-plane shear forces, bending stress caused by the bending moment and bending stress due to the opening force acting perpendicular to the spot weld plane.

Since the spot weld nugget is treated as a rigid inclusion in the center of a circular plate, the ratio of the outer diameter  $D$  (at which the annular plate is clamped) to the spot weld diameter is fixed at 10 [18–20], which can lead to overestimated structural stresses and rather conservative solution (the real ratio of  $D/d$  of observed specimens is lower) [20].

As previously stated, the maximum structural stress at the spot weld edge is calculated either in the plates or in the nugget itself, depending on the crack propagation path. Hence, the Rupp/LBF method makes a clear distinction between the interfacial and pullout failure. In addition, thin sheet metals with large nugget diameters are prone to pullout failure, which manifests itself as a crack occurring next to the weld nugget and propagating perpendicularly to the sheet interface. However, interfacial failure (or the failure occurring through the weld nugget) preferably occurs in thick sheets with smaller weld diameters [18]. Hence, depending on the location of the maximum stress, failure occurs either in the sheet or through the weld nugget. Since most spot welds in automotive components are designed to undergo pullout failure, the equivalent stress around the nugget periphery in the sheet is calculated using the stress superposition formulae [14]:

$$\begin{aligned} \sigma_{eq} = & -\sigma_{max}(F_x)\cos(\theta) - \sigma_{max}(F_y)\sin(\theta) + \sigma(F_z) \\ & + \sigma_{max}(M_x)\sin(\theta) - \sigma_{max}(M_y)\cos(\theta). \end{aligned} \quad (2.6)$$

Furthermore, Rupp *et al.* [18] performed numerous fatigue experiments of various specimen geometries, including different sheet thicknesses, base material properties, nugget diameters, load ratios etc. to obtain spot weld fatigue data. Additionally, Rupp *et al.* [18] observed that for the constant amplitude loading, the fatigue results fall within a narrow band. Therefore, Rupp *et al.* used the obtained fatigue results in combination with the forces and moments extracted from the linear finite element analysis (spot welds are originally represented using stiff beam or bar elements) to form two generic  $S-N$  curves,

both for the nugget failure and the failure occurring in sheet metals, which makes the Rupp/LBF method universally applicable for spot-welded automotive components.

The fatigue life evaluation of spot-welded structures using *nCode DesignLife* is based on the modified Rupp/LBF method<sup>5</sup> [19]. The procedure for fatigue life assessment of spot-welded structures using *nCode DesignLife* starts with the extraction of nodal forces and moments transferred through structural elements representing spot welds. Based on the extracted nodal forces and moments, *nCode DesignLife* calculates the structural stress history both in the weld nugget and spot-welded sheets at user-defined intervals around the nugget circumference. The estimated structural stresses are then used to calculate the accumulated damage and thus the number of cycles to failure based on two generic  $S-N$  curves<sup>6</sup>. It is important to emphasize that although the Rupp/LBF method originally neglects the effect of torsional loading, *nCode DesignLife* offers the possibility to model the torsional failure as the distinct failure mode, which requires the definition of additional material parameters [19]. In addition, the following figures display the aforementioned generic  $S-N$  curves implemented in *nCode DesignLife* for use with spot-welded steel sheets, whereas Table 2.1 contains the material properties employed in the definition of generic  $S-N$  curves.

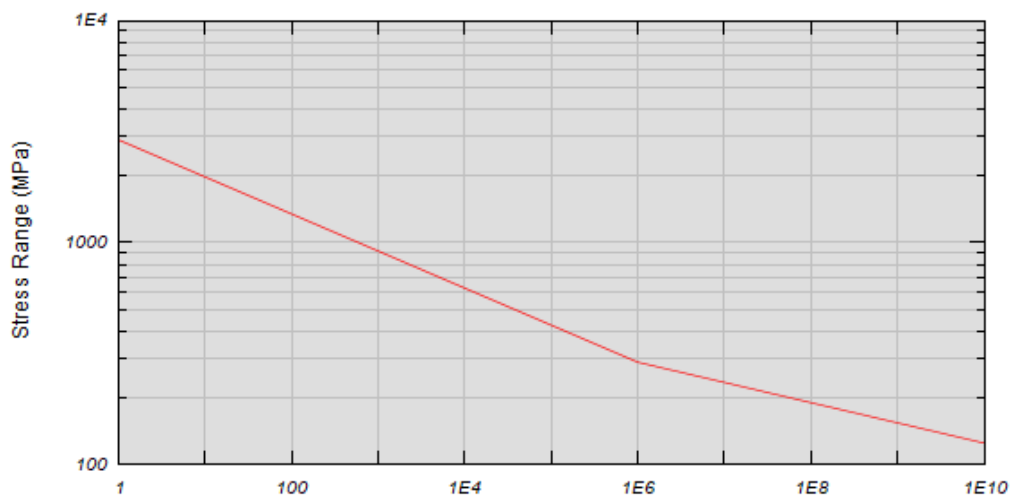


**Figure 2.6: Generic  $S - N$  curve for failure occurring in steel sheets [19]**

<sup>5</sup>*nCode DesignLife* introduces additional experimentally determined parameters into the equations used to calculate structural stresses to adjust the contribution of shear forces relative to the contribution of axial forces and bending moments. Moreover, the aforementioned parameters allow a size effect in terms of weld diameter and sheet thickness to be considered.

<sup>6</sup>The generic  $S - N$  curves implemented in *nCode DesignLife* are derived by Rupp *et al.* [18]

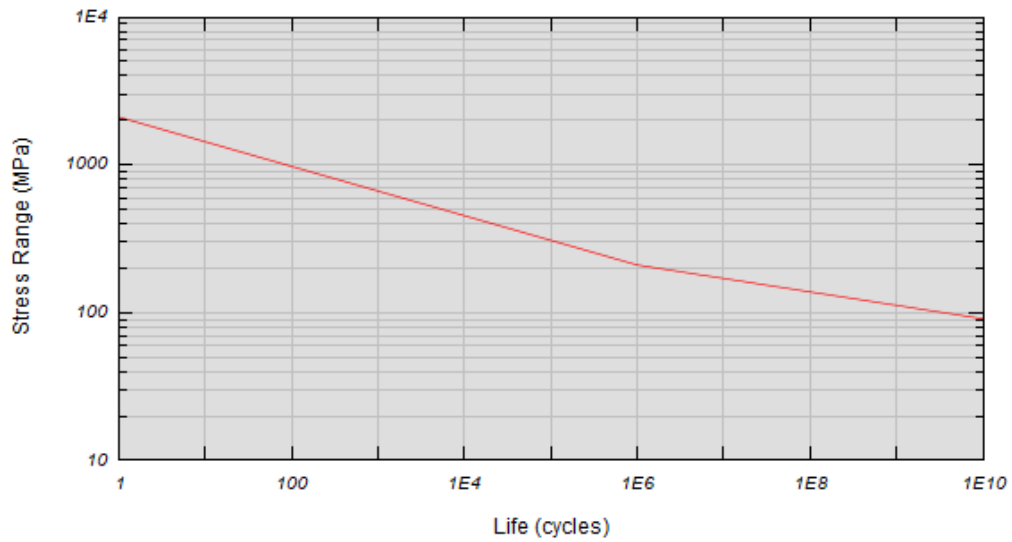


Figure 2.7: Generic  $S - N$  curve for failure through the nugget for spot-welded steel sheets [19]

Table 2.1: Generic mechanical properties employed in the definition of steel  $S - N$  curves in *nCode DesignLife* [19]

Generic Steel Sheet			
$E$ , GPa	$\sigma_Y$ , MPa	$\sigma_{UTS}$ , MPa	$\sigma_N$ , MPa
210	355	500	290
Generic Steel Nugget			
$E$ , GPa	$\sigma_Y$ , MPa	$\sigma_{UTS}$ , MPa	$\sigma_N$ , MPa
210	355	500	210

Moreover, Figure 2.8 displays  $S - N$  curve for use with aluminum spot-welded sheets, whereas Table 2.2 contains the generic material properties employed in the definition of the aforementioned  $S - N$  curve.

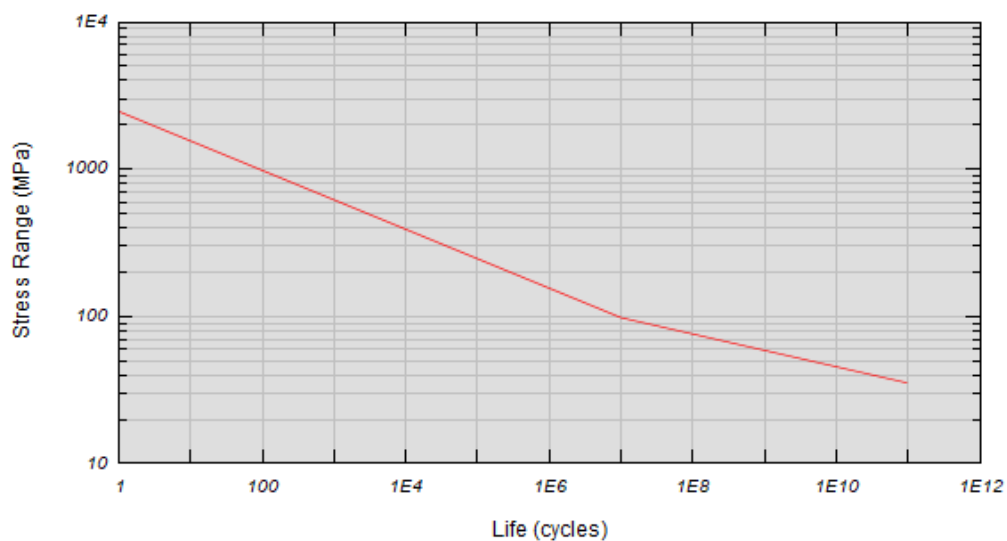


Figure 2.8: Generic aluminum  $S - N$  curve [19]

**Table 2.2: Generic mechanical properties employed in the definition of Al  $S - N$  curve in *nCode DesignLife* [19]**

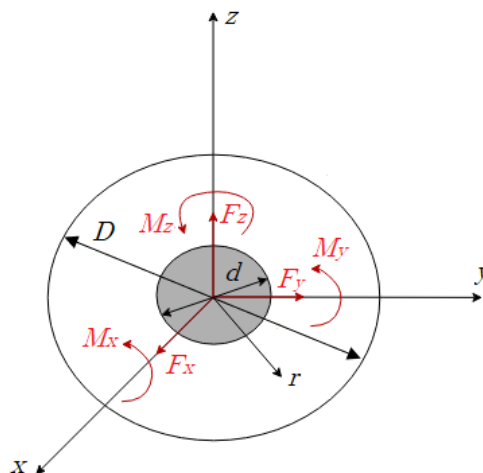
Generic Aluminum			
$E$ , MPa	$\sigma_Y$ , MPa	$\sigma_{UTS}$ , MPa	$\sigma_N$ , MPa
70000	150	300	200

As it was previously mentioned, *nCode DesignLife* introduces additional experimentally determined parameters into the equations used to calculate structural stresses around the nugget circumference, which differ for different  $S - N$  curves [19]. The aim of the aforementioned parameters is to further reduce scatter of estimated structural stresses in different spot-welded structures and for different sheet thicknesses, nugget diameters etc. In addition, the introduced parameters should be adjusted if new experimental fatigue data is implemented in the analysis.

### 2.3.2 Force-based spot fatigue life prediction based on [21]

Nakahara *et al.* [21] proposed an improved force-based method for fatigue life assessment of spot-welded structures, which extracts 6 general forces (Figure 2.9) acting on the weld nugget to calculate structural stresses around the nugget periphery. The following assumptions are employed in the process of method development:

- Linear elastic material properties,
- Contact between spot-welded sheets is neglected,
- The effect of torsional loading acting on the weld nugget is taken into consideration,
- The value of  $D/d$  can be modified to satisfy various application requirements.

**Figure 2.9: Forces acting on weld nugget [21]**

According to the proposed method, the equations which estimate nominal structural stresses are determined based on the elastic plate theory under the assumption of rigid nuggets [22].

First, stress components due to the tensile force  $F_z$  applied to the center of the clamped circular plate are examined (Figure 2.10). The normal stresses  $\sigma_{rp}$  and  $\sigma_{\theta p}$  developing around the nugget edge ( $r = d/2$ ,  $z = t/2$ ) are estimated using the following equations:

$$\sigma_{rp} = C_p F_z = \left\{ \frac{\ln\left(\frac{D}{d}\right)}{1 - \left(\frac{d}{D}\right)^2} - \frac{1}{2} \right\} \frac{3}{\pi t^2}, \quad \sigma_{\theta p} = \nu \sigma_{rp}. \quad (2.7)$$

Secondly, the circumferential distribution of normal stress  $\sigma_{rB}$  at the nugget edge ( $r = d/2$ ,  $z = t/2$ ) caused by the bending moment  $M_y$  (Figure 2.10) is estimated using the following equation:

$$\sigma_{rB} = -C_B M_y \cos(\theta) = \left\{ \frac{1 - \left(\frac{d}{D}\right)^2}{1 + \left(\frac{d}{D}\right)^2} \right\} \frac{6}{\pi d t^2}. \quad (2.8)$$

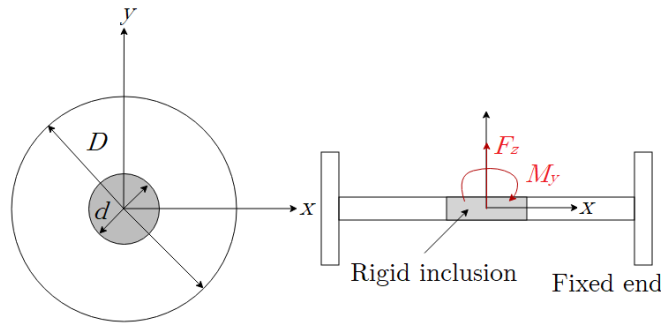


**Figure 2.10: Circular plate subjected to  $F_z$  and  $M_y$  [21]**

Furthermore, stress components  $\sigma_{rs}$ ,  $\sigma_{\theta s}$  and  $\tau_{r\theta s}$  due to the shear force  $F_x$  (Figure 2.11) are estimated as follows:

$$\begin{aligned} \sigma_{rs} &= -C_s F_x \cos(\theta) = -\frac{1}{\pi d t} F_x \cos(\theta), \quad \sigma_{\theta s} = \nu \sigma_{rs}, \\ \tau_{r\theta s} &= C_s F_x \sin(\theta) = \frac{1}{\pi d t} F_x \sin(\theta), \end{aligned} \quad (2.9)$$

whereas the shear stress at the nugget edge caused by the torsional moment applied to the center of a circular rigid inclusion (Figure 2.11) is estimated based on the following equation:

$$\tau_{r\theta T} = -C_T M_z = \frac{2}{\pi d^2 t} M_z. \quad (2.10)$$

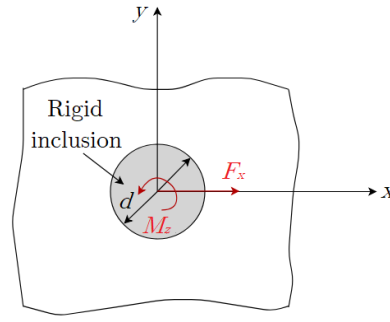


**Figure 2.11: Infinite plate subjected to  $F_x$  and  $M_z$  [21]**

Finally, the method of stress superposition is utilized to calculate nominal structural stress around the nugget periphery:

$$\sigma_{rsum} = C_p F_z + C_B(-M_y \cos(\theta) + M_x \sin(\theta)) - C_s(F_x \cos(\theta) + F_y \sin(\theta)),$$

$$\sigma_{\theta sum} = \nu \sigma_{rsum}, \quad (2.11)$$

$$\tau_{r\theta sum} = C_s(F_x \sin(\theta) + F_y \cos(\theta)) - C_T M_T.$$

The fatigue life of spot-welded joints is estimated based on the principal stresses calculated using the circumferential distribution of structural stress components:

$$\sigma_{p1}, \sigma_{p2} = \frac{(\sigma_{rsum} + \sigma_{\theta sum})}{2} \pm \frac{\sqrt{(\sigma_{rsum} - \sigma_{\theta sum})^2 + 4\tau_{r\theta sum}^2}}{2}. \quad (2.12)$$

Furthermore, Nakahara *et al.* [21] carried out a series of experimental tests of spot-welded specimens under multi-axial fatigue loading conditions and thus observed that the fatigue life of spot welds can be estimated based on the universal  $S-N$  curve. Hence, the proposed method does not make a distinction between pullout and interfacial failure.

The force-based fatigue life evaluation of spot-welded structures using *FEMFAT Spot* is based on the presented method and the experimentally determined master  $S-N$  curve [23]. The forces and moments required for the calculation of structural stresses are extracted from structural elements representing weld nuggets. Moreover, *FEMFAT Spot* offers the possibility to evaluate the fatigue life of spot-welded structures utilizing the stress-based approach, which extracts stresses in shell elements surrounding the weld nugget. Depending on the local load direction, the experimentally defined  $S-N$  curves are employed to calculate the accumulated damage [23]. In addition, Table 2.3 contains the properties of the master  $S - N$  curve utilized for the force-based fatigue life evaluation of spot-welded structures.

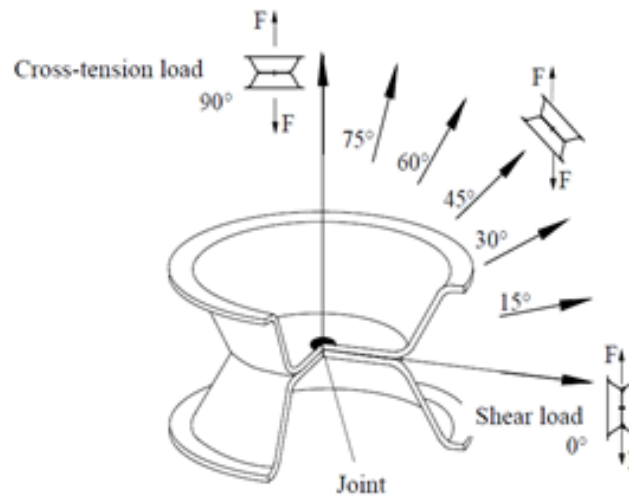
**Table 2.3: Properties of the master  $S - N$  curve [23]**

Slope, $b$	Cycle limit, $N$	$\sigma_N$ , MPa
5	$1 \cdot 10^6$	250

Table 2.4 contains the properties of seven different  $S - N$  curves depending on the local load direction (Figure 2.12), which are utilized for the stress-based fatigue life evaluation of spot-welded structures with *FEMFAT Spot*.

**Table 2.4: Properties of  $S - N$  curves for stress-based fatigue analysis [23]**

Loading direction	Slope, $b$	Cycle limit, $N$	$\sigma_N$ , MPa
$0^\circ$	5.8	$1 \cdot 10^6$	319
$15^\circ$	5.45		307
$30^\circ$	5.1		295
$45^\circ$	4.95		283
$60^\circ$	4.8		271
$75^\circ$	4.75		259
$90^\circ$	4.7		247

**Figure 2.12: Local loading direction [24]**

As evident, the endurance limit and the slope of the stress-based  $S - N$  curves decrease as the loading angle increases. Therefore, the cross-tension loading is the most unfavourable. In addition, it is important to emphasize that *FEMFAT Spot* modifies the endurance limit of spot  $S - N$  curves depending on the base material strength. That is to say, the increase of the base material ultimate tensile strength results in the increase of the spot endurance limit. Therefore, both the force-based method and stress-based fatigue life assessment of spot-welded structures using *FEMFAT Spot* are greatly influenced by the base material strength.

### 3 | Fatigue life assessment of spot-welded specimens using finite element analysis

In this chapter the results obtained by performing fatigue analyses of standard spot-welded specimens using *nCode DesignLife* and *FEMFAT Spot* are presented. The specimen geometry is presented in Figure 2.2. The following assumptions were applied while performing finite element analyses:

- Linear elastic material properties ( $E=210000$  N/mm<sup>2</sup>,  $\nu=0.3$ ),
- Material homogeneity, i.e. no distinction between the base metal, the heat affected zone and the weld nugget regarding the material properties,
- Contact between adjacent shell element meshes is neglected,
- Sheet metals are discretized using S4R shell elements,
- Nominal spot diameter is equal to 7 mm.

The aim of the conducted research was to determine:

- The effect of mesh refinement and mesh alignment,
- The effect of spot weld modelling,
- The effect of weld geometry and sheet thickness on the fatigue life of spot-welded specimens.



To study the effect of spot weld modelling, the weld nugget is represented with the following structural elements (Figure 3.1):

- B31 beam element connected to surrounding shell element mesh via kinematic coupling,
- B31 beam element connected to surrounding shell element mesh via 'spider' of B31 elements (which is supported only in *FEMFAT Spot*),
- C3D8R hexahedral element connected to surrounding shell element mesh via distributing coupling, which is known as Area Contact Method (ACM). The edge length of the hexahedral element is equal to  $a = \sqrt{\frac{d^2\pi}{4}}$  ( $d$  represents the weld nugget diameter). In addition, the height of the hexahedral element is equal to half the sum of shell element thicknesses [25–28].

The diameter of the beam element representing the weld nugget is equal to 7 mm, whereas the beam element length corresponds to half the sum of sheet thicknesses. The material properties assigned to the beam element are equal to the material properties of steel sheets, i.e.  $E=210\,000\text{ N/mm}^2$ ,  $\nu=0.3$ . Moreover, the diameter of beam elements utilized to couple the weld nugget to the shell element mesh is equal to 1 mm, while  $E=210\,000\text{ N/mm}^2$  and  $\nu=0.3$ .

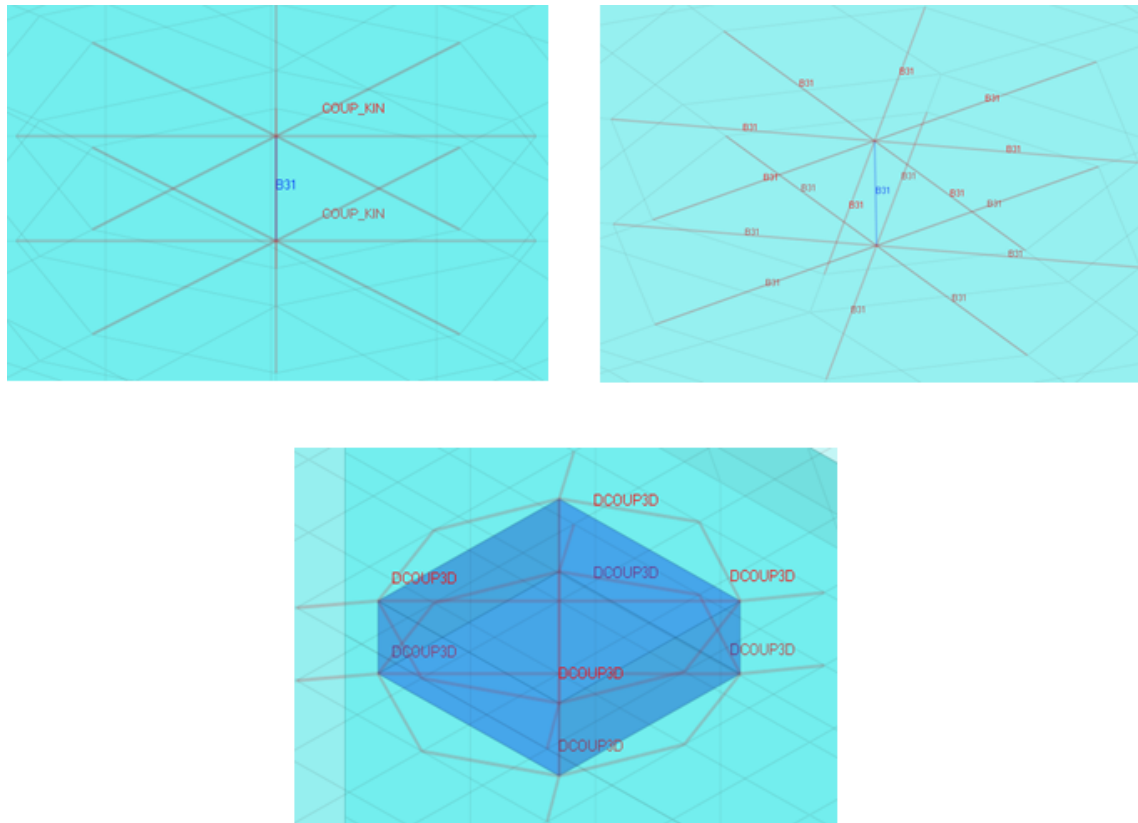
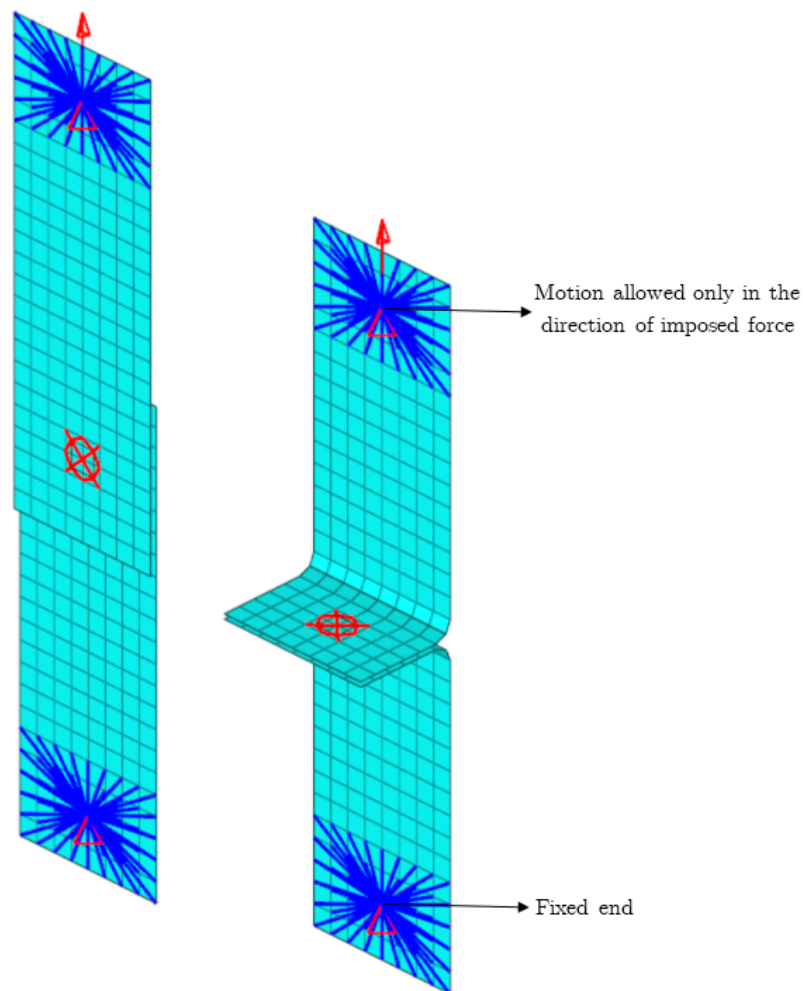


Figure 3.1: Structural elements representing the weld nugget

Based on the analysis of the effect of mesh refinement, mesh alignment and spot weld model representation, it was observed that the force-based fatigue life assessment using both *FEMFAT Spot* and *nCode DesignLife* is insensitive to mesh alignment and mesh refinement. Moreover, the conducted research indicates that *nCode Design Life* is insensitive to spot weld model representation, whereas *FEMFAT Spot* exhibits greater sensitivity to spot weld finite element representation. Since *FEMFAT Spot* and *nCode DesignLife* recommend using coarse shell element meshes for the force-based fatigue life assessment, in all subsequent analyses, the spot-welded specimens are meshed using S4R element with uniform size approximately equal to 5 mm x 5 mm, whereas the weld nugget is represented using ACM. However, it was observed that the stress-based approach implemented in *FEMFAT Spot* is sensitive to mesh refinement around the nugget circumference (see Appendix A). Since most engineering applications of finite element analysis demand quick and simple solutions, the coarse shell element mesh yields sufficiently accurate results and thus it was used in subsequent analyses. In addition, Figure 3.2 shows numerical models for the force-based fatigue analysis.



**Figure 3.2:** Numerical models of tensile shear and coach peel specimen for the force-based fatigue analysis

Furthermore, Figure 3.3 shows numerical models for the stress-based analysis using *FEMFAT Spot*, whereas Table 3.1 contains the mechanical properties of structural elements representing the spot-welded region.

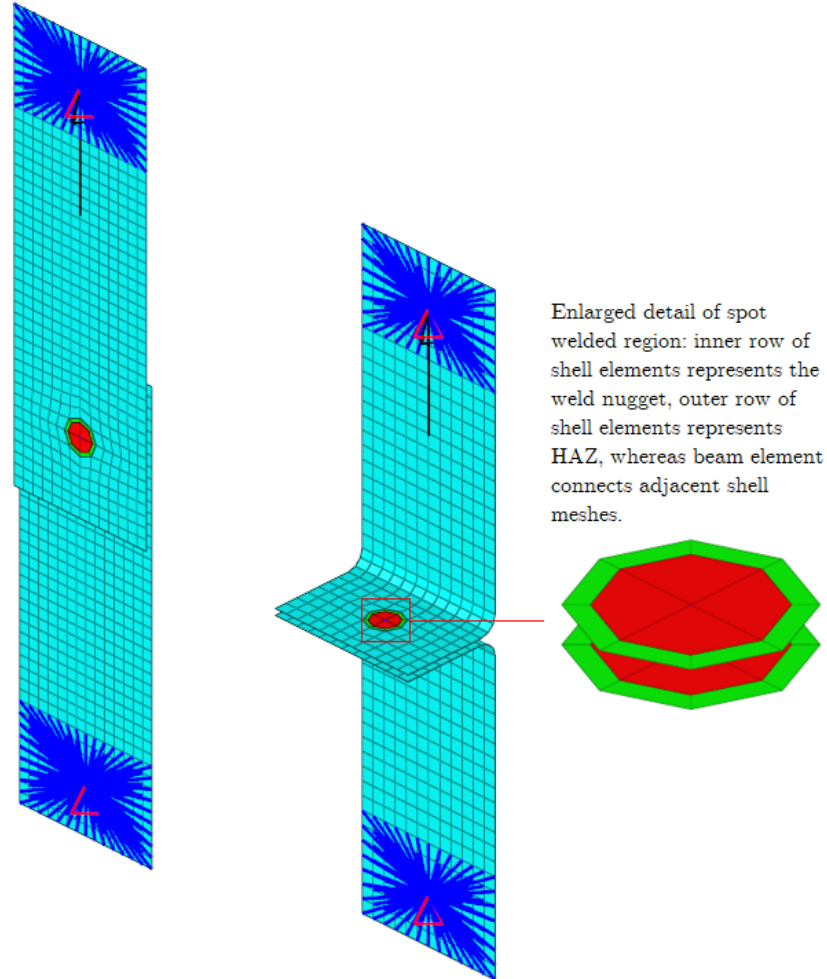


**Figure 3.3:** Numerical models of tensile shear and coach peel specimen for stress-based fatigue analysis

The nugget area for the stress-based fatigue life assessment consists of two rows of shell elements, whereas adjacent shell meshes are connected via B31 element. The inner row of shell elements represent the weld nugget, whereas the outer row of shell elements represents the heat affected zone with diameter equal to [29]:

$$D_{\text{HAZ}} = 1.3 \cdot d_{\text{NUGGET}}. \quad (3.1)$$

Since the weld nugget exhibits the highest hardness, *FEMFAT Spot* multiplies the modulus of elasticity of the base material to describe the rigid behavior of the weld nugget. The default multiplication factor defined is equal to 40, whereas it can be adjusted to suit specific applications.

Moreover, besides the definition of linear elastic material properties in the preliminary finite element analysis, *FEMFAT Spot* requires the definition of base material properties, which are then employed in the fatigue life prediction. Thus, Table 3.1 contains the material properties of HSLA340, DP600 and DP800, whereas the following figures present the corresponding Haigh diagrams.

**Table 3.1: Mechanical properties employed in the fatigue analysis using *FEMFAT Spot***

Material	$E$ , MPa	$\nu$	$\sigma_Y$ , MPa	$\sigma_{UTS}$ , MPa	$\sigma_N$ , MPa
HSLA340	210000	0.3	340	420	168
DP600			361	631	206
DP800			501	802	261

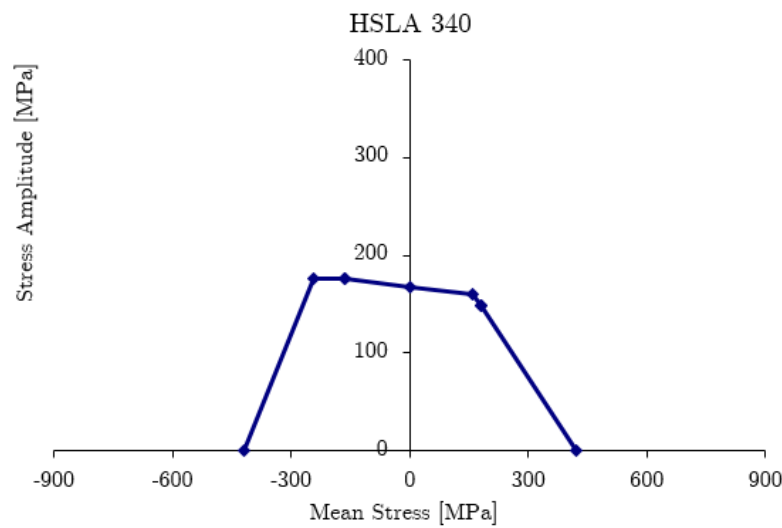


**Figure 3.4: HSLA340**

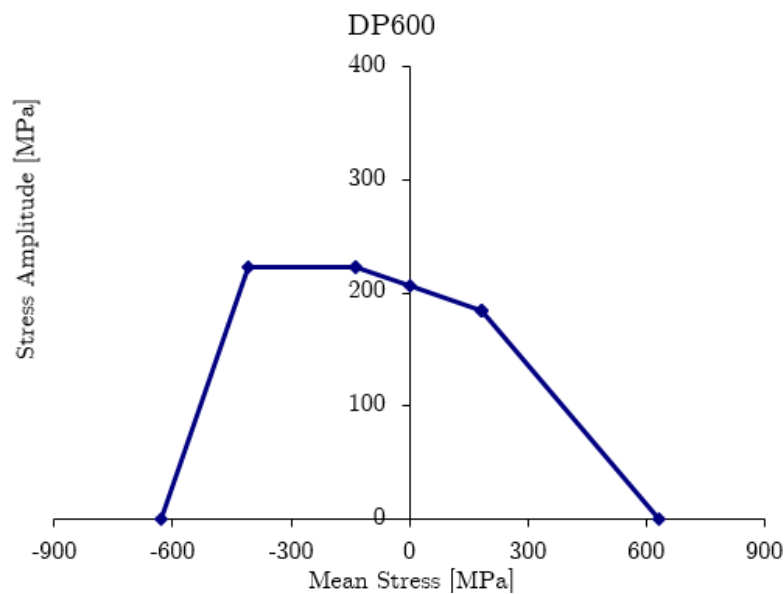


**Figure 3.5: DP600**

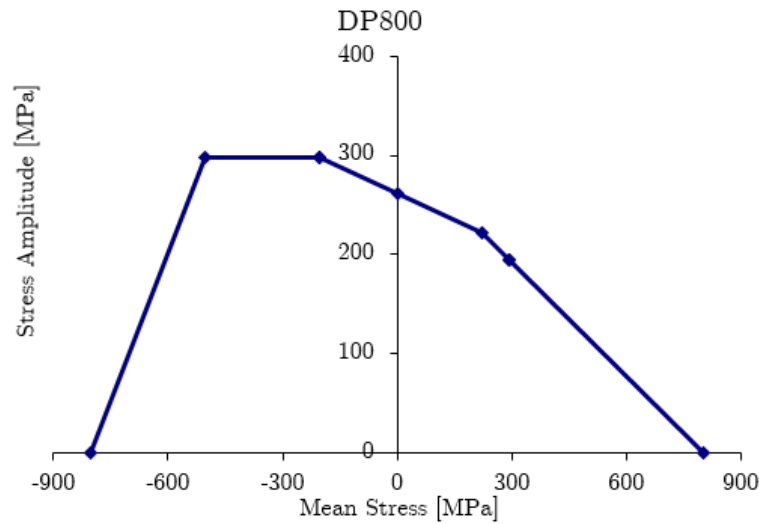


Figure 3.6: DP800

Furthermore, the following figure shows the comparison between the finite element results and the experimental data for specimens made of HSLA340 [14]. The nominal nugget diameter is 7 mm, whereas the sheet thickness is equal to 1.78 mm.

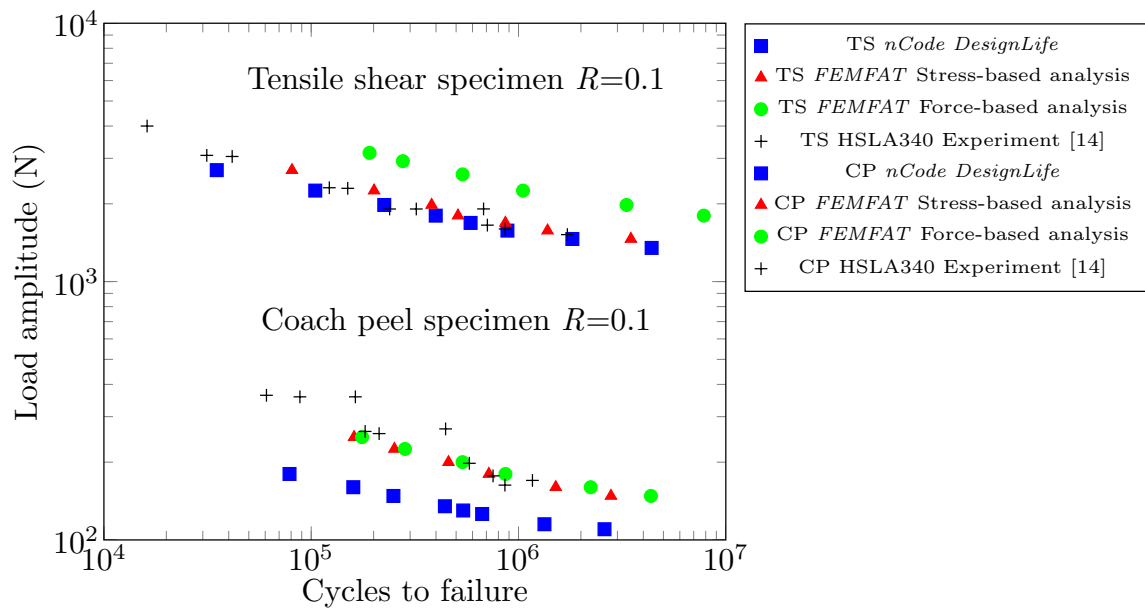


Figure 3.7: Comparison between the numerical results and the experimental data [14]

As evident, in the case of HSLA340, *nCode DesignLife* provides the lower limit of fatigue life, whereas the force-based approach implemented in *FEMFAT Spot* yields the upper limit of predicted fatigue life. However, the stress-based approach implemented in *FEMFAT Spot* yields a good correlation with the experimental results for tensile shear specimen made of HSLA340.

Moreover, the following figures show the effect of base material properties on the fatigue life of spot-welded specimens using *FEMFAT Spot*. For analyses purposes, the nominal weld diameter is equal to 7 mm.

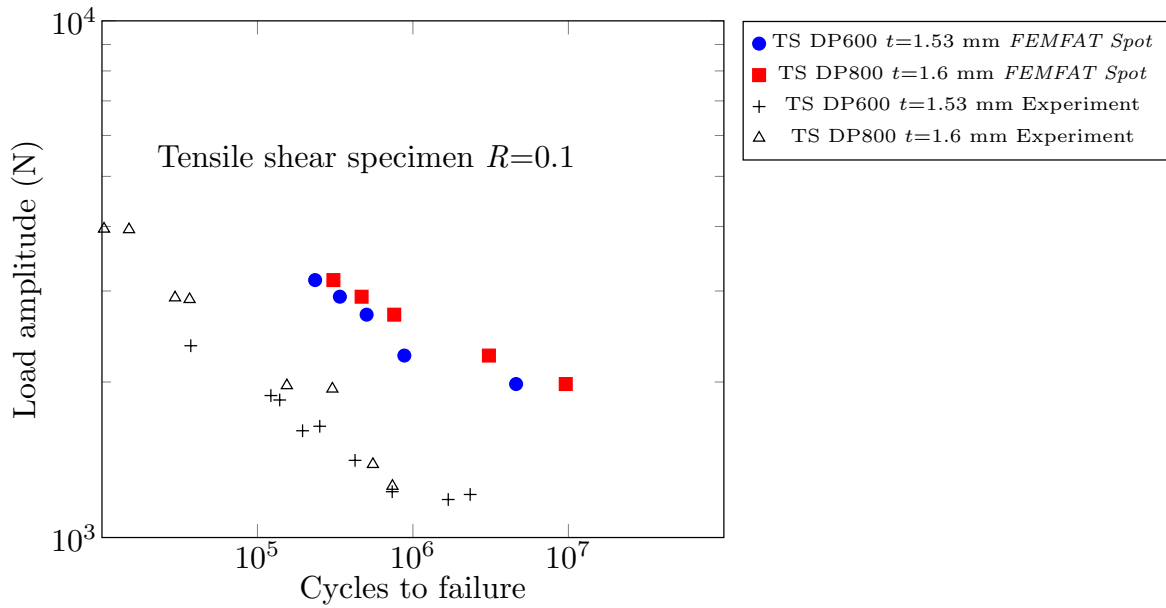


Figure 3.8: Comparison between the experimental [14] and numerical results obtained with *FEMFAT Spot*

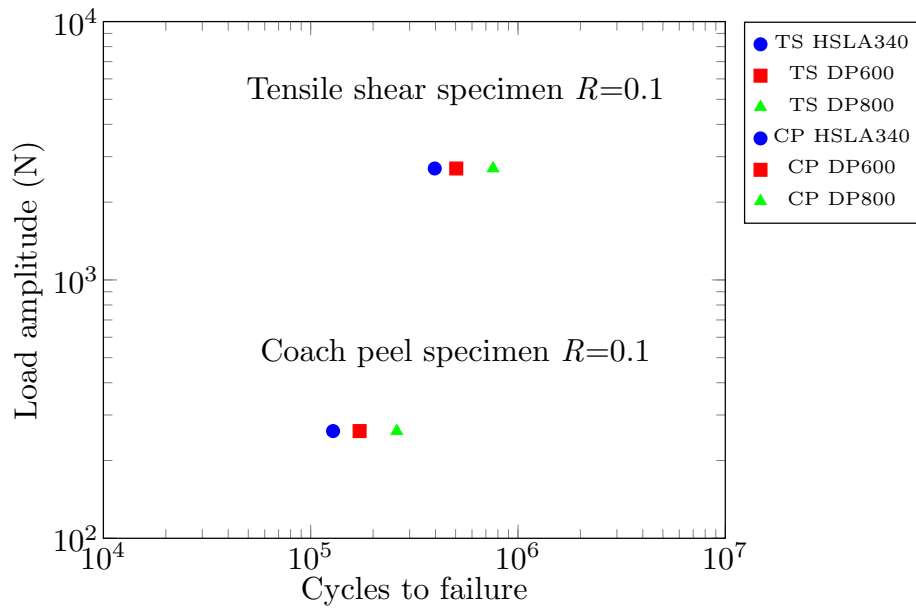


Figure 3.9: Effect of base material on fatigue life of spot-welded specimens using force-based approach implemented in *FEMFAT Spot*

The results presented above indicate that the evaluation of fatigue strength of spot-welded specimens with *FEMFAT Spot* greatly depends upon the base material strength. As shown in Figure 3.8, in the case of DP600 and DP800, *FEMFAT Spot* overestimates the number of cycles to failure of tensile shear specimen. Generally, *FEMFAT Spot* modifies the

endurance limit of the spot  $S-N$  curve, i.e. the increase of the ultimate tensile strength of the base material results in the increase of the endurance limit of the spot  $S-N$  curves, which enhances the durability of spot-welded specimens, as shown in Figure 3.9.

### 3.1 Effect of weld geometry and sheet thickness on fatigue life of spot-welded specimens

Since a large number of existing studies suggest that the fatigue life of spot-welded structures is mainly controlled by the geometric factors, the effect of nugget diameter and sheet thickness is examined. The subsequent analyses are carried out using *nCode DesignLife* to study the effect of weld geometry on the failure mode of spot-welded specimens. First, the effect of nugget diameter is examined, whereas the nominal sheet thickness is equal to 1.6 mm. The analysis results are presented in Figure 3.10.

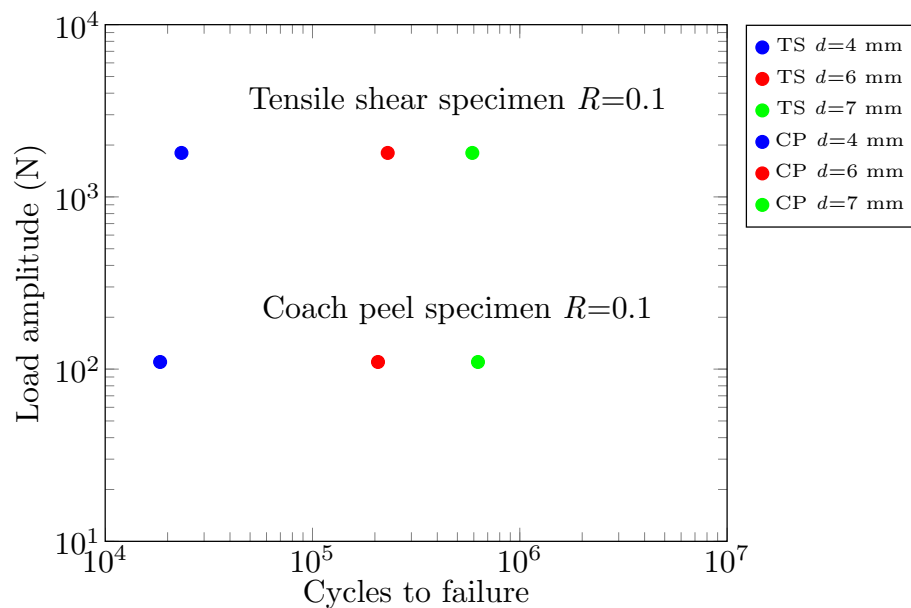
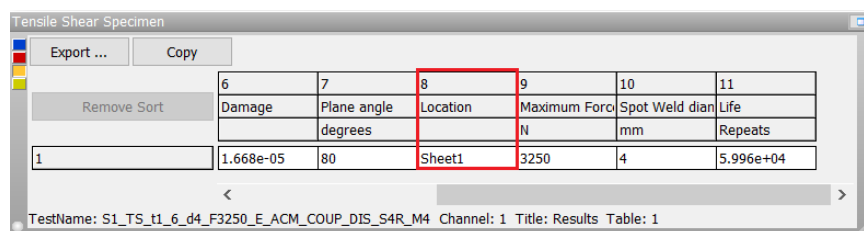


**Figure 3.10: The effect of nugget diameter on the fatigue life of spot-welded specimens-*nCode DesignLife***

According to Equations 2.4 and 2.5, the weld diameter influences the stress distribution around the nugget circumference, i.e. the increase of nugget diameter causes the decrease of structural stresses around the nugget periphery. Therefore, the results presented in Figure 3.10 indicate that the increase of the nugget diameter results in the improved durability of spot-welded specimens. However, *nCode DesignLife* implies that the nugget diameter equal to 4 mm is not sufficient to ensure pullout failure, i.e. the failure is initiated in the lower sheet of tensile shear specimen, as shown in Figure 3.11.



6	7	8	9	10	11
Damage	Plane angle	Location	Maximum Force	Spot Weld diameter	Life
	degrees		N	mm	Repeats
1	1.668e-05	80	Sheet1	3250	4
					5.996e+04

TestName: S1\_TS\_t1\_6\_d4\_F3250\_E\_ACM\_COUP\_DIS\_S4R\_M4 Channel: 1 Title: Results Table: 1

Figure 3.11: Interfacial failure - *nCode DesignLife*

In addition, Figure 3.12 displays the effect of sheet thickness on the fatigue behavior of spot-welded specimens.

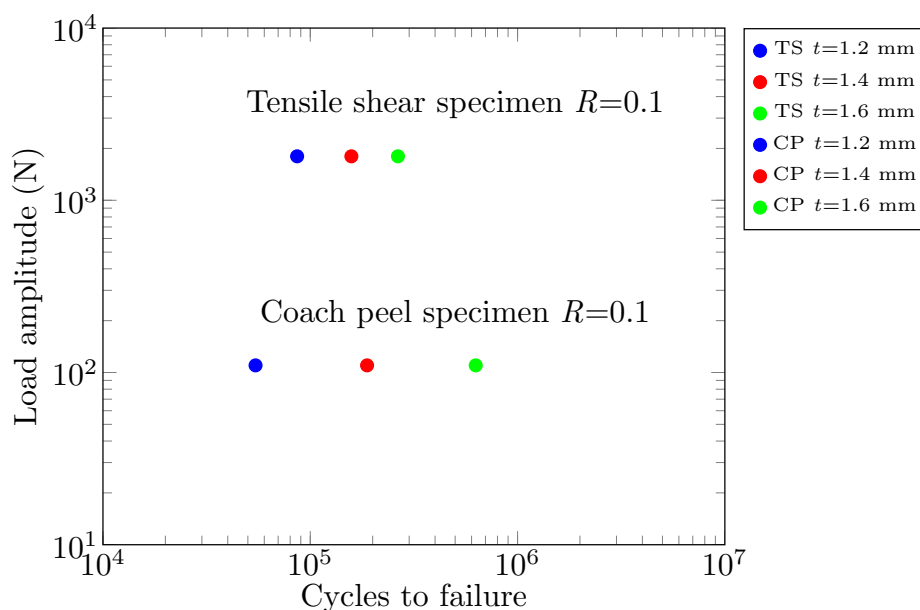
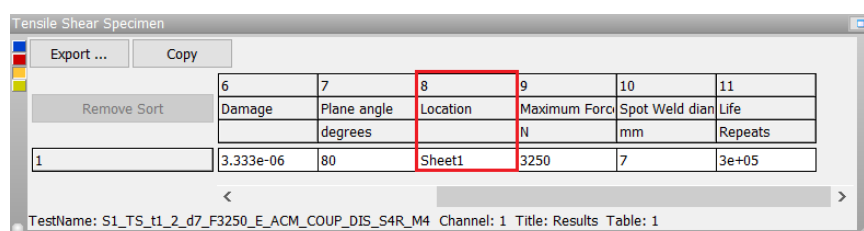


Figure 3.12: Effect of sheet thickness on the fatigue life of spot-welded specimens

According to Equations 2.4 and 2.5, the sheet thickness influences the stress distribution around the nugget circumference, i.e. the increase of sheet thickness causes the decrease of structural stresses around the nugget periphery. Therefore, the results shown in Figure 3.12 indicate that the increase of the sheet thickness results in the improved durability of spot-welded specimens. In addition, *nCode DesignLife* implies that 1.2 mm thick specimens failed in interfacial mode, as shown in Figure 3.13.



6	7	8	9	10	11
Damage	Plane angle	Location	Maximum Force	Spot Weld diameter	Life
	degrees		N	mm	Repeats
1	3.333e-06	80	Sheet1	3250	7
					3e+05

TestName: S1\_TS\_t1\_2\_d7\_F3250\_E\_ACM\_COUP\_DIS\_S4R\_M4 Channel: 1 Title: Results Table: 1

Figure 3.13: Interfacial failure - *nCode DesignLife*



## 3.2 Conclusions

From the results presented in the third chapter the following key findings emerge:

- Both the Rupp/LBF method implemented in *nCode DesignLife* and the force-based fatigue life assessment method implemented in *FEMFAT Spot* greatly simplify the fatigue analysis of spot-welded joints, at the same time capturing complex stress state around the nugget circumference under general loading conditions.
- The force-based approach implemented in *nCode DesignLife* is insensitive to mesh alignment, mesh refinement and the spot weld model representation.
- Due to the fixed ratio of the outer diameter of the circular plate  $D$  to the nugget diameter  $d$ , the Rupp/LBF method implemented in *nCode DesignLife* gives rather conservative results, i.e. structural stresses are overestimated. Hence, *nCode DesignLife* yields the lower limit of fatigue life.
- The force-based fatigue life assessment using *FEMFAT Spot* is insensitive to mesh refinement and mesh alignment. However, the results of the force-based fatigue analyses obtained using *FEMFAT Spot* exhibit greater sensitivity to the spot weld finite element representation compared to *nCode DesignLife*.
- The stress-based approach implemented in *FEMFAT Spot* is greatly influenced by the size of shell elements surrounding the weld nugget. That is to say, the decrease of shell element size leads to the increase of von Mises stress and thus the decrease of the number of cycles to failure.
- The fatigue life prediction of spot-welded specimens using *FEMFAT Spot* greatly depends upon the base material strength. *FEMFAT Spot* modifies the endurance limit of the master spot  $S - N$  curve for the force-based analysis and 7 different  $S - N$  curves employed in the stress-based analysis, although Nakahara *et al.* [14] originally neglected the effect of the base material properties. That is to say, the increase of the base material strength leads to the increase of the endurance limit of the aforementioned spot  $S - N$  curves. Therefore, both the stress-based method and the force-based approach implemented in *FEMFAT Spot* greatly depend upon the base material strength.

- Since the weld nugget and sheet thickness impact the stress distribution around the nugget circumference, the performed fatigue analysis with *nCode DesignLife* indicates that the aforementioned geometrical factors significantly influence the fatigue life of spot-welded specimens. That is to say, both the increase of the nugget diameter and the sheet thickness result in the decrease of structural stresses around the nugget periphery, which enhances the durability of spot-welded specimens.

To summarize, the following table gives a brief comparison of fatigue life prediction methods implemented in *FEMFAT Spot* and *nCode DesignLife*.

**Table 3.2:** Comparison of methods implemented in *FEMFAT Spot* and *nCode DesignLife*

	<i>FEMFAT Spot</i> Stress-based approach	<i>FEMFAT Spot</i> Force-based approach	<i>nCode DesignLife</i>
Linear elastic material properties	✓	✓	✓
Contact between welded sheets is neglected	✓	✓	✓
Extracts stresses in shell elements	✓	✗	✗
Extracts cross-sectional forces and moments	✗	✓	✓
Effect of restraint diameter	✗	✓	✗
Torsional loading	✓	✓	✗
Distinction between pullout and interfacial failure	✗	✗	✓
Effect of base material	✓	✓	✗

# 4 | Random vibration fatigue analysis

## 4.1 Introduction

Fatigue life evaluation of structures subjected to a constant amplitude loading is performed in the time domain based on the rainflow cycle counting method and Palmgreen-Miner linear damage accumulation rule. However, vehicle components are during anticipated operational time seldom subjected to a constant amplitude cyclic loading, i.e. the excitation amplitudes, phase and frequency content are random in nature and caused by different sources, such as irregular road profile. Random excitation causes dynamic stress/strain response, therefore random vibration fatigue analysis is carried out in the frequency domain to ensure that the resonance will not be invoked during the operational time of the observed structures [30–32]. In addition, modal analysis enables sufficiently accurate calculation of natural frequencies and predicts the local response of observed system, thus playing a vital role in the random vibration fatigue life assessment.

As previously mentioned, due to the stress concentration around the weld nugget circumference, spot welds are prone to premature fatigue failure. Hence, understanding the mechanical behavior of spot welds subjected to random excitation is crucial for evaluating both durability and noise, vibration and harshness. Moreover, the subsequent sections cover the basic principles of signal processing and spectral fatigue analysis, whereas the procedure of random vibration fatigue analysis of spot-welded structures using *nCode DesignLife* is described in the last section of this chapter.

## 4.2 Signal processing

Generally, signals can be classified into two main categories, i.e. deterministic and random (non-deterministic) signals [33], as shown in Figure 4.1. Random, stochastic or non-deterministic signals are unpredictable in a manner that future states cannot be predicted from past states using a closed-form solution. Hence, it is necessary to introduce statistical variables to describe the excitation source and the response of the observed system.

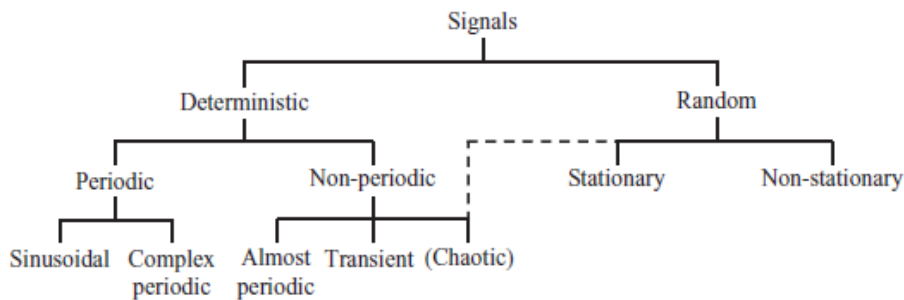


Figure 4.1: Signal classification [33]

Furthermore, due to their complex nature, continuous time-domain random signals are discretized and transformed to the frequency domain using Fast Fourier Transformations<sup>7</sup> [33]. Although the amplitude of applied excitation constantly changes, most random processes influencing the fatigue life of structures follow a zero-mean Gaussian probability distribution, which can be observed by plotting the probability density function<sup>8</sup> (PDF) [32–35], as shown in Figure 4.2.

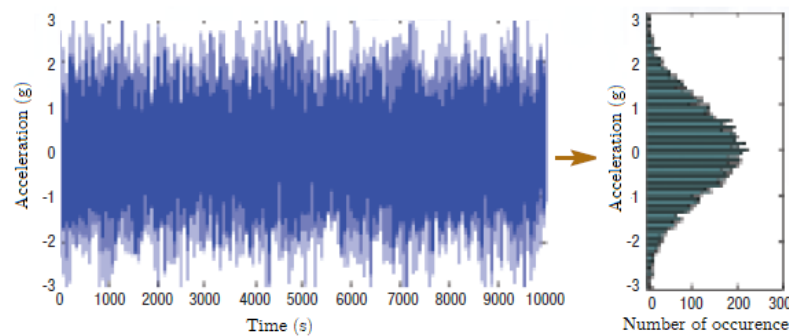


Figure 4.2: Time domain waveform and probability density function of random excitation [35]

<sup>7</sup>FFT is the most commonly used method to transform a random signal in time domain into frequency domain and vice versa. Moreover, FFT provides a unique representation of the original signal, i.e. the total energy of a signal in time domain is equal to the total energy over frequency spectrum (equality known as Parseval's theorem) [33].

<sup>8</sup>PDF describes the probability of a variable reaching a certain value, i.e. PDF represents the number of occurrence of a particular amplitude reached in a certain frequency band.

The probability density function enables the statistical description of a random excitation, thus providing the possibility to estimate the accumulated fatigue damage. Therefore, even though random vibrations are unpredictable, they exhibit some form of statistical regularity and can be characterized statistically.

Due to the complexity of stochastic signals and the inability to accurately evaluate the response of a structure under constantly changing amplitudes of applied excitation, the average value of all amplitudes within a given frequency range is often evaluated. Hence, the applied excitation is usually described in the frequency domain using Power spectral density (PSD) [34–39], which is a mathematical description of the average spectral content of a random time signal. Additionally, PSD is equal to the mean square of the observed signal at a given frequency band [30, 31] and it is calculated from a signal in time domain using the following equation [40]:

$$S(\omega) = \frac{|\text{FFT}|^2}{f_s \cdot N}, \quad (4.1)$$

where  $|\text{FFT}|$  represents the amplitude of the original signal at a certain frequency band (after performing FFT operation),  $f_s$  is the sampling frequency, whereas  $N$  is the number of samples. To summarize, the following features of PSD functions and their application are highlighted:

- PSD is equal to the mean-square value of a signal being analyzed (it does not refer to the physical quantity of power),
- PSD represents the distribution of a signal's power content over a given frequency spectrum,
- The amplitude of the PSD is normalized with respect to the spectral resolution utilized for signal discretization,
- Performing random vibration analysis in the frequency domain with excitation specified in terms of PSD greatly simplifies the procedure and enables the use of efficient FE approach based on the calculation of linear frequency response functions, instead of performing transient analysis in the time domain.

### 4.3 Random vibration fatigue analysis

Random vibration can be described as a motion that varies randomly with respect to time, hence the instantaneous amplitude of a random vibration cannot be characterized as an exact function of time. In addition, random vibrations are composed of a continuous frequency spectrum, thus numerous natural frequencies of structures may be excited simultaneously in the defined frequency range.

When a structure is subjected to random excitation, first the input continuous signal in time domain is discretized and transformed into frequency domain using FFT. Secondly, steady-state linear dynamic analysis<sup>9</sup> under continuous unit harmonic excitation is performed to obtain frequency response functions (FRF), which establish the correlation between input excitation and response of the analyzed system [41–44]. In addition, frequency response functions depend upon inherent characteristics of structures (i.e. mass, damping and stiffness). The general equation of motion of a multiple degree of freedom system (MDOF) subjected to harmonic excitation is expressed as follows:

$$\mathbf{M} \cdot \ddot{\mathbf{x}}(t) + \mathbf{C} \cdot \dot{\mathbf{x}}(t) + \mathbf{K} \cdot \mathbf{x}(t) = \mathbf{F}(t), \quad (4.2)$$

where  $\mathbf{M}$  is the mass matrix,  $\mathbf{C}$  is the damping matrix,  $\mathbf{K}$  is the stiffness matrix,  $\mathbf{F}(t)$  is the excitation vector, whereas  $\mathbf{x}(t)$  is the displacement vector. Moreover, when performing steady-state linear dynamic analysis utilizing the modal superposition technique, the first step is the modal transformation of the displacement vector  $\mathbf{x}(t)$ :

$$\mathbf{y}(\mathbf{t}) = \boldsymbol{\Phi}_1 \cdot z_1 + \dots + \boldsymbol{\Phi}_n \cdot z_n = \boldsymbol{\Phi}_n \cdot \mathbf{z}, \quad (4.3)$$

where  $\boldsymbol{\Phi}$  is the mode shape vector, which defines vibration pattern of the observed system at a specific natural frequency, whereas  $\mathbf{z}$  presents the vector of modal coordinates. Therefore, the basic assumption employed in the modal superposition technique is that the displacement vector can be written as a linear combination of the eigenmodes. Moreover, referring to Equation (4.3), the general equation of motion is expressed using the following relation:

$$\mathbf{M} \cdot \boldsymbol{\Phi} \cdot \ddot{\mathbf{y}}(\mathbf{t}) + \mathbf{C} \cdot \boldsymbol{\Phi} \cdot \dot{\mathbf{y}}(\mathbf{t}) + \mathbf{K} \cdot \boldsymbol{\Phi} \cdot \mathbf{y}(\mathbf{t}) = \mathbf{F}(\mathbf{t}). \quad (4.4)$$

---

<sup>9</sup>Steady-state linear dynamic (SSD) analysis predicts the linear response of a structure subjected to harmonic excitation as a function of frequency of the imposed excitation. Moreover, SSD is performed based either on a direct or a mode-based frequency response analysis [41].

Multiplication of Equation (4.4) by  $\Phi^T$  results in a set of uncoupled equations of motion:

$$\mathbf{M}_\Phi \cdot \ddot{\mathbf{y}}(t) + \mathbf{C}_\Phi \cdot \dot{\mathbf{y}}(t) + \mathbf{K}_\Phi \cdot \mathbf{y}(t) = \mathbf{F}_\Phi, \quad (4.5)$$

where:

$$\begin{aligned} \mathbf{M}_\Phi &= \Phi^T \cdot \mathbf{M} \cdot \Phi, & \mathbf{K}_\Phi &= \Phi^T \cdot \mathbf{K} \cdot \Phi, \\ \mathbf{C}_\Phi &= \Phi^T \cdot \mathbf{C} \cdot \Phi, & \mathbf{F}_\Phi &= \Phi^T \cdot \mathbf{F} \cdot \Phi. \end{aligned} \quad (4.6)$$

Moreover, modal equations are transformed into the frequency domain, which enables the calculation of the frequency response functions based on the following equation:

$$\mathbf{Y}_\Phi(\omega) = \mathbf{H} \cdot \mathbf{F}_\Phi(\omega), \quad (4.7)$$

where  $\mathbf{H}$  represents the matrix of frequency response functions. Finally, the response power spectral density is estimated based on the following equation:

$$S_x(\omega) = |\mathbf{H}|^2 \cdot S_f(\omega), \quad (4.8)$$

where  $S_f(\omega)$  is the imposed PSD. Since the input excitation is most frequently defined as the Acceleration spectral density, FE solvers transform the acceleration response into the stress response based on the existing stress criteria. Most commonly utilized stress criteria to calculate the stress response PSD are signed von Mises stress approach, Absolute Maximum Principal Stress approach or Critical plane method, which is highlighted as the most accurate approach when performing multi-axial random vibration fatigue life evaluation [45, 46]. Therefore, the objective of the aforementioned criteria is to convert the obtained local stress PSD data into a form suitable for the calculation of the accumulated damage. The PSD-based rainflow cycle counting is accomplished using spectral moments, which condense the information carried by the PSD into scalar quantities, as shown in Figure 4.3. Most importantly, spectral moments describe the probability density function of the stress range, which enables the calculation of the accumulated fatigue damage. In addition, the  $n^{th}$  spectral moment is calculated as follows [44, 47–49]:

$$m_n = \int_0^\infty f^n W(f) df = \sum f_s^n W_s(f) \delta f. \quad (4.9)$$

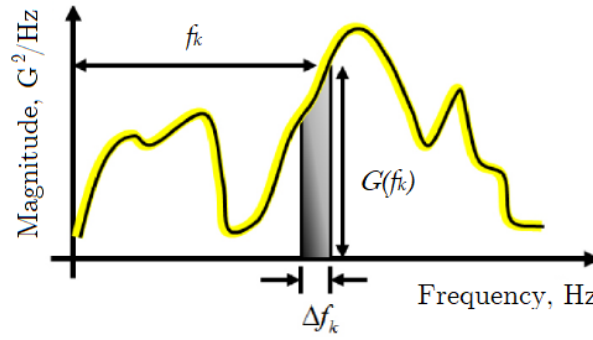


**Figure 4.3:** Calculation of spectral moments [44]

The zeroth, second and fourth spectral moments can be combined to fully characterize the random response and are utilized to statistically describe response variables, thus enabling the estimation of the accumulated fatigue damage. The most significant parameters describing random signals are the expected number of zero crossings  $E[0]$ , the expected number of peaks  $E[P]$  and the irregularity factor  $\alpha^{10}$  [47–51], which are calculated based on spectral moments:

$$\begin{aligned} E[0] &= \sqrt{\frac{m_2}{m_0}}, \\ E[P] &= \sqrt{\frac{m_4}{m_2}}, \\ \alpha &= \frac{E[0]}{E[P]}. \end{aligned} \quad (4.10)$$

Furthermore, the expected number of zero crossing  $E[0]$ , the expected number of peaks  $E[P]$  and the irregularity factor  $\alpha$  are utilized to calculate the probability density function of the stress range, thus providing the basis for calculation of the accumulated damage. The existing methods which enable the estimation of PDF of the stress range assume the following properties of random excitation [33]:

- Stationarity, which imposes the time - invariance of statistical variables describing stochastic processes,
- Ergodicity, i.e. all statistical variables characterizing random excitation can be obtained from any of its single realizations,
- Gaussian probability distribution.

<sup>10</sup>Irregularity factor measures the bandwidth of a random process and varies between 0 and 1. Hence,  $\alpha$  characterizes the nature of random signals, i.e. it differentiates narrow band and wide band processes. If  $\alpha$  approaches 1, a process is narrow band and is characterized by only one central frequency, which indicates that the number of zero crossings is approximately equal to the number of peaks. However,  $\alpha$  of wide band processes tends to zero, indicating a much more complex relationship between the zero crossing and the number of peaks [36–39].



Most commonly used methods to predict the PDF of the stress range are Lalanne, Steinberg, Narrow Band and Dirlik [19,34,36–39]. Lalanne's approach assumes the following probability density function of the stress range:

$$N(S) = E[P] \cdot p(S). \quad (4.11)$$

In Equation (4.11),  $N(S)$  represents the number of stress cycles expected per second, whereas the probability density function of the stress range is defined using the following equation:

$$p(S) = \frac{1}{2RMS} \left\{ \frac{\sqrt{1-\gamma^2}}{\sqrt{2\pi}} e^{\frac{-S^2}{8RMS^2(1-\gamma^2)}} \right\} + \frac{S \cdot \gamma}{4RMS} e^{\frac{-S^2}{8RMS^2}} \left[ 1 + \operatorname{erf} \left( \frac{S \cdot \gamma}{2RMS \sqrt{2(1-\gamma^2)}} \right) \right], \quad (4.12)$$

where:

$$\operatorname{erf}(x) = \frac{2}{\sqrt{\pi}} \int_0^x e^{-t^2} dt \quad \text{and} \quad RMS = \sqrt{m_0}. \quad (4.13)$$

Secondly, Dirlik defined  $p(S)$  as follows:

$$p(S) = \frac{\frac{D_1}{Q} \cdot e^{\frac{-Z}{Q}} + \frac{D_2 \cdot Z}{R^2} \cdot e^{\frac{-Z^2}{2 \cdot R^2}} + D_3 \cdot Z \cdot e^{\frac{-Z^2}{2}}}{2 \cdot \sqrt{m_0}}, \quad (4.14)$$

where:

$$\begin{aligned} D_1 &= \frac{2 \cdot (x_m - \gamma^2)}{1 + \gamma^2}, \quad D_2 = \frac{1 - \gamma - D_1 + D_1^2}{1 - R}, \quad D_3 = 1 - D_1 - D_2, \\ Z &= \frac{S}{2 \cdot \sqrt{m_0}}, \quad q = \frac{1.25 \cdot (\gamma - D_3 - D_2 \cdot R)}{D_1}, \quad R = \frac{\gamma - x_m - D_1^2}{q - \gamma - D_1 + D_1^2} \quad \text{and} \quad (4.15) \\ x_m &= \frac{m_1}{m_0} \cdot \sqrt{\frac{m_2}{m_4}}. \end{aligned}$$

Furthermore, the Narrow Band approach assumes the Rayleigh distribution of the probability density function of the stress range:

$$N(S) = E[P] \cdot \frac{S}{4 \cdot m_0} \cdot e^{\frac{S^2}{8 \cdot m_0}}. \quad (4.16)$$

Due to the assumption that each peak is matched with a corresponding valley of similar magnitude (Figure 4.4), the damage calculated using the Narrow Band approach is overestimated when broad band signals are being processed<sup>11</sup>. Hence, the Narrow band approach generally yields a conservative solution.

<sup>11</sup>Broad band signals are characterized in the time domain by a large number of smaller waves, i.e. since the irregularity factor  $\alpha$  tends to zero,  $E[P]$  does not correspond to  $E[0]$  [19].

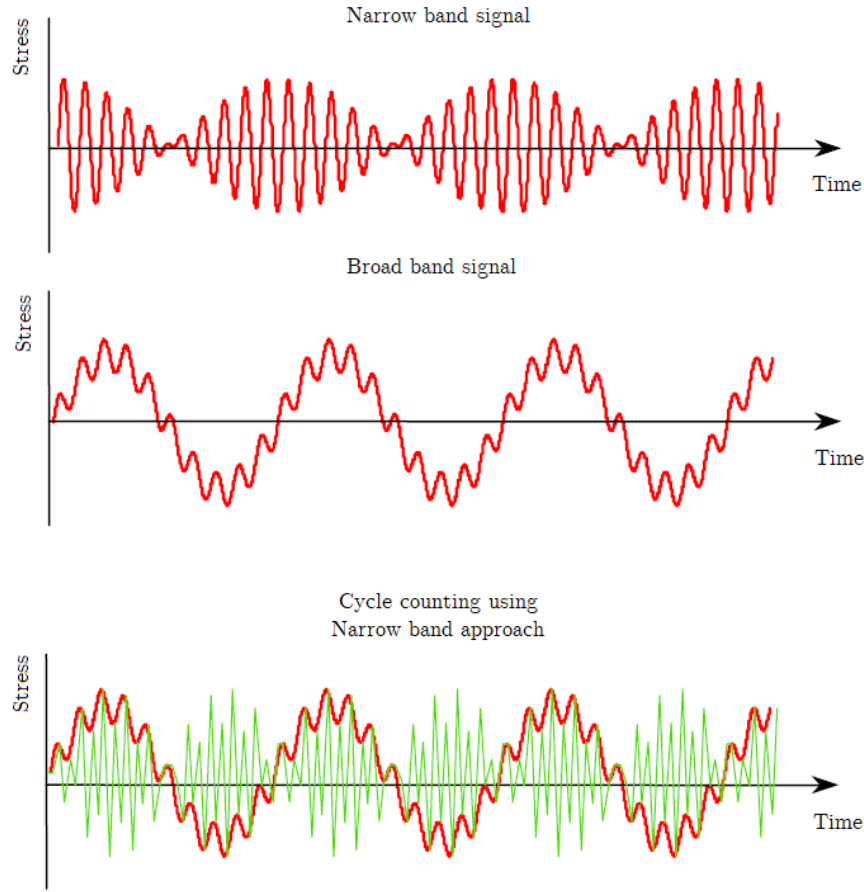


Figure 4.4: Comparison of narrow band and broad band time signal [19]

Lastly, Steinberg's three band method assumes that the probability density function follows a Gaussian distribution, thus the expected values of stress amplitudes are bounded by discrete probability levels:

$$N(S) = E[P] \cdot \begin{cases} 0.683, & \text{at } 2 \cdot RMS, \\ 0.271, & \text{at } 4 \cdot RMS, \\ 0.043, & \text{at } 6 \cdot RMS. \end{cases} \quad (4.17)$$

To summarize, since the stress history is not available, the aforementioned probability methods are introduced to estimate stress histogram, i.e. the amplitude distribution of the local PSD stress response. In addition, the accumulated damage is calculated based on the probability density function of the stress range utilizing the Palmgreen-Miner rule [43, 50, 51]:

$$D = \frac{E[P]T}{k} \sum_0^{\infty} S_r^b \cdot p(S_r), \quad (4.18)$$

where  $E[P]$  is the expected number of fatigue cycles per second,  $T$  is the exposure time,  $k$  is the material fatigue strength coefficient,  $b$  is the material fatigue exponent,  $S_r$  is the stress range and  $p(S_r)$  is the probability density function of the stress range.

## 4.4 Random vibration fatigue of spot welds using *nCode DesignLife*

The fatigue life evaluation of spot-welded structures subjected to random excitation using *nCode DesignLife* is performed utilizing the modified Rupp/LBF method. Based on the input PSD, transfer functions and nodal forces and moments extracted from the preliminary linear steady-state dynamic analysis, *nCode DesignLife* estimates the PSD of structural stress response around the nugget circumference both in the weld nugget and the spot-welded sheets. Moreover, the probability methods described in the previous chapter are implemented in *nCode DesignLife* to calculate the probability density function of the stress range. In addition, a schematic representation of a general algorithm for the random vibration fatigue analysis of spot-welded structures is shown in Figure 4.5, whereas Figure 4.6 shows the analysis model used to evaluate the random vibration fatigue life procedure using *nCode DesignLife*.

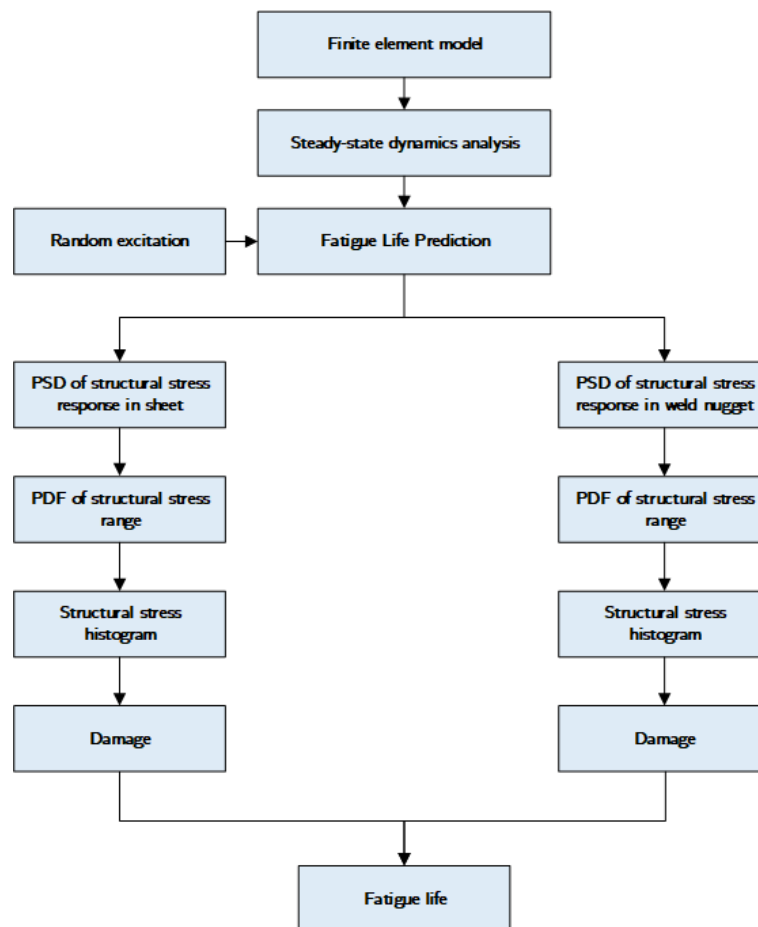
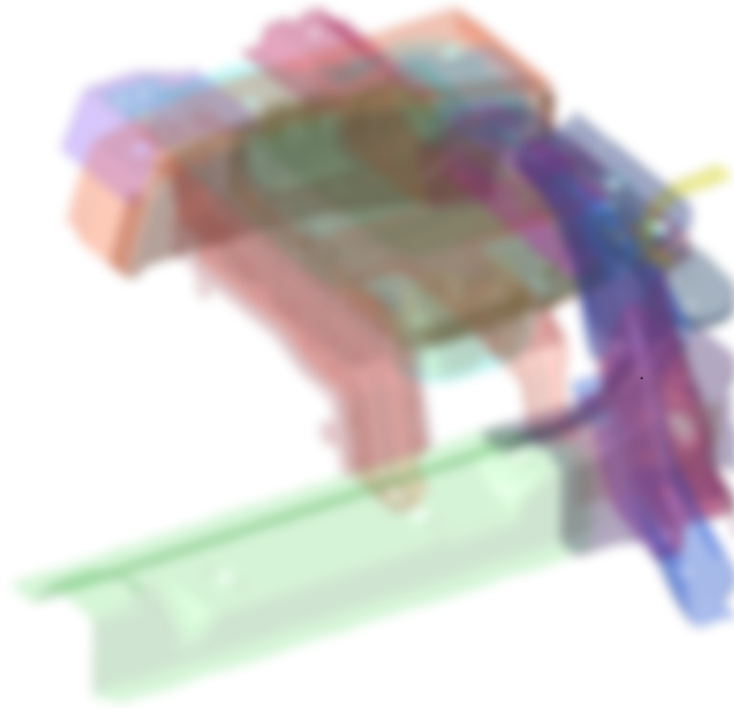
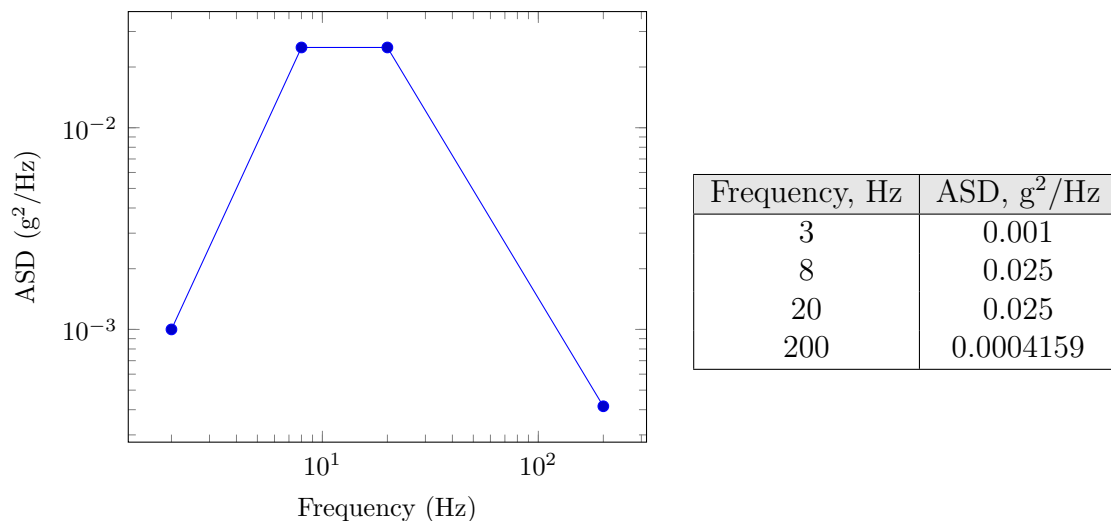


Figure 4.5: Schematic representation of random vibration fatigue life evaluation procedure of spot-welded structures



**Figure 4.6: Analysis model**

The accumulated damage was estimated by performing separate single-axis acceleration tests and subsequently summing damage values for each test. Figure 4.7 displays the input acceleration spectral density, whereas the exposure duration was 180 000 s. In addition, spot welds are represented using the Area Contact Method (C3D8R elements connected to the surrounding shell element mesh via distributing coupling).



**Figure 4.7: Input acceleration spectral density**

Furthermore, the following tables contain the values of the irregularity factor, root mean square of stress response and damage accumulated in the critical spot welds. The aforementioned values are obtained using different probabilistic models.

**Table 4.1: Comparison of results for X-axis direction test**

Element 4603362	Irregularity factor $\alpha$	RMS Stress, MPa	Accumulated damage
Lalanne	0.826	13.44	$3.27 \cdot 10^{-7}$
Dirlik			$2.98 \cdot 10^{-7}$
NarrowBand			$3.906 \cdot 10^{-7}$
Steinberg			$2.467 \cdot 10^{-7}$
Element 4603506	Irregularity factor $\alpha$	RMS Stress, MPa	Accumulated damage
Lalanne	0.788	12.61	$1.313 \cdot 10^{-7}$
Dirlik			$1.25 \cdot 10^{-7}$
NarrowBand			$1.052 \cdot 10^{-7}$
Steinberg			$1.666 \cdot 10^{-7}$

**Table 4.2: Comparison of results for Y-axis direction test**

Element 4603362	Irregularity factor $\alpha$	RMS Stress, MPa	Accumulated damage
Lalanne	0.9043	29.57	0.001613
Dirlik			0.001527
NarrowBand			0.001783
Steinberg			0.001128
Element 4603506	Irregularity factor $\alpha$	RMS Stress, MPa	Accumulated damage
Lalanne	0.8961	33.57	0.005909
Dirlik			0.005605
NarrowBand			0.006592
Steinberg			0.004212

**Table 4.3: Comparison of results for Z-axis direction test**

Element 4603362	Irregularity factor $\alpha$	RMS Stress, MPa	Accumulated damage
Lalanne	0.8949	64.59	1.628
Dirlik			1.402
NarrowBand			1.852
Steinberg			1.774
Element 4603506	Irregularity factor $\alpha$	RMS Stress, MPa	Accumulated damage
Lalanne	0.8922	74.61	4.59
Dirlik			3.776
NarrowBand			4.86
Steinberg			4.938

The cumulative fatigue damage  $D_T$  is simply calculated as the sum of the damage accumulated during each individual test:

$$D(f) = \sum D_i(f). \quad (4.19)$$

According to Steinberg's approach, the highest damage is accumulated in the spot weld represented with the hexahedral element 4603506:

$$D = 4.942, \quad (4.20)$$

which indicates that the particular spot weld fails under the imposed random excitation. The following table presents the comparison of the cumulative damage estimated using the Dirlik, Lalanne and Narrow Band approach with respect to the Steinberg method, whereas the location of the critical spot weld is displayed in Figure 4.8.

**Table 4.4: Comparison of cumulative damage values**

Method	Accumulated damage	$E_{\text{rel}}^{12}$
Steinberg	4.942	-
NarrowBand	4.86	-1.65 %
Lalanne	4.59	-7.1 %
Dirlik	3.776	-23.6 %

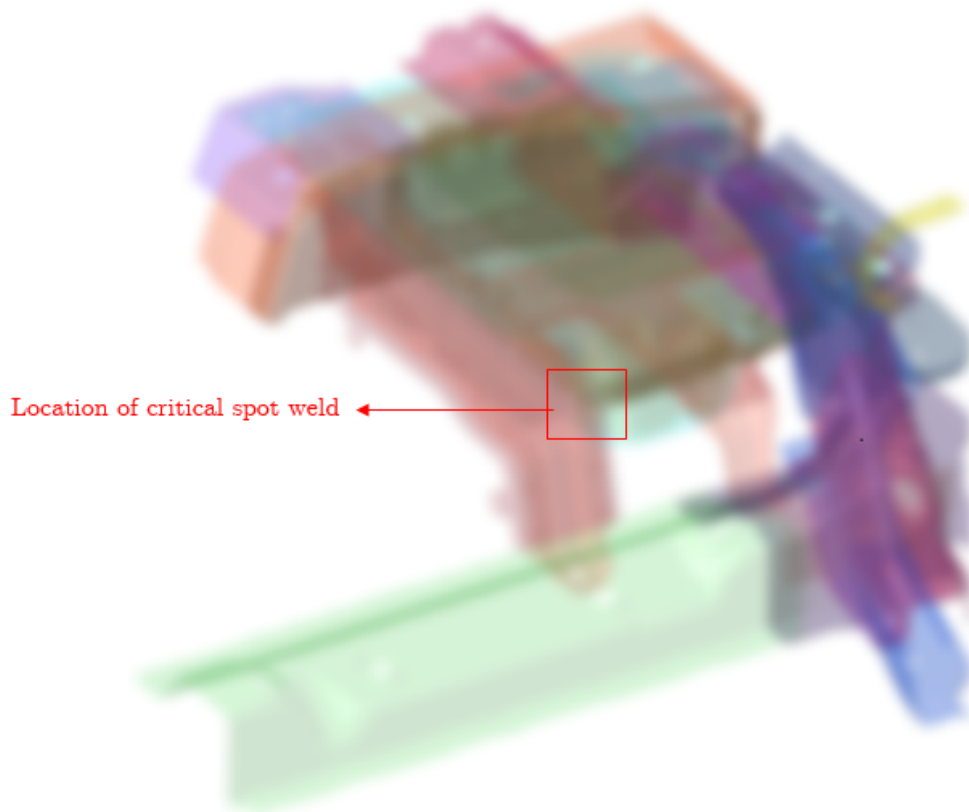


**Figure 4.8: Location of critical spot weld**

<sup>12</sup> $E_{\text{rel}}$  refers to the relative change between two quantities calculated as  $E_{\text{rel}} = \left( \frac{x - x_{\text{reference}}}{x_{\text{reference}}} \right) \cdot 100$ .

# 5 | Damage analysis of spot welded joints

## 5.1 Introduction

Recent developments in vehicle crash analyses have made a significant impact on design optimization and vehicle crashworthiness, thus reducing the time and cost of full-scale experiments and design changes. The most significant parameters dictating the behavior of vehicle components during crashing and hence essential to preserve the integrity of passenger compartment are the kinetic energy absorption and crash resistance [52]. Moreover, the tendency to enhance vehicle crashworthiness is frequently in competition with achieving lightweight and fuel efficient design. Since spot welds play an important role during vehicle crash, it is crucial to understand the mechanical behavior of spot-welded joints under dynamic loading conditions to balance design objectives, ensure passenger's safety and reduce design cycle time.

Failure modes of spot-welded joints under crash loading conditions result from a complex interrelation between the weld geometry and the mechanical properties of spot-welded region [53–61]. Two primary failure modes of spot welds under dynamic loading conditions are interfacial and pullout failure. As an example, during tensile shear testing, the weld nugget first rotates to align with the imposed force direction, which causes the distribution of shear stress at the faying interface and tensile stress around the nugget circumference. If the shear stress exceeds the nugget shear strength before the tensile stress can cause plastic deformation around the weld nugget, interfacial failure occurs, indicating poor weld quality due to low energy absorption and load carrying capability [53, 54]. In contrast, pullout failure occurs when tensile stresses around the nugget circumference cause plastic deformation, i.e. necking in the base material or HAZ (Figure 5.1). Moreover, necking develops unevenly in both sheets, causing stress

concentration. As the region in which necking occurs is continually stressed, the weld nugget will be eventually completely pulled out from the base material, leaving the hole in the other sheet [53, 54]. Hence, the driving force for the pullout failure is tensile stress distributed around the nugget circumference. In addition, pullout failure is common for larger nugget diameters due to the increased overall bond area, which results in a higher energy absorption and load carrying capability (Figure 5.2).

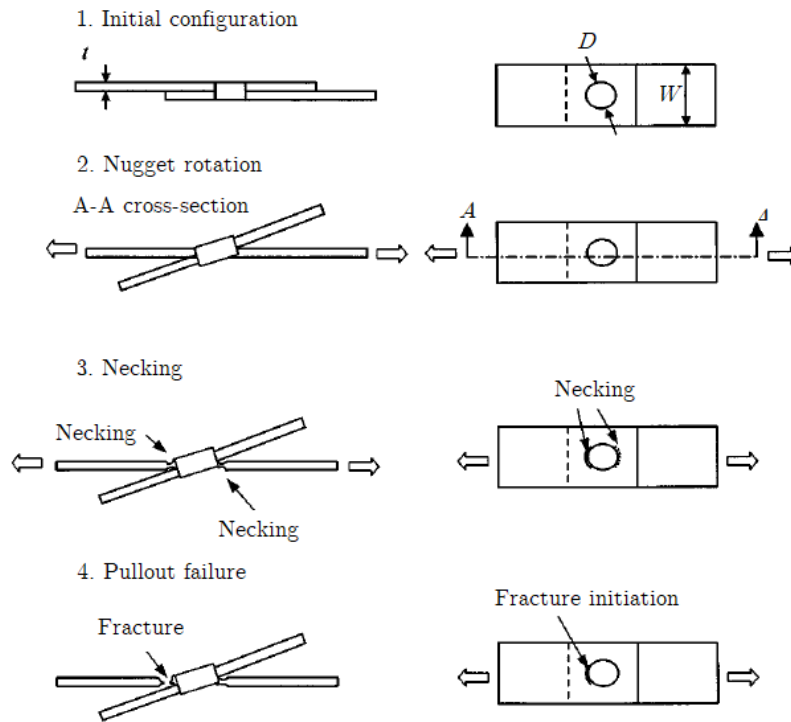


Figure 5.1: Schematic representation of pullout failure [53]

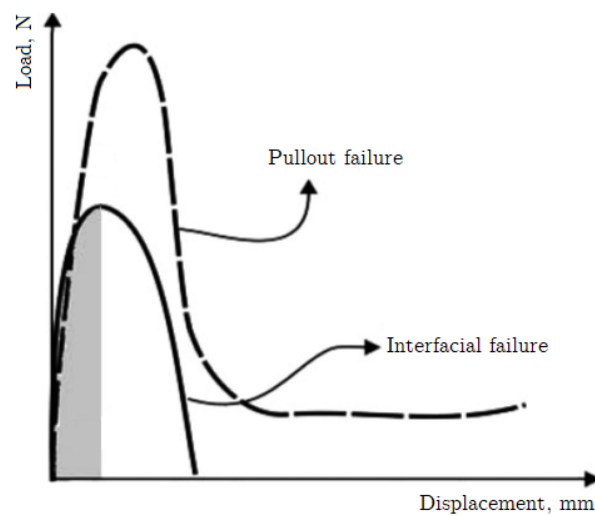


Figure 5.2: Energy absorption during pullout and interfacial failure [54]



## 5.2 Spot weld failure modeling

An increasing body of literature has suggested that due to the material heterogeneity and complex spot weld geometry causing stress concentration, detailed spot weld modeling using solid elements is impractical and time-consuming [62–65]. Therefore, to simplify the spot weld damage modeling, a force-based failure criterion<sup>13</sup>, which captures the behavior of spot-welded joints under general loading conditions, was developed [64, 65]:

$$\left(\frac{f_n}{F_N}\right)^\alpha + \left(\frac{f_s}{F_S}\right)^\beta + \left(\frac{m_b}{M_B}\right)^\gamma + \left(\frac{m_t}{M_T}\right)^\delta = 1, \quad (5.1)$$

where  $F_N$ ,  $F_S$ ,  $M_B$  and  $M_T$  represent the spot weld strength under four distinct loading conditions, whereas  $\alpha$ ,  $\beta$ ,  $\gamma$  and  $\delta$  are parameters defining the failure surface<sup>14</sup>, thus capturing the competition between independent failure modes<sup>15</sup>. Generally, six loading components act on weld nuggets, i.e. three forces and three moments, as shown in Figure 5.3. Normal force  $F_Z$  causes pullout failure, whereas in-plane shear forces  $F_X$  and  $F_Y$  cause rupturing of spot weld under shear loading. Furthermore, out-of-plane moment  $M_Z$  causes torsional failure, while in-plane bending moments  $M_X$  and  $M_Y$  cause bending failure.

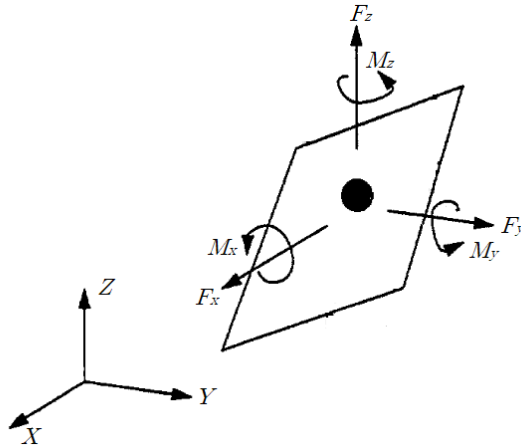


Figure 5.3: Forces acting on weld nugget [65]

In addition, in-plane shear forces are coupled into the resultant shear force  $f_s$ , whereas bending moments are coupled into the resultant bending moment  $m_b$  [64, 65]:

$$f_s = \sqrt{(F_X)^2 + (F_Y)^2}, \quad m_b = \sqrt{(M_X)^2 + (M_Y)^2}. \quad (5.2)$$

<sup>13</sup>The majority of existing finite element software packages are based on the displacement formulation, hence using resultant forces to analyze damage increases accuracy and reduces time of finite element modeling.

<sup>14</sup>Both spot weld strength and parameters defining failure surface are determined experimentally.

<sup>15</sup>Since spot-welded automotive components are seldom subjected to pure tensile, shear, bending and torsion, the coupled force-based criterion is presented to capture the complex behavior of spot-welded joints under general loading conditions and to describe the competition of distinct failure modes.

The left side of the Equation (5.1) provides the value of the spot weld equivalent force under general loading conditions. When the equivalent force exceeds the spot weld strength, damage is initiated. As the loading increases, damage propagates, thus reducing weld stiffness, which eventually results in the complete rupture of the weld nugget.

### 5.3 Quasi-static analysis using *Abaqus/Explicit* [41]

*Abaqus/Explicit* is generally intended to perform high speed dynamic analyses including complex contact formulations and material stiffness degradation due to damage, whereas performing such analyses in *Abaqus/Implicit* usually causes convergence difficulties. Explicit analyses are performed in a large number of small increments utilizing the central-difference time integration scheme to calculate the change of nodal velocities by assuming a constant acceleration during an increment. *Abaqus/Explicit* solves the dynamic equilibrium equation:

$$\mathbf{M} \cdot \ddot{\mathbf{u}} = \mathbf{P} - \mathbf{I}, \quad (5.3)$$

where  $\mathbf{M}$  is the nodal mass matrix,  $\ddot{\mathbf{u}}$  is the vector of nodal acceleration, whereas  $\mathbf{P}$  and  $\mathbf{I}$  are respectively the vector of imposed forces and the vector of internal forces. Nodal accelerations at the beginning of the increment are calculated from Equation (5.3):

$$\ddot{\mathbf{u}}|_{(t)} = \mathbf{M}^{-1}(\mathbf{P} - \mathbf{I})|_{(t)}. \quad (5.4)$$

The next step is the calculation of nodal velocities using the central-difference time integration:

$$\dot{\mathbf{u}}|_{(t+\frac{\Delta t}{2})} = \dot{\mathbf{u}}|_{(t-\frac{\Delta t}{2})} + \frac{\Delta t|_{(t+\Delta t)} + \Delta t|_{(t)}}{2} \cdot \ddot{\mathbf{u}}|_{(t)}. \quad (5.5)$$

Finally, the calculated nodal velocities are integrated to obtain nodal displacements as follows:

$$\mathbf{u}|_{(t+\Delta t)} = \mathbf{u}|_{(t)} + \Delta t|_{(t+\Delta t)} \dot{\mathbf{u}}|_{(t+\frac{\Delta t}{2})}. \quad (5.6)$$

Therefore, output variables at time  $t + \Delta t$  are calculated from the corresponding values at time  $t$ , thus no iterations are required. However, the key to the computational efficiency is the use of diagonal and lumped nodal mass matrix  $\mathbf{M}$ , which results in uncoupled equations of motion. Hence, the explicit procedure does not require the estimation of tangent stiffness, yet the inversion of  $\mathbf{M}$  is trivial, which reduces the cost of the analysis [41, 66].

Since the explicit dynamic procedure integrates nodal accelerations using small increments, the central-difference time integrator is conditionally stable, i.e. an approximate stability limit<sup>16</sup> is calculated using the following equation:

$$\Delta t \approx \frac{L_{min}}{c_d}, \quad (5.7)$$

where  $L_{min}$  represents the smallest element dimension and  $c_d$  represents the dilatational wave speed<sup>17</sup>. Moreover, the time increment used in the procedure has to be smaller than the stability limit, otherwise, the solution becomes unstable, i.e. the response variables tend to oscillate.

Energy balance plays a vital part in the evaluation of a system response obtained using the explicit central-difference integration rule. The total energy of the observed system comprises of several components and should be approximately constant throughout the analysis:

$$E_{Total} = E_I + E_{FD} + E_V + E_K + E_{IH} - E_W - E_{PW} - E_{CW} - E_{MW} - E_{HF}, \quad (5.8)$$

where  $E_I$  is the internal energy,  $E_{FD}$  is the frictional dissipated energy,  $E_V$  is the viscous dissipation energy,  $E_K$  is the kinetic energy and  $E_{IH}$  is the internal heat energy, whereas  $E_W$ ,  $E_{PW}$ ,  $E_{CV}$  and  $E_{MW}$  are respectively the work done by the external applied loads, contact penalties, constraint penalties and added mass. Lastly,  $E_{HF}$  is the energy developing through external fluxes. In addition, the internal energy consists of the following components:

$$E_I = E_E + E_P + E_{CD} + E_A + E_{DMD} + E_{DC} + E_{FC}, \quad (5.9)$$

where  $E_E$  is the elastic strain energy,  $E_P$  is the energy dissipated through inelastic processes,  $E_{CD}$  is the energy dissipated through creep or viscoelasticity,  $E_A$  is the artificial strain energy<sup>18</sup>,  $E_{DMD}$  is energy dissipated through damage, whereas  $E_{FC}$  is the fluid cavity energy.

---

<sup>16</sup>Generally, the stability limit is calculated based on the highest frequency of the observed structure, i.e.  $\Delta t \leq \frac{2}{\omega_{max}}$ . However, the determination of the exact value of the highest frequency is time-consuming. Hence, approximate stability limit is estimated, often not resulting in a conservative value, but simultaneously reducing the analysis time and simplifying the procedure [41].

<sup>17</sup>The dilatational wave speed is the material-dependent variable calculated as  $c_d = \sqrt{\frac{E}{\rho}}$  [41]. Since the stable time increment is estimated based on the dilatational wave speed, the stability limit represents the smallest time required for the dilatational wave to cross any element of the mesh.

<sup>18</sup>The artificial strain energy consists of the energy stored in hourglass resistance and transverse shear in shell and beam elements. Large values of artificial strain energy indicate that mesh refinement should be performed [41].

Moreover, during quasi-static analyses, imposed loading rates are low. Thus, strain rates of observed structures are low and inertial effects can be neglected. Since a quasi-static solution is, by definition, a long-time solution, performing quasi-static analysis in its natural time scale is computationally impractical and time-consuming. Hence, the aim is to artificially accelerate analysis, which results in transformation of the state of static equilibrium into a state of dynamic equilibrium, yet achieving insignificant inertial effects [?, 41, 67–69]. If inertial forces have a significant impact on the system response, the solution tends to localize, resulting in e.g. excessive local plastic deformation. In addition, analysis can be artificially accelerated either by increasing loading rate or by scaling the mass, whereas the quasi-static response is obtained if the ratio of kinetic to internal energy does not exceed 10% throughout the process, which ensures the conservation of energy. Hence, the quasi-static response is ensured if the work done by the external forces is approximately equal to the internal energy of the system, as shown in Figure 5.4.

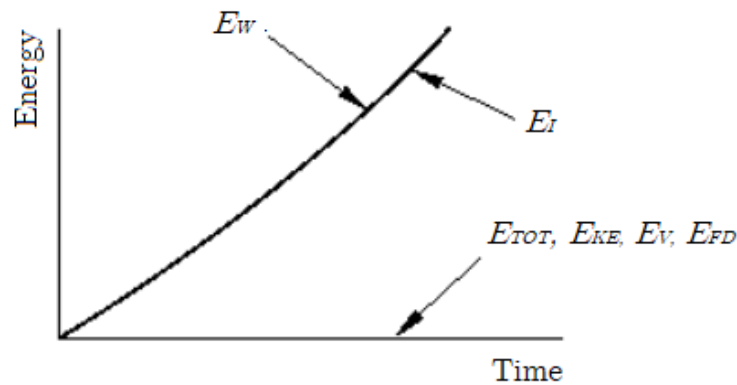


Figure 5.4: Energy balance in quasi-static analysis [41]

Since the dominant response of quasi-static analysis is the first structural mode shape, appropriate loading rates<sup>19</sup> are estimated based on the period of the lowest natural frequency [41, 67–70]. As the loading rate increases, the time required to perform the analysis reduces, however, inertial effects become more dominant. Therefore, the appropriate loading rate should provide an economical solution, simultaneously ensuring the quasi-static response. Moreover, mass scaling enables the reduction of solution time without increasing loading rates in simulations involving e.g. a rate-dependent material. Since the stable time increment is dictated by the smallest element length, the aim of mass scaling is to artificially increase the density of the smallest elements in the mesh to increase the stable time increment. However, excessive mass scaling leads to unstable solutions as well, therefore, it is crucial to determine the appropriate mass scaling factor.

<sup>19</sup>Loading rate is defined as the ratio between the maximum displacement occurring in the analysis and the assumed step time.

## 5.4 Quasi-static damage analysis of spot-welded specimens based on [71]

The coupled-force based damage initiation criterion (Equation 5.1) is verified by performing a displacement-controlled quasi-static damage analysis of standard spot-welded specimens (Figure 5.5) using *Abaqus/Explicit* under the following assumptions:

- Homogeneous material properties,
- General contact between spot-welded sheets,
- Sheet metals are discretized using S4R shell elements,
- Displacement is imposed using smooth step amplitude to reduce noise generated from the initial kinetic energy [41].

The objectives of performed quasi-static analyses are as follows:

1. Verification of the coupled force-based damage initiation criterion (Equation 5.1),
2. Analysis of the effect of different spot weld models.

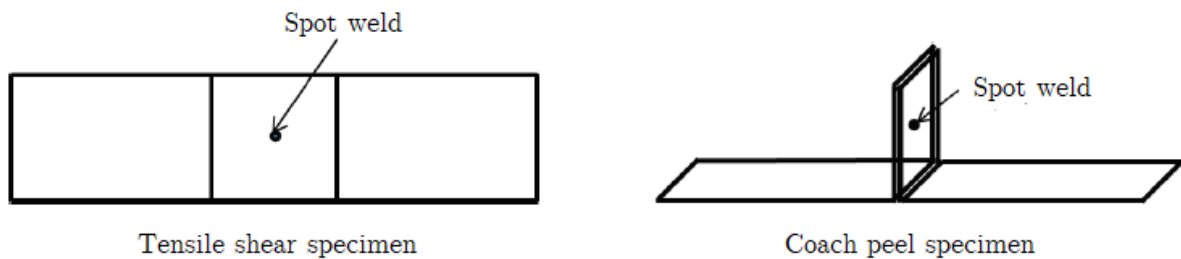


**Figure 5.5: Specimen geometry [71]**

Spot welds are represented using the following structural elements:

1. Connector element (CONN3D2) connected to surrounding shell elements via kinematic coupling,
2. Connector element (CONN3D2) connected to surrounding shell elements via 'spider' of rigid B31 elements,
3. Mesh-independent fastener.

Generally, connector elements provide a functional and versatile way of modeling physical connections using discrete geometry (node-to-node connection), simultaneously describing the kinematic and kinetic complexity of such connections (e.g. spot welds, hinges, rivets etc.) [41]. In comparison with multi-point constraints, connector elements do not eliminate degrees of freedom included in the connection and can be utilized to model both rigid and deformable behavior. Moreover, the available degrees of freedom define the components of relative motion local to the connector element, i.e. the motion and position of the second node is defined relative to the first node of the connector element [41]. In addition, *Abaqus/CAE* offers a wide variety of connector element types to model the complex connector behavior. The available connector element types are categorized into the following classes:

- Basic connections, which affect either translational or rotational components of the second node,
- Assembled connections, which are comprised of the basic connections,
- Complex connections, which affect a combination of DOF at the connector element nodes.

To verify the coupled force-based damage initiation criterion, the weld nugget was modeled using CONN3D2, which is a three-dimensional 2-node element having a total of 12 degrees of freedom. That is to say, each node of the connector element is associated with three displacements and three rotations defined in a local coordinate system of the connector element. The deformable behavior of spot-welded region is described using the assembled connector type *Bushing*, which is composed of two basic connections: *Projection Cartesian*, which allows independent behavior in three local Cartesian directions affecting translational DOF at both connector nodes and *Projection Flexion-Torsion*, which allows different behavior of bending and torsional rotation at both nodes. Moreover, the connector type *Bushing* does not impose constraints on the components of relative motion and can describe general state of deformation. In addition, Figure 5.6 shows the spot weld connector orientation and derived loading components, according to the Equation (5.2).

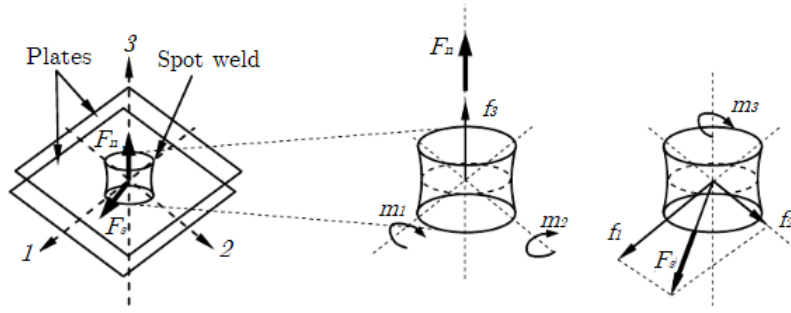


Figure 5.6: Spot weld connection orientation and derived components [72]

In addition, the following material properties are assigned to the connector element representing the weld nugget [71]:

- Uncoupled linear elasticity,
- Coupled plasticity with defined nonlinear isotropic hardening,
- Force-based damage initiation criterion,
- Motion-based damage evolution law.

Moreover, uncoupled linear elasticity is based on Timoshenko's beam theory [71, 73, 74] by assuming the isotropic base material properties and isotropic weld cross-section:

$$\begin{bmatrix} f_1 \\ f_2 \\ f_3 \\ m_1 \\ m_2 \\ m_3 \end{bmatrix} = \begin{bmatrix} \frac{2GS}{L} & 0 & 0 & 0 & 0 & 0 \\ 0 & \frac{2GS}{L} & 0 & 0 & 0 & 0 \\ 0 & 0 & \frac{ES}{L} & 0 & 0 & 0 \\ 0 & 0 & 0 & \frac{EI}{L} & 0 & 0 \\ 0 & 0 & 0 & 0 & \frac{EI}{L} & 0 \\ 0 & 0 & 0 & 0 & 0 & \frac{GJ}{L} \end{bmatrix} \cdot \begin{bmatrix} u_1 \\ u_2 \\ u_3 \\ \theta_1 \\ \theta_2 \\ \theta_3 \end{bmatrix}, \quad (5.10)$$

where  $G$  represent the shear modulus equal to  $G = \frac{E}{2(1+\nu)}$ ,  $S$  and  $L$  are the cross-section and the length of the spot weld, whereas  $I$  and  $J$  are respectively the area moment of inertia and polar moment of inertia. The plastic behavior of connector element is formulated in terms of the equivalent force  $\bar{F}$  and the equivalent plastic displacement  $\bar{u}_{pl}$ , instead of stress and equivalent plastic strain [41, 71, 73]. The connector equivalent force is estimated as follows:

$$\bar{F} = \left[ \left( \frac{F_N}{R_N} \right)^\beta + \left( \frac{F_S}{R_S} \right)^\beta + \left( \frac{M_T}{R_T} \right)^\beta + \left( \frac{M_B}{R_B} \right)^\beta \right]^{\frac{1}{\beta}}, \quad (5.11)$$

where  $F_N$  is the connector normal force,  $F_S$  and  $M_B$  are respectively the shear and the bending derived loading components (Equation 5.2), whereas  $M_T$  is the torsional loading.

Moreover, parameters  $R_N$ ,  $R_S$ ,  $R_T$ , and  $R_B$  are experimentally defined coupling coefficients, which describe the relative contribution of connector derived loading components to the connector force [71]. Moreover, the connector yield function is defined by the following equation:

$$\phi(\bar{F}, \bar{u}_{pl}) = \bar{F} - F_H \leq 0, \quad (5.12)$$

where  $F_H$  represent the isotropic hardening function, i.e. the force or moment that causes yielding. When  $\phi=0$ , the local plastic deformation is initiated, thus the associated plastic flow rule is assumed [41]:

$$\dot{u}_{pl} = \dot{\bar{u}}_{pl} \frac{\delta \Phi}{\delta \bar{F}}, \quad (5.13)$$

where  $\dot{u}_{pl}$  is the rate of plastic relative motion, whereas  $\dot{\bar{u}}_{pl}$  is the rate of equivalent plastic relative motion [41]. In addition, the isotropic hardening<sup>20</sup> describing the size change of the yield surface is formulated as a function of the equivalent plastic relative motion [41, 71, 73]:

$$F_H = F_0 + Q(1 - e^{-b\bar{u}_{pl}}), \quad (5.14)$$

where  $Q$  and  $b$  are material-dependent parameters defining respectively the maximum change of the yield surface size and the rate of change of the yield surface size as the plastic flow progresses. If the connector equivalent force defining the yield surface size remains constant, the hardening does not occur. Furthermore, the stiffness degradation due to the damage initiation is defined using the coupled force-based damage initiation criterion (Equation 5.1). Generally, if the forces transferred through the connector element representing the weld nugget exceed critical values, the damage is initiated, resulting in the stiffness degradation and eventually leading to the complete failure [41]:

$$F_i = (1 - d_i)F_{eff_i}, \quad 0 \leq d_i \leq 1, \quad (5.15)$$

where  $d_i$  represents the overall damage variable, whereas  $F_{eff_i}$  is the response of the component of the relative motion  $i$  if damage were not present [41], as shown in Figure 5.7.

---

<sup>20</sup>The presented nonlinear hardening function is described using an isotropic exponential Voce hardening law, which adds exponential saturation hardening term to the linear component.



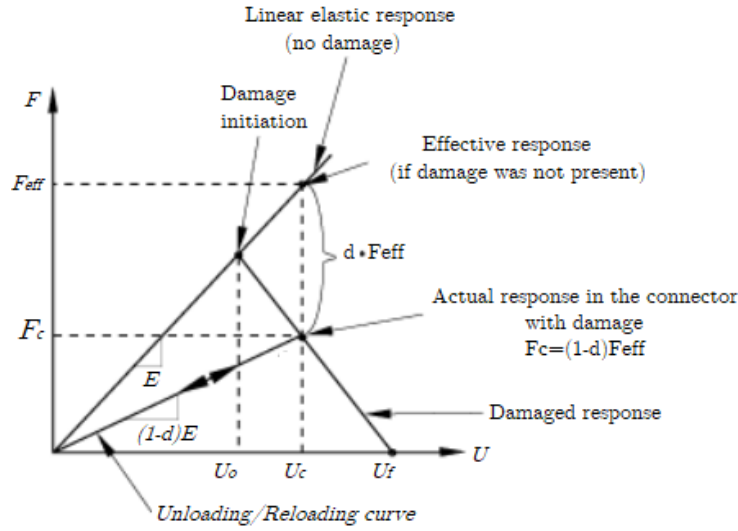


Figure 5.7: Schematic representation of stiffness degradation upon damage initiation [41]

Prior to damage initiation, the overall damage variable  $d_i$  is equal to 0, hence the connector element force response remains intact. However, upon damage initiation, the stiffness of the connector element is progressively degraded, until  $d_i$  reaches the value of 1, which results in the complete failure.

Moreover, by introducing Equation (5.11) into Equation (5.1), the coupled-force based damage initiation criterion is defined as follows:

$$\left(\frac{F_N}{F_{iN}}\right)^\beta + \left(\frac{F_S}{F_{iS}}\right)^\beta + \left(\frac{M_B}{M_{iB}}\right)^\beta + \left(\frac{M_T}{M_{iT}}\right)^\beta \leq 1, \quad (5.16)$$

where  $F_{iN} = R_N \cdot F_N$ ,  $F_{iS} = R_S \cdot F_S$ ,  $M_{iB} = R_B \cdot M_B$  and  $M_{iT} = R_T \cdot M_T$  [71]. In addition, the connector damage evolution is specified as a linear motion-based damage evolution law [41]:

$$d = \begin{cases} 0, & \text{if } \bar{U} \leq U_i, \\ \frac{\bar{U} - U_i}{U_f - U_i}, & \text{if } U_i \leq \bar{U} \leq U_f, \end{cases} \quad (5.17)$$

where  $\bar{U}$  and  $U_i$  represent respectively the equivalent motion and the equivalent motion at damage initiation, whereas  $U_f$  represents the motion at the ultimate failure. The equivalent motion  $\bar{U}$  is estimated using the following equation:

$$\bar{U} = \left[ \left(\frac{U_N}{k_N}\right)^\beta + \left(\frac{U_S}{k_S}\right)^\beta + \left(\frac{\theta_T}{k_T}\right)^\beta + \left(\frac{\theta_B}{k_B}\right)^\beta \right]^{\frac{1}{\beta}}, \quad (5.18)$$

where  $k_N$ ,  $k_S$ ,  $k_B$  and  $k_T$  represent experimentally determined coupling coefficients,  $U_N$  is the normal displacement and  $\theta_T$  is the torsional rotation.

Furthermore, in Equation (5.18)  $U_B$  and  $\theta_T$  represent the shear and torsional derived components of the relative motion:

$$U_S = \sqrt{u_1^2 + u_2^2}, \quad \theta_B = \sqrt{\theta_1^2 + \theta_2^2}. \quad (5.19)$$

When the damage variable  $d_i$  reaches 1, the equivalent motion  $\bar{U}$  is equal to the motion at ultimate failure  $U_f$ . Hence, spot weld ruptures and losses its load carrying capability.

The above presented equations describe the complex spot weld behavior, yet connector elements are easy to implement and greatly simplify the analysis. However, there is a total of 20 different parameters required to define the deformable connector behavior. The determination of parameters describing the connector behavior requires experimental testing, thus there is a focus to additionally simplify connector element definition, at the same time obtaining sufficiently accurate results.

Moreover, mesh-independent fasteners use connector elements to define discrete, point-to-point connections and to model the complex nature of spot-welded connections. Therefore, fasteners are composed of CONN3D2 elements connected to the surrounding mesh via distributing coupling<sup>21</sup>, i.e. each fastening point is associated with a group of nodes of the surrounding elements in a region named radius of influence [41]. Since the fastening points are connected to the adjacent mesh via distributing coupling, the fastener location is independent of the position of nodes on the connected surfaces. In addition, the typical fastener configuration is presented in Figure 5.8.

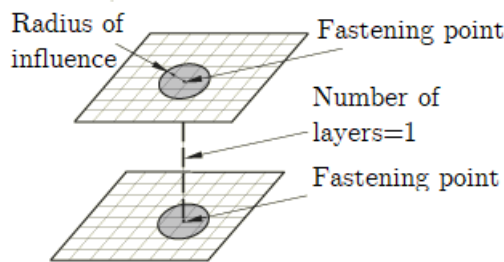


**Figure 5.8: Fastener definition [41]**

Structural elements representing the weld nugget are shown in Figure 5.9, whereas Figure 5.10 presents numerical models of the standard spot-welded specimens used to verify the coupled force-based failure criterion.

<sup>21</sup>Distributing coupling constraints the motion of the coupling nodes to the motion of the reference node in a weighted sense. Thus, it is implemented in the fastener definition to monotonically decrease the contribution of nodes in the region of influence to the motion of fastening points as the distance from the fastening points increases [41].

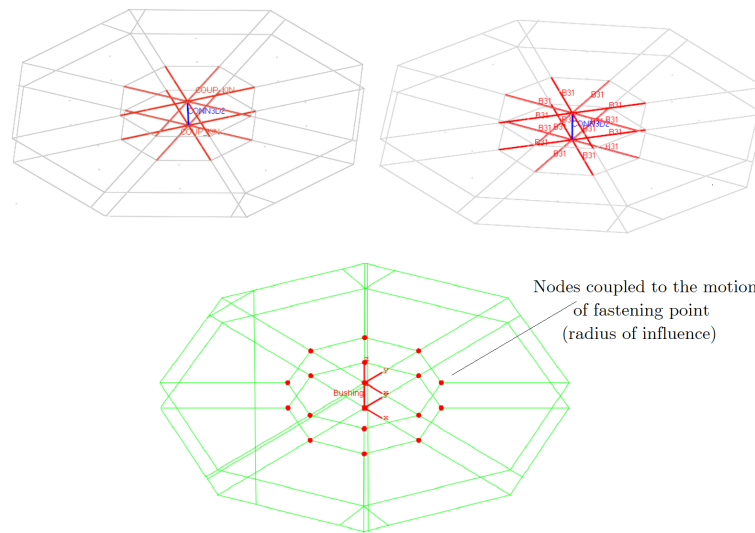


Figure 5.9: Structural elements representing spot weld nugget

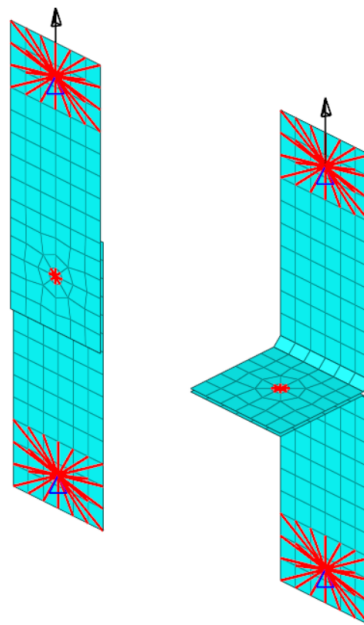
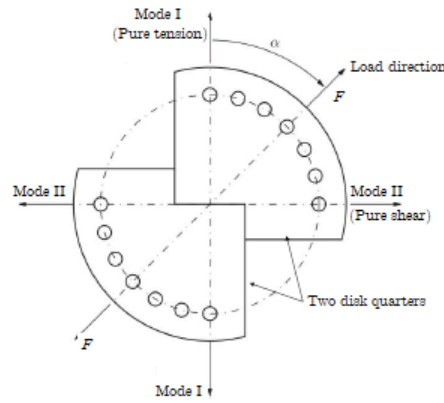


Figure 5.10: Numerical model of tensile shear and coach peel specimens used for quasi-static damage analysis

#### 5.4.1 Determination of parameters defining connector element behavior [71]

The experimental data provided in [71] is used to define the connector element behavior and thus verify the coupled force-based damage initiation criterion. The material parameters defining the spot weld damage behavior under pure and combined tensile shear loads were determined using Arcan clamping device (Figure 5.11), which limits the deformation of the base material around the nugget circumference and enables the characterization of the weld nugget non-linear behavior.



**Figure 5.11: Arcan clamping device [71]**

According to [71] and [73], the determination of the spot weld strength using the standard spot-welded specimens is characterized by the contribution of the plates to the global response. Hence, the spot weld strengths of independent failure modes do not correspond to the actual values. However, Arcan clamping device reduces the contribution of the plates around the weld nugget to the overall response and provides the possibility of mixed-mode loading. The experimental results obtained with Arcan clamping device are presented in Figure 5.12.

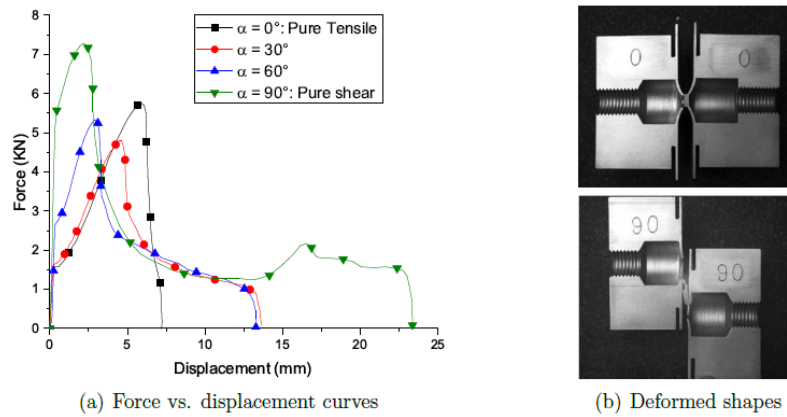


**Figure 5.12: Experimental results obtained with Arcan clamping device [71]**

The experimental results presented above lead to the conclusion that the pure shear loading requires the highest failure initiation force. Thus, the connector equivalent force and the equivalent relative motion are normalized with respect to the shear loading direction [71]:

$$R_S = 1, \quad k_S = 1, \quad (5.20)$$

whereas  $R_N$  is defined as the ratio of the peak normal force to the peak shear force:

$$R_N = \frac{F_{maxN}}{F_{maxS}}. \quad (5.21)$$

Since the experimental testing of spot-welded specimens using Arcan clamping device does not produce bending nor torsional moments, coupling coefficients  $R_B$  and  $R_T$  are assumed as follows [71]:

$$R_B = R_S \cdot r, \quad R_T = R_N \cdot r, \quad (5.22)$$

where  $r$  is the radius of the spot weld nugget.

Furthermore, the following assumptions are included in the process of material parameters identification [71]:

- The initial yield force  $F_0$  (Equation 5.14) corresponds to the yield force obtained by performing the pure shear Arcan experiment,
- The failure initiation force  $F_i$  corresponds to the peak force of the pure shear Arcan experiment,
- Parameter  $\beta$  defining the failure surface is determined using the experimental peak forces obtained by performing the pure and mixed-mode loading Arcan tests. Thus,  $\beta$  is equal to 1.2.

The initial yield force could as well be determined based on the base material properties [71]:

$$F_0 = \sigma_0 \cdot S, \quad (5.23)$$

where  $S$  represents the weld nugget cross-section area, whereas the saturation  $Q$  is determined as the difference between the ultimate tensile stress and the yield stress multiplied by the weld nugget cross-section area [71]:

$$Q = (\sigma_{UTS} - \sigma_Y) \cdot S. \quad (5.24)$$

The remainder of the parameters defining the connector behavior is determined experimentally and performing subsequent optimization of a cost function, which measures the difference between the experimentally and numerically obtained force vs. displacement curve (elaborated in more detail in [71]). In addition, the base material properties are listed in Table 5.1.

**Table 5.1: Properties of base material following Ludwik's hardening law [71]**

$E$ , GPa	$\sigma_Y$ , MPa	$\sigma_{UTS}$ , MPa	$K$ , MPa	$n$
210	171	301.6	409.6	0.447

## 5.5 Numerical results

Figure 5.13 schematically displays the finite element verification procedure of the coupled force-based failure initiation criterion. The aim of the procedure is to artificially increase the loading rate simultaneously obtaining the quasi-static response. Since the dominant response of the quasi-static analysis is the first structural mode shape, the appropriate loading rate was determined based on the period of the first natural frequency. According to [41], the quasi-static response is ensured if the selected analysis duration is at least 3 to 5 times higher than the period of the first eigenfrequency.

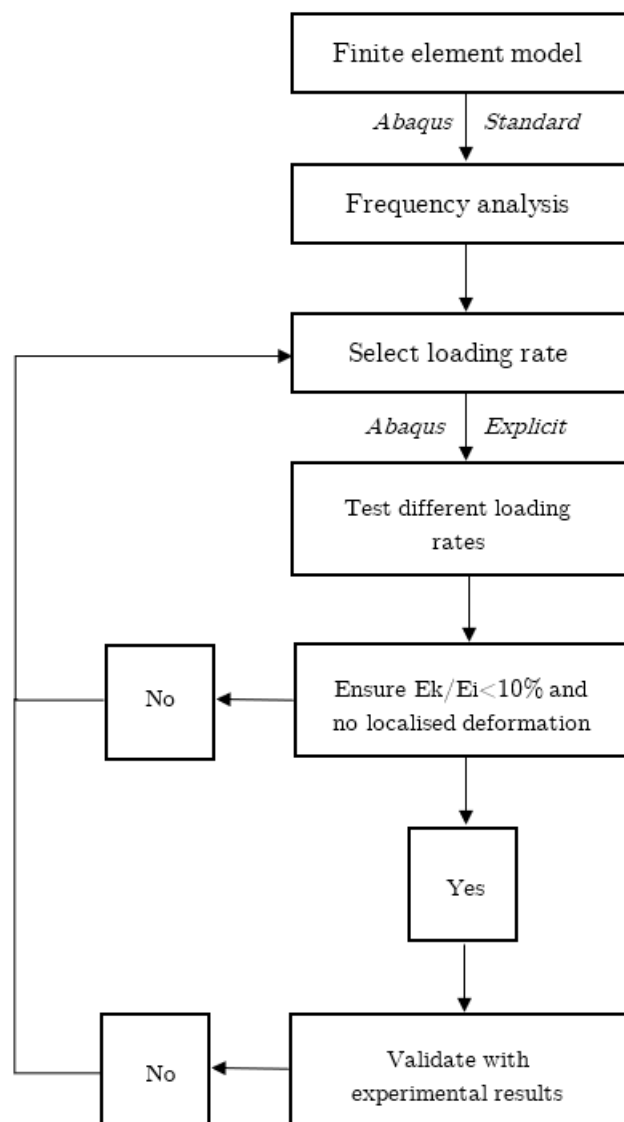


Figure 5.13: Schematic representation of an algorithm to define appropriate loading rate, which ensures the quasi-static response

### 5.5.1 Tensile shear specimen

Figure 5.14 shows the finite element meshes used to evaluate the effect of mesh size on the first eigenfrequency of tensile shear specimen. The approximate size of shell elements is respectively 8 mm, 6 mm, 4 mm and 2 mm.

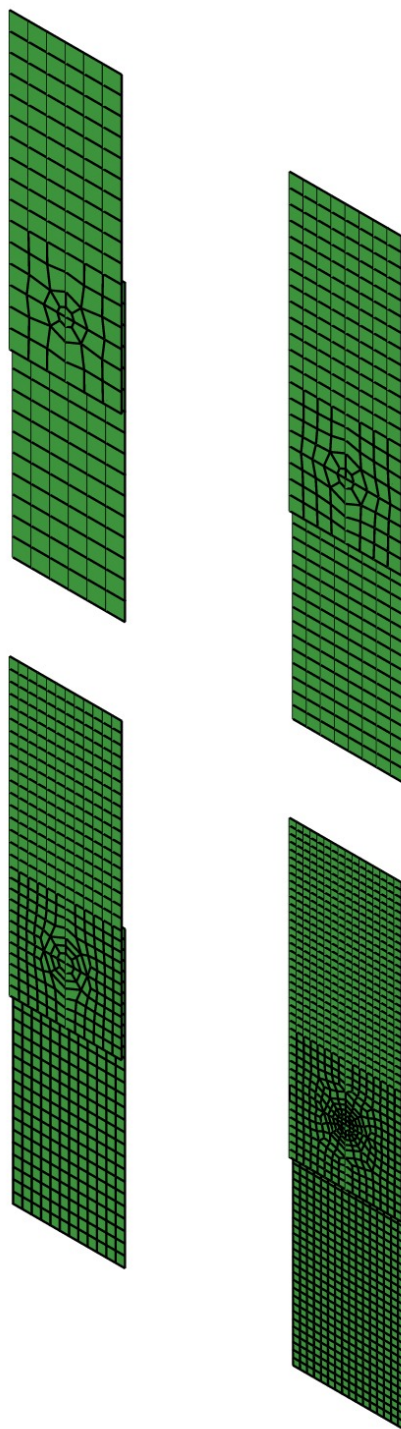
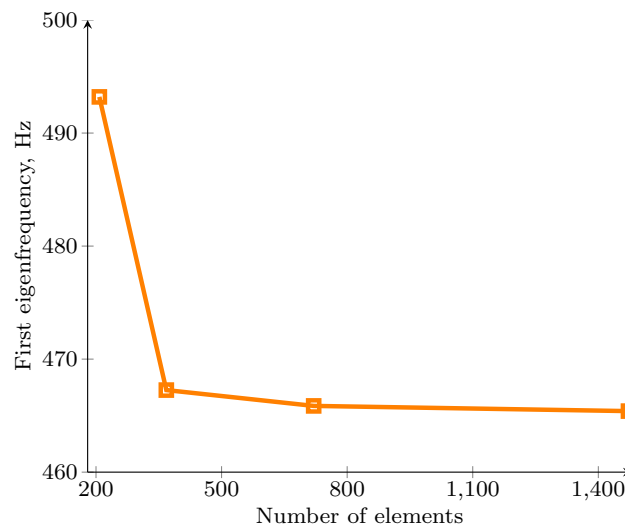


Figure 5.14: Tensile shear specimen discretized with S4R element of different size

The values of the first eigenfrequency with respect to the number of shell elements are listed in Table 5.2. Additionally, Figure 5.15 graphically displays the convergence of the first natural frequency.

**Table 5.2: The change in the first eigenfrequency of tensile shear specimen**

Number of S4R	$f_1$ , Hz
208	493.2
368	467.2
720	465.8
1472	465.4



**Figure 5.15: First eigenfrequency vs. number of S4R elements**

Given the results above, it is concluded that the shell element size has no significant influence on the first eigenfrequency of tensile shear specimen. Thus, for the subsequent verification of the coupled force-based damage initiation criterion, the shell element mesh with 368 elements is used based on the following conclusions:

- The value of the first eigenfrequency does not change significantly with the increase of the number of S4R elements from 368 to 1472,
- Since the stability limit of the explicit procedure is calculated based on the smallest element of the mesh, finite element models with 720 and 1472 would require a large number of increments to perform the analysis. Therefore, the numerical model consisting of 368 S4R elements is used to achieve an economical solution.



Moreover, the following figures display the energy distribution for different loading rates.

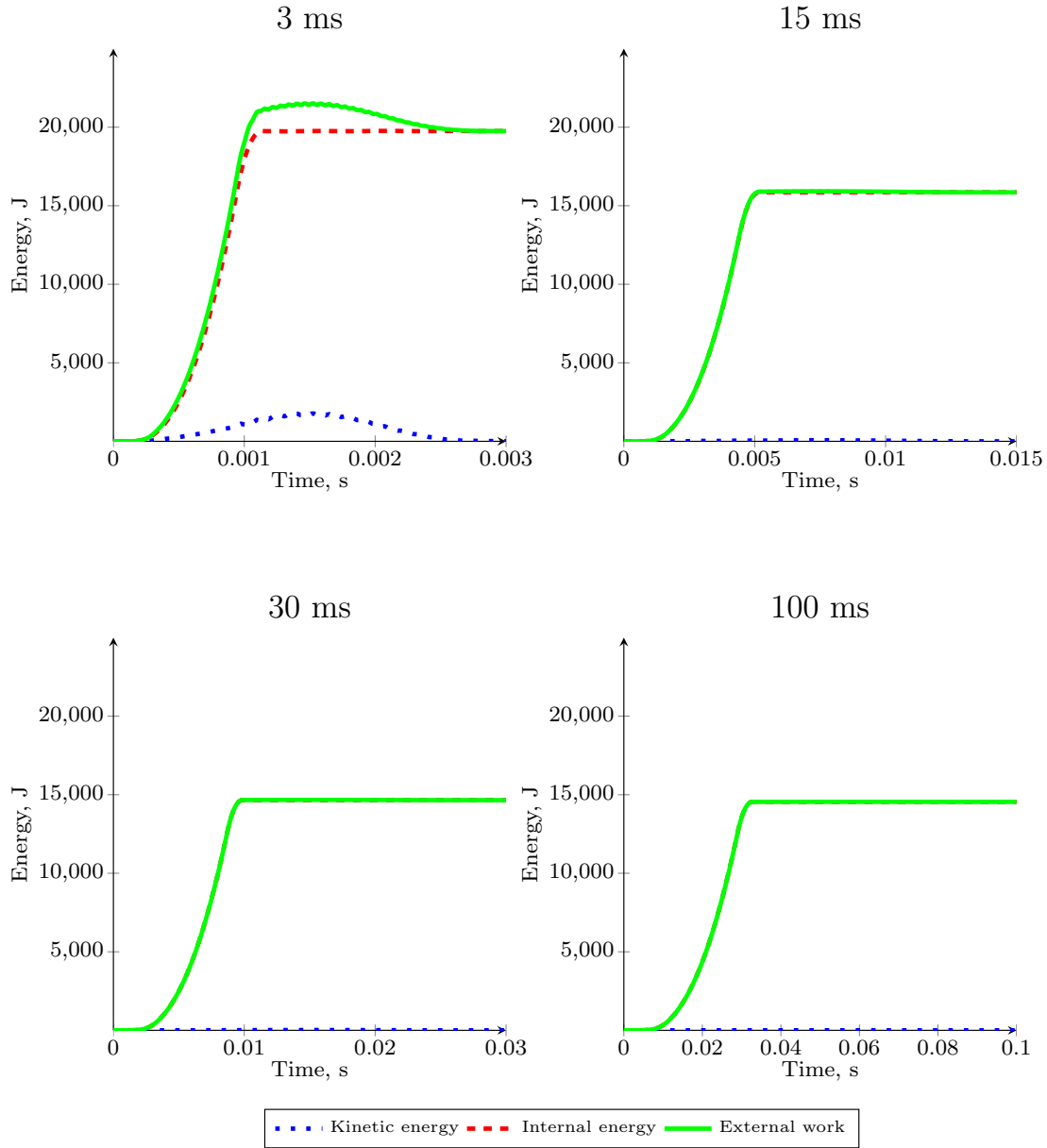


**Figure 5.16: Energy distribution during the analysis of tensile shear specimen**

Since the period of the first eigenfrequency is equal to 0.002 s, first the analysis duration time of 0.003 s was evaluated. As evident, the energy conservation criterion (Equation 5.8) is not satisfied. Thus, the obtained response is not quasi-static due to the significant inertial effects. Therefore, the loading rate was gradually reduced and it was observed that the quasi-static response is ensured if the duration time is at least 3 times higher than the period of the first eigenfrequency. According to [41], even though the kinetic energy is small compared to the internal energy, if the kinetic energy contains large oscillations, the analysis model could experience significant plastic deformation. Therefore, a secondary evaluation criterion in addition to  $(E_k/E_i) \cdot 100 < 10\%$  is introduced to validate the obtained response. The secondary criterion includes the evaluation of the stress distribution and the equivalent

plastic deformation around the nugget circumference at the moment prior to the failure initiation, as shown in Figure 5.17 and Figure 5.18.

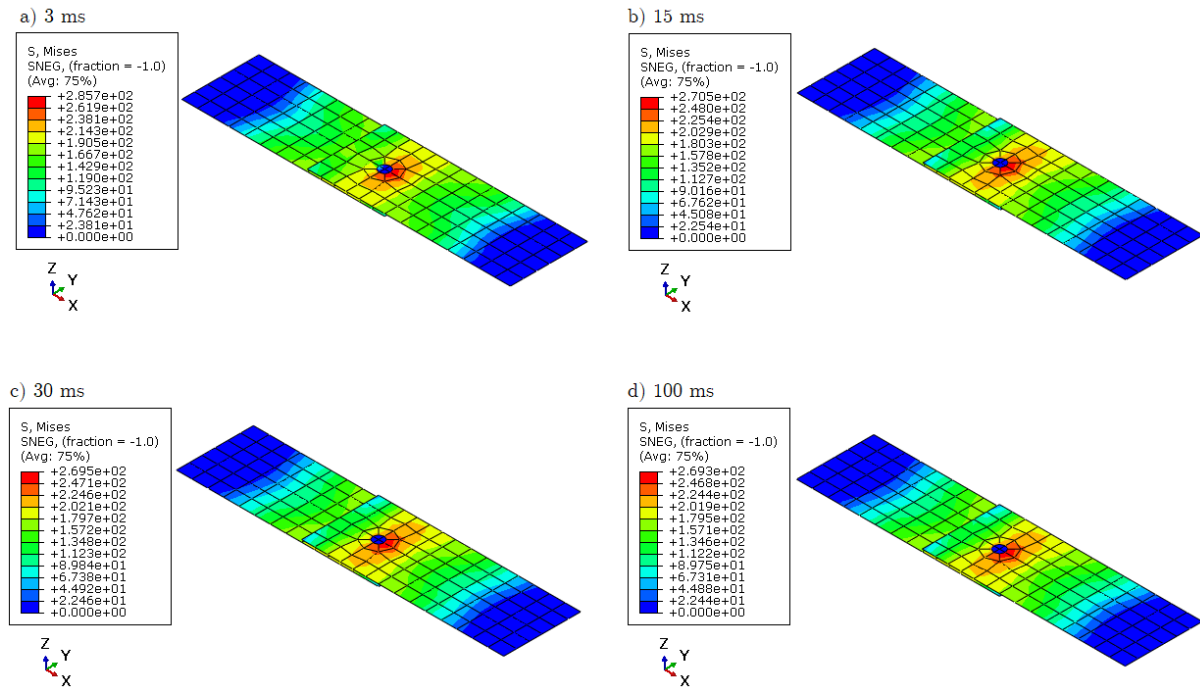


Figure 5.17: Stress distribution around the nugget circumference

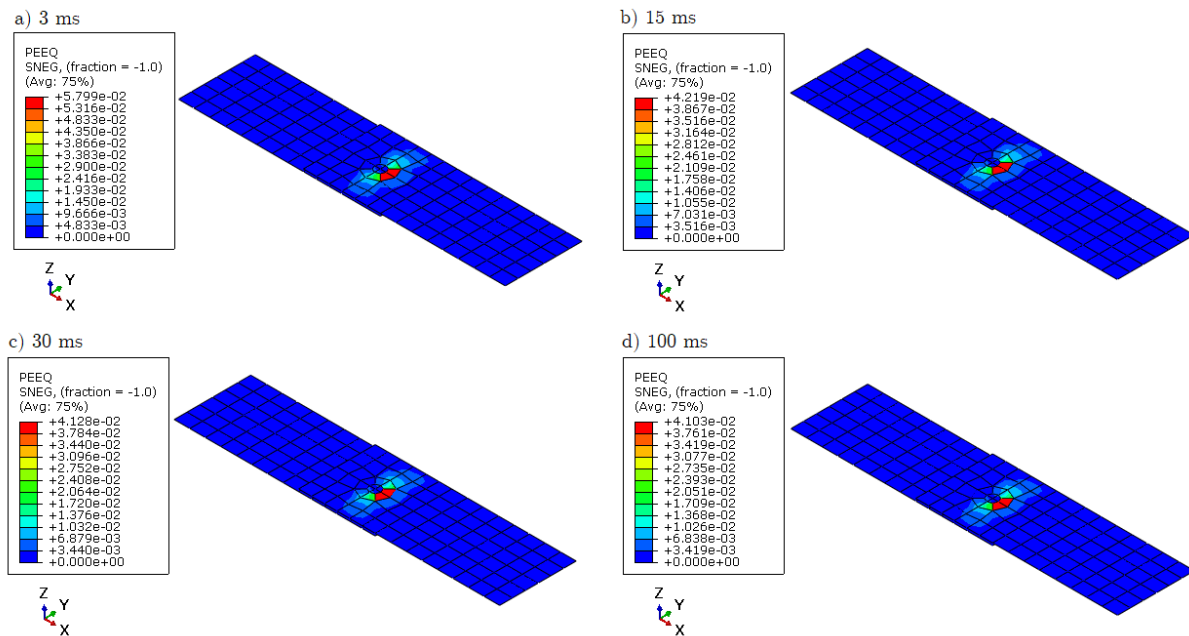


Figure 5.18: Equivalent plastic deformation around the nugget circumference

The results presented above lead to the conclusion that as the loading rate increases, the ratio of kinetic to internal energy increases, which influences the stress distribution and the amount of plastic deformation around the nugget circumference. Thus, the subsequent analyses are performed with the step time equal to 0.1 s. Furthermore, Figure 5.19 show the reaction

force with respect to the displacement at tension node obtained using different structural elements to couple the weld nugget to the surrounding shell element mesh. Additionally, the comparison of the failure initiation force and the displacement at failure initiation with the experimental data is presented in Table 5.3.

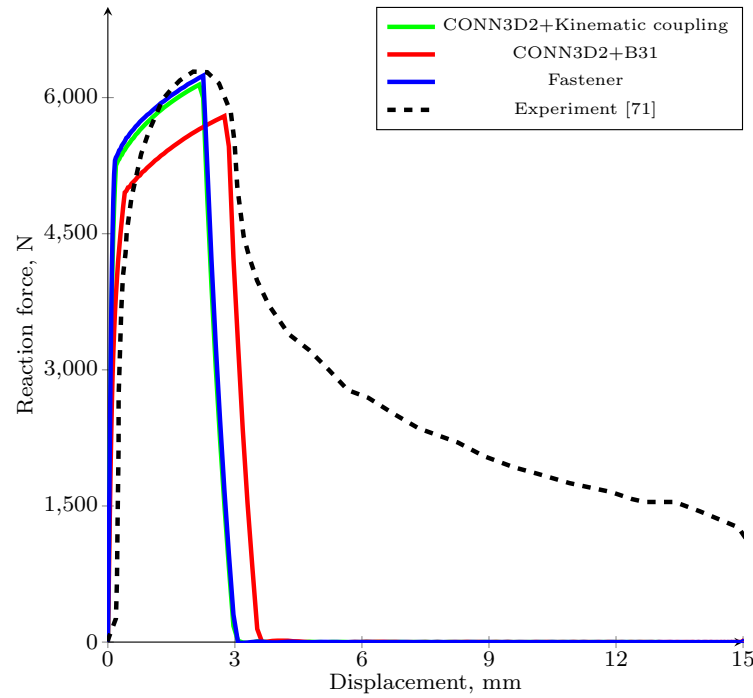


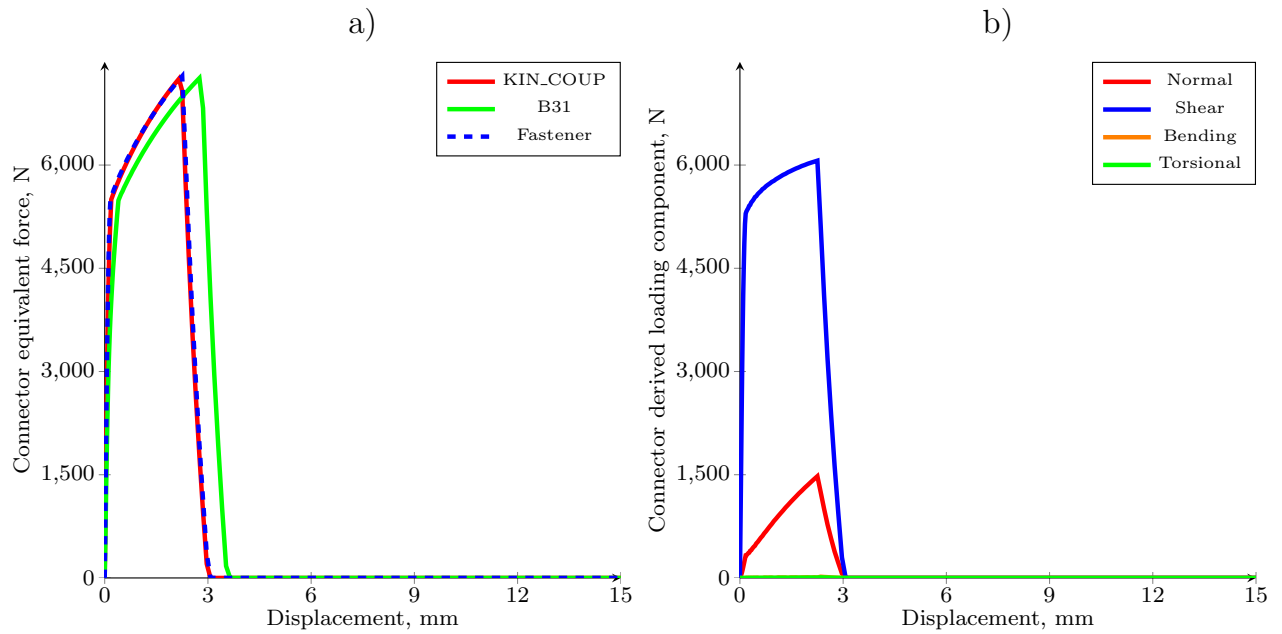
Figure 5.19: Reaction force vs. displacement at tension node

Table 5.3: Comparison of numerical results with experimental data [71]

Model	$F_i^{FEM}$ , N	$F_i^{Exp}$ , N	$E_{rel}$
CONN3D2+KIN_COUP	6142.23	6286	-2.3%
CONN3D2+B31	5796.21	6286	-7.8%
Fastener	6241.72	6286	-0.7%
Model	$U_i^{FEM}$ , m	$U_i^{Exp}$ , mm	$E_{rel}$
CONN3D2+KIN_COUP	2.157	2.015	7.04%
CONN3D2+B31	2.75	2.015	36.47%
Fastener	2.25	2.015	11.66%

The results presented above lead to the conclusion that the mesh-independent fastener and the connector element in combination with kinematic coupling yield sufficiently accurate prediction of the failure initiation force ( $E_{rel} < 10\%$ ). Although the displacement at the failure initiation is overestimated, the relative difference between the displacement at the failure initiation obtained using the connector element in combination with kinematic coupling is within the acceptable range ( $E_{rel} < 10\%$ ). However, the displacement at the failure initiation obtained using the mesh-independent fastener exceeds the acceptable limit

( $E_{\text{rel}} > 10\%$ ). Moreover, the connector element in combination with the 'spider' of beam elements yields sufficiently accurate prediction of the failure initiation force, whereas the displacement at the failure initiation is significantly overestimated. Furthermore, Figure 5.20 a) shows the connector equivalent force (Equation 5.11) with respect to the displacement at tension node obtained using different structural elements to couple the connector element to surrounding shell mesh. In addition, Figure 5.20 b) displays the connector derived loading components (Equation 5.2) obtained using kinematic coupling to connect the connector element to adjacent shell element mesh.



**Figure 5.20: a) Connector equivalent force, b) Connector derived loading components**

Based on the results presented in Figure 5.20, it is observed that in the case of tensile shear specimen, the torsional and bending loading components make no significant contribution to the connector equivalent force. Therefore, the coupled force-based damage initiation criterion can be expressed in terms of the normal and shear loading:

$$\bar{F} = \left[ \left( \frac{F_N}{R_N} \right)^\beta + \left( \frac{F_S}{R_S} \right)^\beta \right]^{\frac{1}{\beta}}. \quad (5.25)$$

In addition, Figure 5.21 a) presents the connector equivalent force obtained using mesh-independent fastener in combination with the modified failure initiation criterion (Equation 5.25), whereas Figure 5.21 b) display the connector derived loading components (Equation 5.2) with respect to the displacement at the tension node.

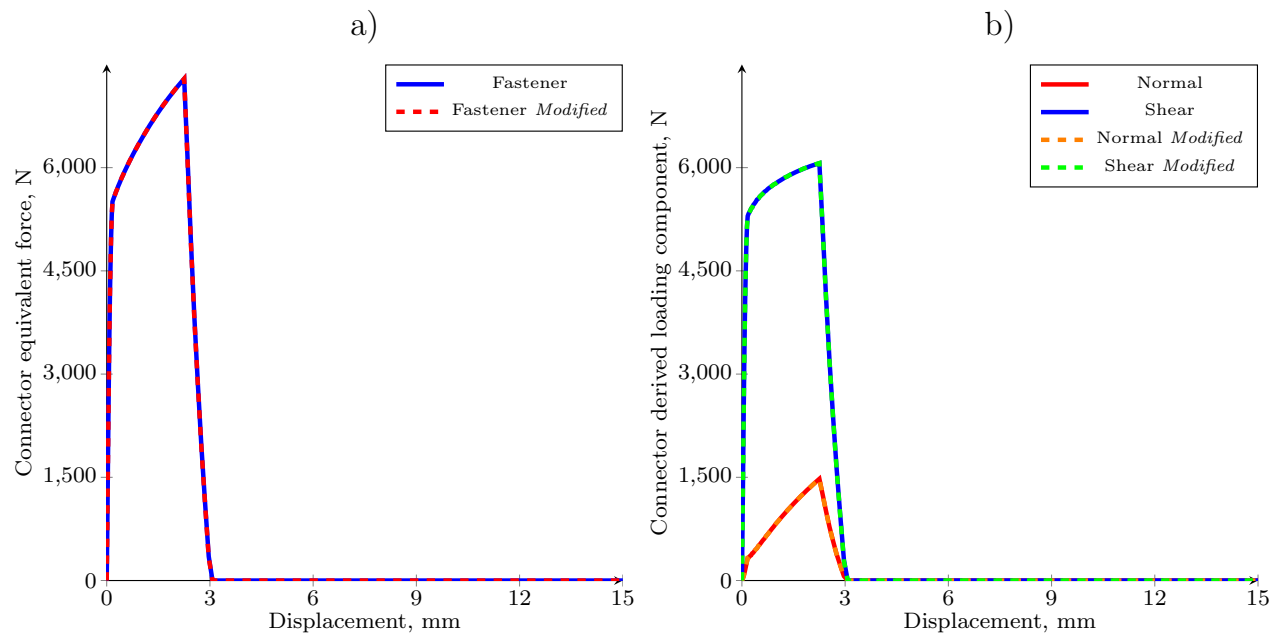


**Figure 5.21: a) Connector equivalent force, b) Connector derived loading component**

Furthermore, Figure 22. displays the reaction force at tension node with respect to the global displacement obtained using mesh-independent fastener in combination with the modified failure initiation criterion (Equation 5.25). In addition, Table 5.4 presents the comparison of obtained results with the experimental data.

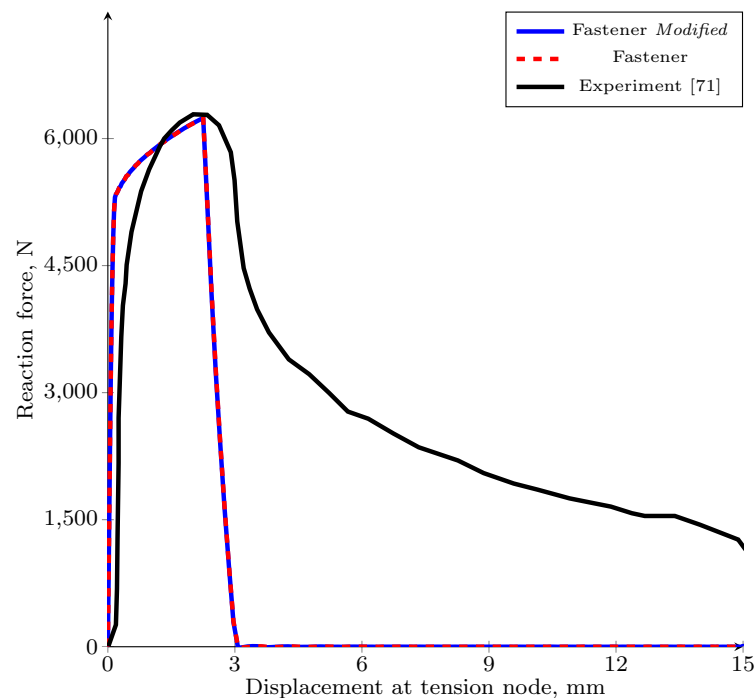


**Figure 5.22: Reaction force vs. displacement at tension node**

**Table 5.4: Comparison between numerical and experimental data [71] for the modified failure initiation criterion**

Model	$F_i^{FEM}$ , N	$F_i^{Exp}$ , N	$E_{rel}$
Fastener	6241.72	6286	-0.7%
Fastener <i>Modified</i>	6243.36	6286	-0.67%
Model	$U_i^{FEM}$ , m	$U_i^{Exp}$ , mm	$E_{rel}$
Fastener	2.25	2.015	10.44%
Fastener <i>Modified</i>	2.25	2.015	10.44%

As evident, the modified failure initiation criterion yields a minor improvement in the prediction of the failure initiation force, whereas the displacement at the failure initiation is overestimated. However, it is important to emphasize that the modified force-based damage initiation criterion simplifies the analysis.

To summarize, from the previously presented results the following key findings emerge:

- The quasi-static response can be ensured based on the period of the first eigenfrequency. That is to say, the quasi-static response is generally obtained if the selected analysis duration is at least 3 to 5 times higher than the period of the first natural frequency, which ensures the conservation of energy. However, although the conservation of energy is ensured, the analysis models could experience significant plastic deformation. Therefore, a secondary evaluation criterion, which validates the stress and equivalent plastic strain distribution around the nugget circumference, is introduced.
- All three spot weld models yield sufficiently accurate prediction of the failure initiation force ( $E_{rel} < 10\%$ ). The displacement at the failure initiation obtained using the connector element in combination with kinematic coupling is within the acceptable range ( $E_{rel} < 10\%$ ). However, both the mesh-independent fastener and the connector element in combination with the 'spider' of beam elements significantly overestimate the displacement at the failure initiation ( $E_{rel} > 10\%$ ).
- In the case of tensile shear specimen, the torsional and bending loading components make no significant contribution to the connector equivalent force. Therefore, the coupled force-based damage initiation criterion can be expressed in terms of the normal and shear loading components. The modified failure initiation criterion simplifies the analysis, simultaneously yielding sufficiently accurate prediction of the failure initiation force, whereas the displacement at the failure initiation is overestimated.

### 5.5.2 Coach peel specimen

Figure 5.23 shows finite element meshes used to evaluate the effect of mesh size on the first eigenfrequency of coach peel specimen. The approximate size of the shell elements is respectively 7 mm, 6 mm, 4 mm and 3 mm.

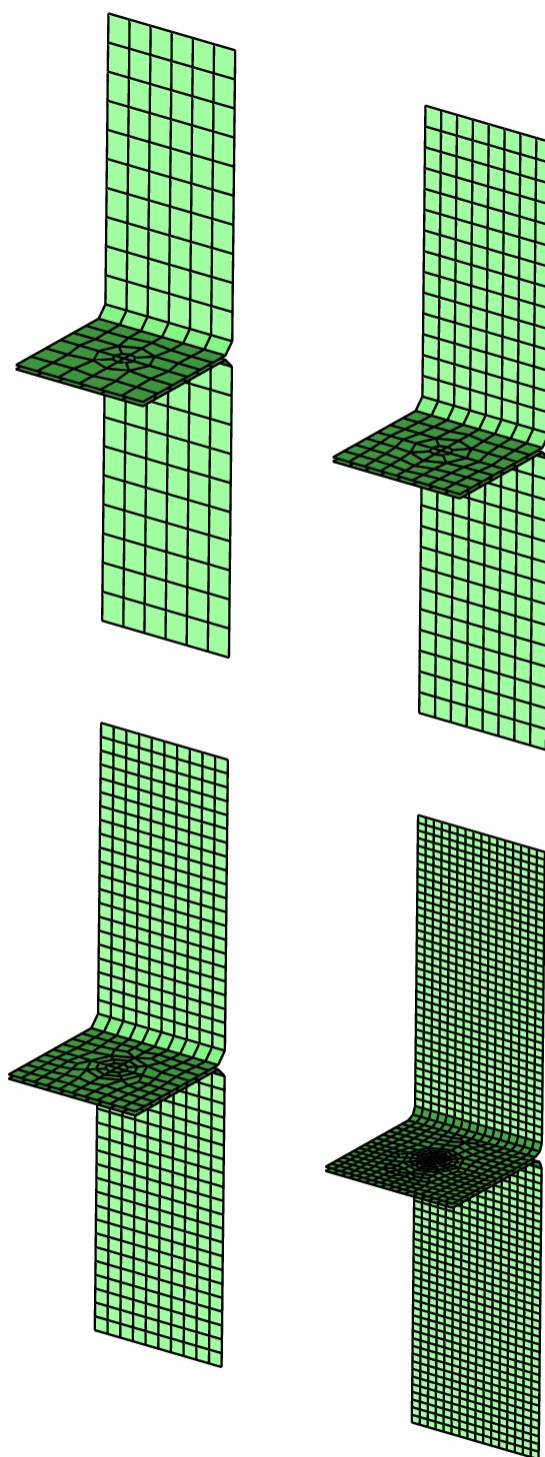
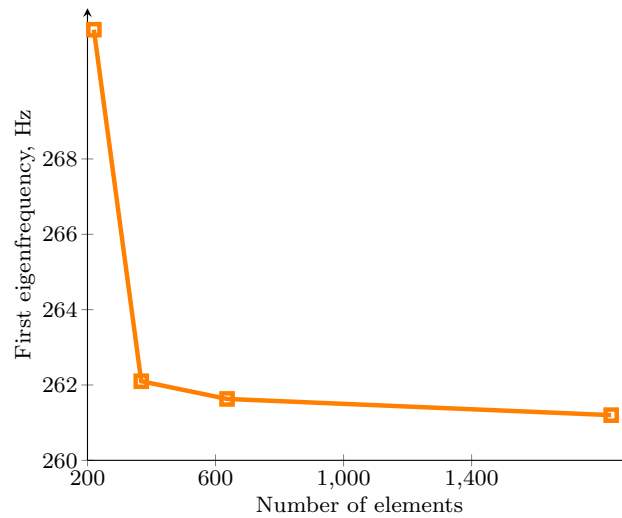


Figure 5.23: Coach peel specimen discretized with S4R element of different size

The values of the first eigenfrequency with respect to the number of shell elements are listed in Table 5.5. In addition, Figure 5.24 graphically displays the convergence of the first natural frequency.

**Table 5.5: The change in the first eigenfrequency of coach peel specimen**

Number of S4R	$f_1$ , Hz
220	271.43
368	262.1
636	261.63
1836	261.2



**Figure 5.24: First eigenfrequency vs. number of S4R elements**

From the previously presented results, it is concluded that the shell element size has no significant influence on the first eigenfrequency of coach peel specimen. Therefore, for the subsequent verification of the coupled force-based damage initiation criterion, the shell element mesh with 220 elements is used based on the following conclusions:

- The value of the first eigenfrequency does not change significantly with the increase of S4R elements from 368 to 1472,
- Since the stability limit of the explicit procedure is calculated based on the smallest element of the mesh, finite element models with 636 and 1836 would require a large number of increments to perform the analysis. Thus, the numerical model consisting of 368 S4R elements is used to obtain an economical solution.



Moreover, the following figures display the energy distribution for different loading rates.

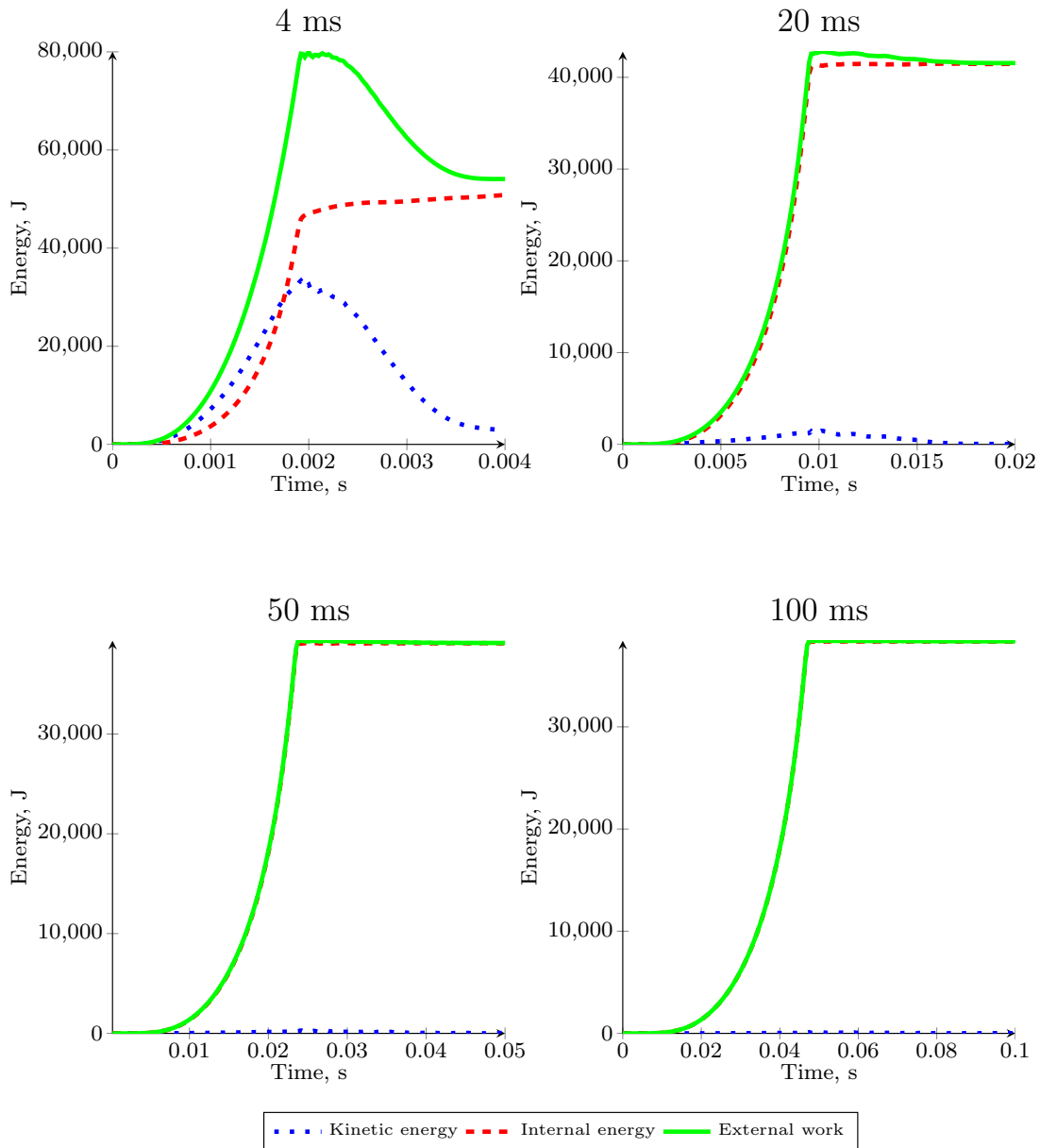


**Figure 5.25: Energy distribution during analysis of coach peel specimen**

Since the period of the first eigenfrequency is equal to 0.003 s, first the analysis duration time of 0.004 s was evaluated. As evident, the energy conservation criterion (Equation 5.8) is not satisfied. Thus, the obtained response is not quasi-static due to the significant inertial effects. Therefore, the loading rate was gradually reduced and it was observed that the quasi-static response is ensured if the duration time is at least 3 times higher than the period of the first eigenfrequency. Furthermore, the stress distribution and the equivalent plastic deformation around the nugget circumference at the moment prior to the failure initiation are evaluated, as shown in the following figures.

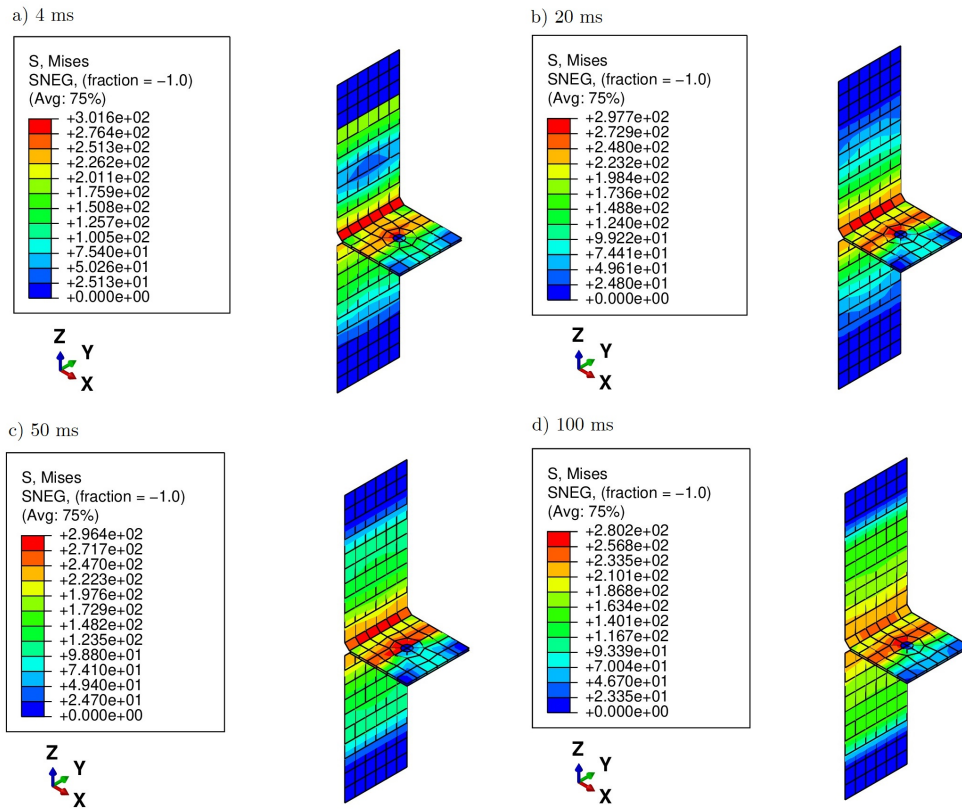


Figure 5.26: Stress distribution around the nugget circumference

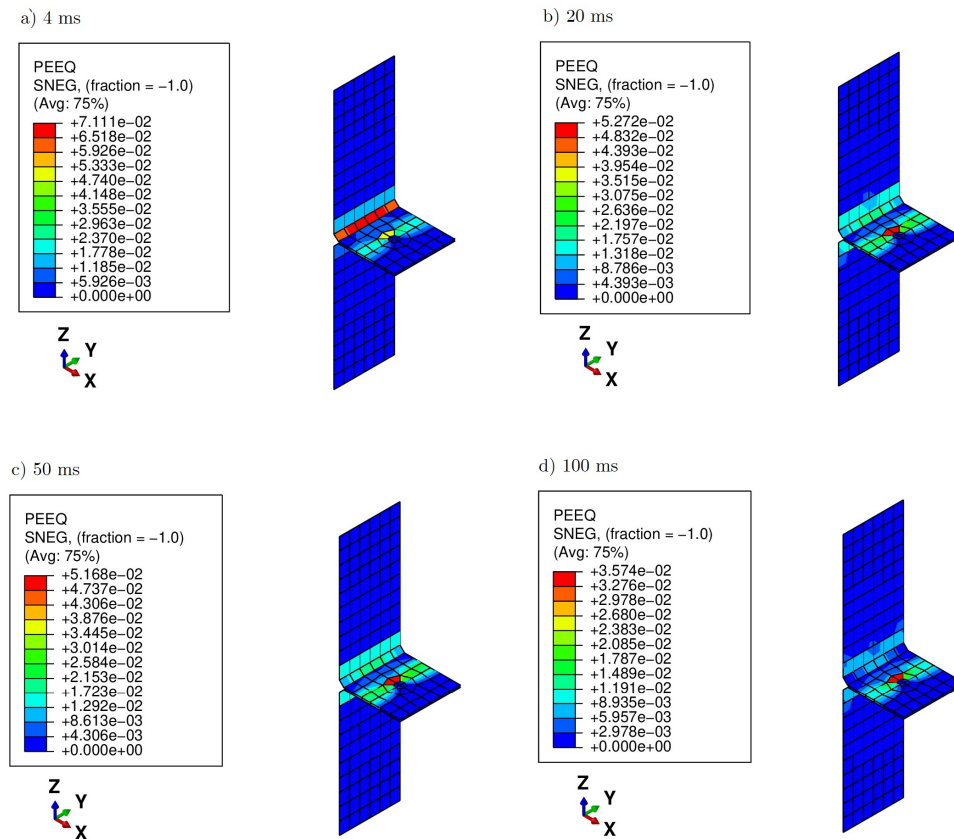


Figure 5.27: Equivalent plastic deformation around the nugget circumference

The results presented above lead to the conclusion that as the loading rate increases, the ratio of the kinetic to internal energy increases, which influences the stress distribution and the amount of plastic deformation around the nugget circumference. Therefore, subsequent analyses were performed with the step time equal to 0.1 s. In addition, Figure 5.28 display the reaction force with respect to the displacement at the tension node obtained using different structural elements to couple the connector element to surrounding shell mesh. In addition, the comparison of the failure initiation force and the displacement at failure initiation with the experimental data is presented in Table 5.6.

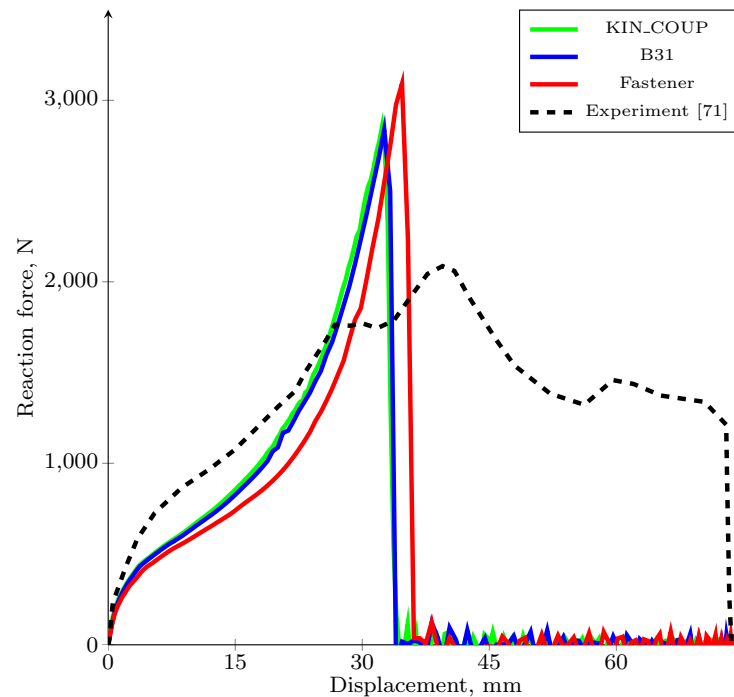


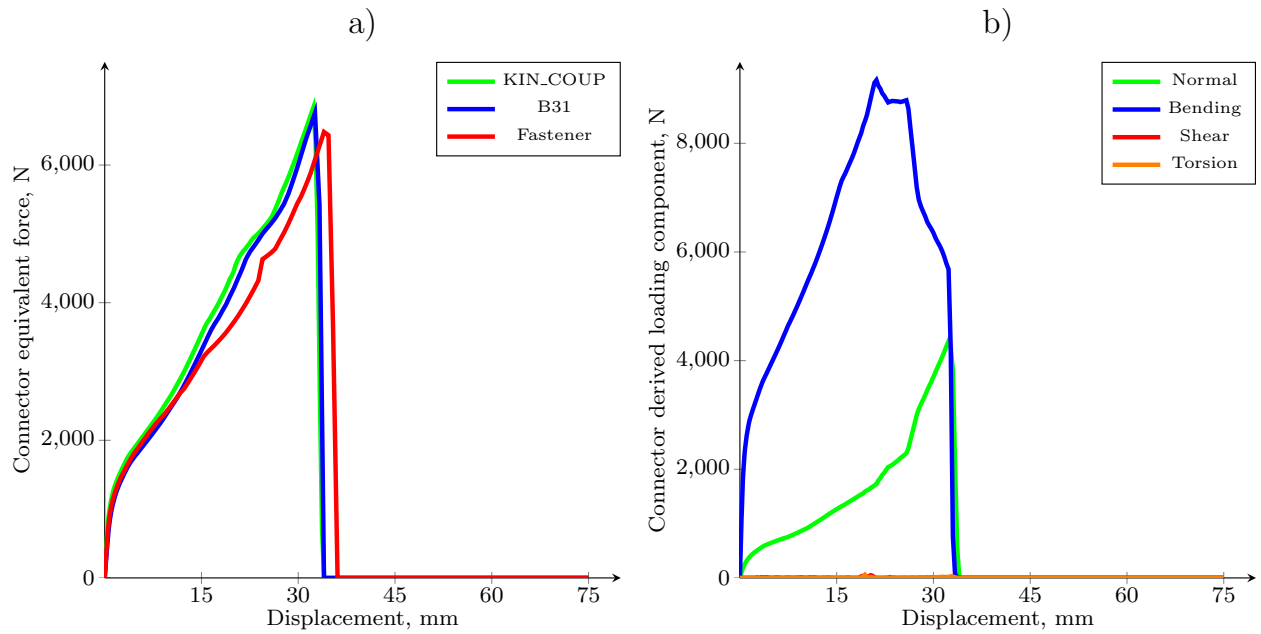
Figure 5.28: Reaction force vs. displacement at tension node

Table 5.6: Comparison of numerical results with experimental data [71]

Model	$F_i^{FEM}$ , N	$F_i^{Exp}$ , N	$E_{rel}$
CONN3D2+KIN.COUP	2855	1744	38.9%
CONN3D2+B31	2837	1744	38.5%
Fastener	3090.76	1766	42.86%
Model	$U_i^{FEM}$ , m	$U_i^{Exp}$ , mm	$E_{rel}$
CONN3D2+KIN.COUP	32.3437	31.8	1.7%
CONN3D2+B31	32.59	31.8	2.4%
Fastener	34.69	31.8	8.3%

As evident, the peak force causing damage initiation obtained using all three spot weld models is significantly overestimated, i.e the predicted failure initiation force values exceed the acceptable limit ( $E_{rel} > 10\%$ ). However, in the case of coach peel specimen, the

displacement at failure initiation obtained using all three spot weld models is within the acceptable range ( $E_{rel} < 10\%$ ). Furthermore, Figure 5.29 a) displays the connector equivalent force (Equation 5.11) with respect to the displacement at tension node obtained using different structural elements to couple the connector element to the adjacent shell mesh. In addition, the connector derived loading components (Equation 5.2) obtained using kinematic coupling to connect the connector element to the surrounding shell mesh are presented in Figure 5.29 b).



**Figure 5.29: a) Connector equivalent force, b) Connector derived loading component**

As evident, in the case of coach peel specimen, the torsional and shear loading component make no significant contribution to the connector equivalent force. Therefore, the coupled force-based damage initiation criterion can be expressed in terms of the normal and bending loading:

$$\bar{F} = \left[ \left( \frac{F_N}{R_N} \right)^\beta + \left( \frac{M_B}{R_B} \right)^\beta \right]^{\frac{1}{\beta}}. \quad (5.26)$$

Moreover, Figure 5.30 a) shows the connector equivalent force obtained using the connector element coupled to surrounding shell mesh via kinematic coupling in combination with the modified failure initiation criterion (Equation 5.26). In addition, Figure 5.30 b) displays the normal and bending loading components with respect to the displacement at tension node.

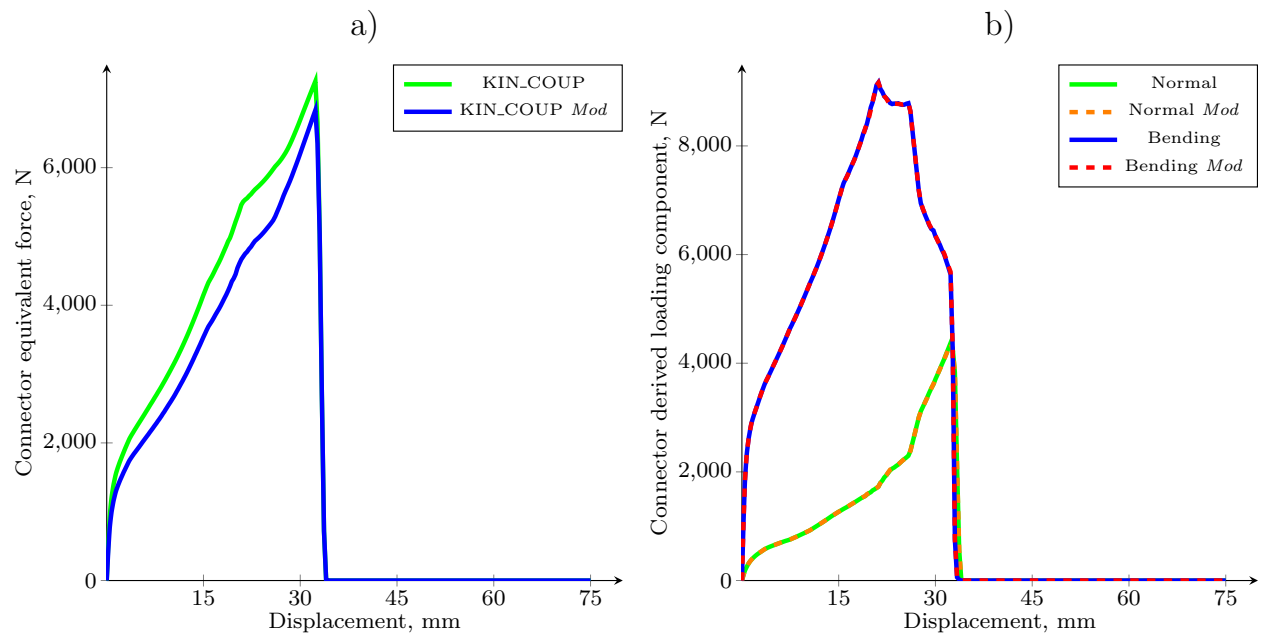


Figure 5.30: a) Connector equivalent force, b) Connector derived loading component

Furthermore, Figure 5.31 displays the reaction force at tension node with respect to the global displacement, whereas the comparison between the numerical results and experimental data is presented in Table 5.7

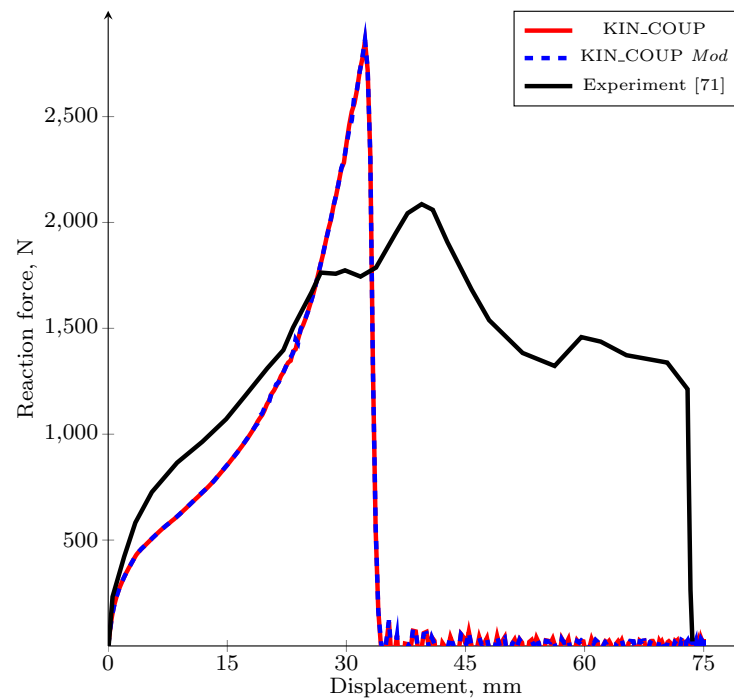


Figure 5.31: Reaction force vs. displacement at tension node

**Table 5.7: Comparison of numerical results with experimental data [71]**

Model	$F_i^{FEM}$ , N	$F_i^{Exp}$ , N	$E_{rel}$
CONN3D2+KIN_COUP	2855	1766	38.14%
CONN3D2+KIN_COUP <i>Mod</i>	2852.17	1766	38.08%
Model	$U_i^{FEM}$ , m	$U_i^{Exp}$ , mm	$E_{rel}$
CONN3D2+KIN_COUP	34.69	31.8	8.33%
CONN3D2+KIN_COUP <i>Mod</i>	34.36	31.8	7.45%

As evident, the modified damage initiation criterion yields a minor improvement in the prediction of the damage initiation force, whereas the predicted displacement at the failure initiation is within the acceptable range ( $E_{rel} < 10\%$ ). However, it is important to emphasize that the modified force-based damage initiation criterion simplifies the analysis.

Moreover, it is important to emphasize that the previously presented results are obtained with the spot weld stiffness values calculated according to Equation 5.10. However, if the axial and shear stiffness optimized according to [71] are employed in the connector behavior definition, the estimated value of damage initiation force is significantly altered. The aim of the optimization process was to minimize the cost function which measures the difference between numerically and experimentally obtained results. Both the axial and shear stiffness values were optimized to achieve better correlation with the pure shear and pure tensile Arcan experimental testing [71]. Moreover, the subsequent analysis is performed under the following assumptions:

- The damage behavior is described with the coupled force-based damage initiation criterion according to Equation 5.11,
- The value of connector element shear and axial stiffness is optimized according to [71], while the remainder of stiffness values to describe the uncoupled elastic behavior is calculated according to Equation 5.10,
- The spot weld nugget is represented using mesh-independent fastener.

In addition, Figure 5.32. presents the reaction force with respect to the displacement at tension node, whereas the comparison of the experimental data with the results obtained using optimized stiffness values is presented in Table 5.8.

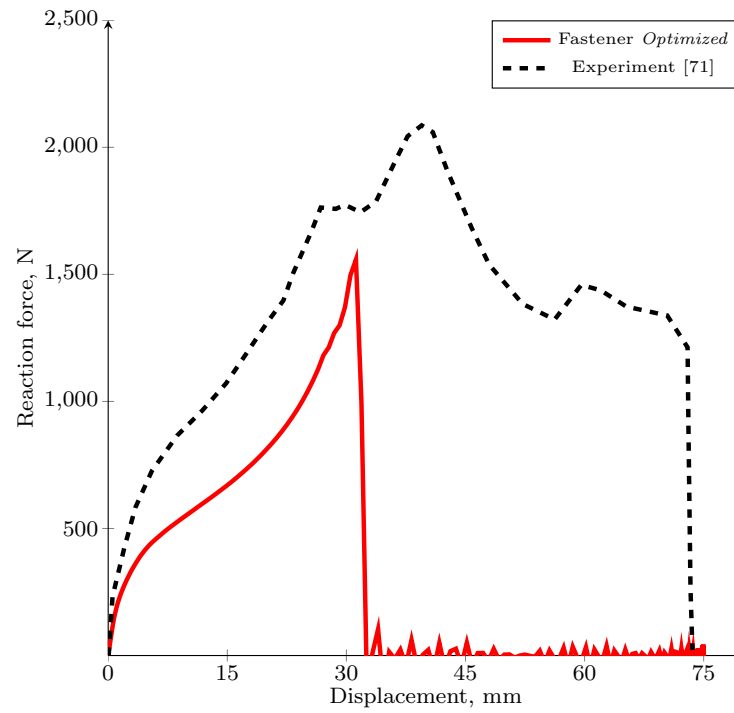


Figure 5.32: Reaction force vs. displacement at tension node

Table 5.8: Comparison between numerical results obtained using optimized spot weld stiffness and experimental data [71]

Model	$F_i^{FEM}$ , N	$F_i^{Exp}$ , N	$E_{rel}$
Fastener	3090.76	1766	42.86%
Fastener <i>Opt</i>	1558.3	1766	-11.7%
Model	$U_i^{FEM}$ , m	$U_i^{Exp}$ , mm	$E_{rel}$
Fastener	34.69	31.8	8.3%
Fastener <i>Opt</i>	31.2	31.8	1.8%

As evident, the damage initiation force is underestimated and the relative difference exceeds the acceptable limit ( $E_{rel} > 10\%$ ). However, the optimized values of axial and shear stiffness yield significant improvement in the predicted value of the displacement at damage initiation. To summarize, the previously presented results lead to the following conclusions:

- In the case of coach peel specimen, numerically determined values of the failure initiation force are overestimated, although the displacement at failure initiation is estimated accurately. Due to the specimen geometry which tends to excessively deform, the experimental results are characterized by the contribution of plates to the global response. That is to say, due to the excessive deformation of sheet metals an additional amount of energy is dissipated during coach peel testing, as shown in Figure 5.31. Therefore, connector parameters defined using Arcan experimental testing yield the upper limit of the failure initiation force.

- In the case of coach peel specimen, both the torsional and shear loading components make no significant contribution to the connector equivalent force. Therefore, the coupled force-based damage initiation criterion can be expressed in terms of the normal and bending connector derived loading components. In addition, the modified failure initiation criterion simplifies the analysis, simultaneously yielding sufficiently accurate prediction of the displacement at damage initiation, whereas the damage initiation force is significantly overestimated.
- If the axial and shear stiffness optimized according to [70] are employed in the connector behavior definition, the estimated value of damage initiation force is significantly altered. That is to say, the damage initiation force is significantly lower, but it exceeds the acceptable limit ( $E_{\text{rel}} > 10\%$ ). However, the relative difference between experimentally and numerically obtained value of the displacement at damage initiation is further reduced.



# 6 | Conclusions

## 6.1 Summary and main conclusions

The four main objectives of the conducted research are identified as follows:

- I. To define a procedure for the fatigue life assessment of spot welded components under constant amplitude loading using fatigue solvers *nCode DesignLife* and *FEMFAT Spot*,
- II. To investigate the effect of geometric properties on the fatigue life of spot-welded specimens,
- III. To define a procedure for the fatigue life assessments of spot-welded structures subjected to random excitation,
- IV. To verify the coupled force-based damage initiation criterion.

### 6.1.1 Findings related to research objectives I and II

The results of performed fatigue analyses of spot-welded specimens under constant amplitude loading lead to the following conclusions:

- Both the Rupp/LBF method and the force-based approach implemented in *FEMFAT Spot* greatly simplify the analysis, simultaneously capturing complex stress state around the nugget perimeter under general loading conditions.
- The Rupp/LBF method implemented in *nCode DesignLife* is insensitive to mesh alignment, mesh refinement and the spot weld model representation.
- Due to the fixed ratio of the outer diameter of the circular plate  $D$  and the nugget diameter  $d$ , *nCode DesignLife* yields rather conservative results, i.e. the structural stresses are overestimated. Hence, *nCode DesignLife* gives the lower limit of the predicted fatigue life.

- The force-based method implemented in *FEMFAT Spot* is insensitive to mesh refinement and mesh alignment. However, the fatigue life of spot-welded specimens exhibits a greater sensitivity to spot weld finite element representation compared to *nCode DesignLife*.
- The stress-based approach implemented in *FEMFAT Spot* is greatly influenced by the shell element size. That is to say, the decrease of shell element size leads to the increase of von Mises stress and thus the decrease of the number of cycles to failure.
- The fatigue life prediction of spot-welded specimens using both force-based and stress-based approach implemented *FEMFAT Spot* greatly depends upon the base material strength. *FEMFAT Spot* modifies the endurance limit of the master spot  $S - N$  curve for the force-based analysis and 7 different  $S - N$  curves employed in the stress-based analysis, although the effect of base material should be originally neglected. That is to say, the increase of the base material strength leads to the increase of the endurance limit of the aforementioned spot  $S - N$  curves. Hence, both the stress-based method and the force-based approach implemented in *FEMFAT Spot* provide the upper limit of fatigue life assessment.
- Since the weld nugget and sheet thickness impact the stress distribution around the nugget circumference, the performed fatigue analysis with *nCode DesignLife* indicates that the aforementioned geometrical factors significantly influence the fatigue life of spot-welded specimens. That is to say, both the increase of the nugget diameter and the sheet thickness result in the decrease of structural stresses around the nugget periphery, which enhances the durability of spot-welded specimens.

### 6.1.2 Findings related to the research objective III

The research conducted in the third chapter leads to the following conclusions:

- The random vibration fatigue analysis of spot-welded structures using *nCode DesignLife* is performed utilizing the Rupp/LBF method to calculate the local response stress PSD. Based on the input PSD, transfer functions and nodal forces and moments extracted from the preliminary linear steady-state dynamic analysis, *nCode DesignLife* estimates the PSD of structural stress response around the nugget circumference both in the weld nugget and the spot-welded sheets. Moreover, Lalanne, Dirlik, NarrowBand and Steinberg probability methods are implemented in

*nCode DesignLife* to calculate the probability density function of the stress range. The PDF of the stress range enables the estimation of the damage accumulated during the analysis duration.

- The results obtained with the Steinberg's approach are the most conservative.
- The results obtained by performing the random vibration fatigue analysis of presented model using *nCode DesignLife* indicate that the *Z*-axis response is characterized by the highest accumulated damage. In addition, there are two spot welds that experience failure under the imposed excitation.

### 6.1.3 Findings related to the research objective IV

From the conducted quasi-static damage analysis of spot-welded specimens the following key findings emerge:

- The quasi-static response can be ensured based on the period of the first natural frequency. That is to say, the quasi-static response is generally obtained if the selected analysis duration is at least 3 to 5 times higher than the period of the first natural frequency, which ensures the conservation of energy. However, although the conservation of energy is ensured, the analysis models could experience significant plastic deformation. Therefore, a secondary evaluation criterion, which validates the stress and equivalent plastic strain distribution around the nugget circumference, is introduced.
- In the case of tensile shear specimen, all three spot weld models yield sufficiently accurate prediction of the failure initiation force ( $E_{\text{rel}} < 10\%$ ). The displacement at the failure initiation obtained using the connector element in combination with kinematic coupling is within the acceptable range ( $E_{\text{rel}} < 10\%$ ). However, both the mesh-independent fastener and the connector element in combination with the 'spider' of beam elements significantly overestimate the displacement at the failure initiation ( $E_{\text{rel}} > 10\%$ ). Moreover, the torsional and bending loading components make no significant contribution to the connector equivalent force. Therefore, the coupled force-based damage initiation criterion can be expressed in terms of the normal and shear loading components. The modified failure initiation criterion simplifies the analysis, simultaneously yielding sufficiently accurate prediction of the failure initiation force, whereas the displacement at the failure initiation is overestimated.

- In the case of coach peel specimen, numerically determined values of the failure initiation force are overestimated, although the displacement at failure initiation is estimated accurately. Due to the specimen geometry which tends to excessively deform, the experimental results are characterized by the contribution of plates to the global response. That is to say, due to the excessive deformation of sheet metals an additional amount of energy is dissipated during coach peel testing, as shown in Figure 5.31. Therefore, connector parameters defined using Arcan experimental testing yield the upper limit of the failure initiation force. Furthermore, both the torsional and shear loading components make no significant contribution to the connector equivalent force. Therefore, the coupled force-based damage initiation criterion can be expressed in terms of the normal and bending connector derived loading components. In addition, the modified failure initiation criterion simplifies the analysis, simultaneously yielding sufficiently accurate prediction of the displacement at damage initiation, whereas the damage initiation force is significantly overestimated. However, if the axial and shear stiffness optimized according to [70] are employed in the connector behavior definition, the estimated value of damage initiation force is significantly altered. That is to say, the damage initiation force is significantly lower, but it exceeds the acceptable limit ( $E_{\text{rel}} > 10\%$ ), whereas the relative difference between experimentally and numerically obtained value of the displacement at damage initiation is further reduced.

## 6.2 Recommendations for future work

Based on the findings of this thesis, the following recommendations for any potential continuation of this research are outlined:

- Since the fatigue life assessment using *FEMFAT Spot* is greatly influenced by the base material strength and the value of the restraint diameter, the effect of the aforementioned parameters should be further examined and verified based on experimental testing of different spot-welded specimens.
- The future research might be extended to develop and implement a coupled force-based damage initiation criterion for ACM. Thus, the same spot weld model could be used both in the fatigue and damage analysis.

- Further studies should investigate the possibility of simplifying the definition of connector element damage behavior, which will ensure sufficiently accurate prediction of the damage initiation.
- Due to the lack of the experimental data, the effect of the base material properties and the spot weld geometry on the failure initiation force was not investigated. Therefore, future investigations are necessary to correlate the failure initiation force with the base material properties, the weld nugget diameter and the sheet thickness.

# Bibliography

- [1] Khanna, S. K., Long, X. *Fatigue behavior of spot welded joints in steel sheets*, Failure Mechanisms of Advanced Welding Processes, Woodhead Publishing, 2010.
- [2] Saleem, J. *et al.*, *Nugget formation during resistance spot welding using finite element method*, World Academy of Science, Engineering and Technology 67, 2012.
- [3] Fukumoto, M. *et al.*, *Finite element simulation of resistance spot welding process*, International Body Engineering Conference & Exposition, 2003.
- [4] Wan, X. *et al.*, *Modeling the effect of welding current on resistance spot welding of DP600 steel*, Journal of Materials Processing Technology, 2014.
- [5] Hashemi, R. *et al.*, *An incrementally coupled thermo-electro-mechanical model for resistance spot welding*, Materials and Manufacturing Processes 27(12):1442-1449, 2012.
- [6] Moharrami, R., Hemmati, B., *Numerical stress analysis in resistance spot-welded nugget due to post-weld shear loading*, Journal of Manufacturing Processes, 2017.
- [7] Nodeh, I. R., *et al.*, *Simulation of welding residual stresses in resistance spot welding, FE modeling and X-ray verification*, Journal of Material Processing Technology, 2008.
- [8] Huh, H., Kang, W.J., *Electrothermal analysis of electric resistance spot welding processes by a 3-D finite element method*, Journal of Material Processing Technology, 2008.
- [9] Khan, A. J., *et al.*, *Numerical simulation of resistance spot welding process*, An International Journal of Computation and Methodology, 2010.
- [10] AHSS Data Utilization, <https://www.autosteel.orgg/research/ahss-data-utilization>
- [11] Nakayama, E. *et al.* *Fatigue strength prediction of spot-welded joints using small specimen testing*, Fracture of Nano and Engineering Materials and Structures, 2006.

- [12] Barkey, M. E., Zhang, S. *Spot weld fatigue*, A chapter in Fatigue Testing and Analysis: Theory and Application, Butterworth-Heinemann, 2004.
- [13] Gao, Y. *et al. Review of CAE fatigue analysis techniques for spot-welded high strength steel automotive structures*, SAE 2001 Transactions Journal of Materials & Manufacturing-V110-5
- [14] Bonnen, J. *et al. Fatigue of advanced high strength steel spot-welds*, Fatigue research & Application, 2006-SP-2013, SAE 2006 Transactions Journal of Material and Manufacturing V115-5
- [15] Baik, Y., *Spot weld modeling for vehicle durability performance with ANSA*, 4<sup>th</sup> ANSA &  $\mu$ ETA International Conference
- [16] Chamid, I. *et al., Critical nugget diameter of resistance spot welded stiffened thin plate structure*, Modern Applied Science, 2013.
- [17] JIS Z 3140:2017 *Method of inspection and acceptance levels for resistance spot welds*, Japanese Standards Association
- [18] Rupp, A. *et al. Computer aided dimensioning of spot-welded automotive structures*, SAE 1995 Transactions: Journal of Materials and Manufacturing-V104-5,
- [19] nCode DesignLife 2018, Theory Guide, HBM Prenscia
- [20] Zhang, G., Richter, B. *A new approach to the numerical fatigue-life prediction of spot-welded structures*, Fatigue & Fracture of Engineering Materials & Structures, 2008.
- [21] Nakahara, Y. *et al., Method of fatigue life estimation for spot-welded structures*, SAE 2000 World Congress, 2000.
- [22] Timoshenko, S., Woinowsky-Krieger, S., *Theory of plates and shell*, McGraw-Hill, 1989.
- [23] FEMFAT SPOT User Manual, Magna, 2017.
- [24] Dora-Fiskal, S., *Modelling and evaluation of spot weld using FEMFAT Spot Module*, Unpublished Internal Document, AVL List GmbH, Released on 1.10.2014.
- [25] Joseph, S. *et al., A mesh insensitive finite element spot-weld model*, Internationaler VDI-Kongress SIMVEC, 2014.

- [26] Palmonella, M. *et al.* *Finite element models of spot welds in structural dynamics: review and updating*, Computer & Structures, 2005.
- [27] Zhang, X., Kiu, B. *Strength analysis and simulation of multiple spot-welded joints*, Proceedings of the SEM Annual Conference, 2009.
- [28] Zhu, T. *et al.*, *Fatigue life prediction of spot-welded structure under different finite element models of spot-weld*, Advanced Materials Research Vols. 118-120, 2010.
- [29] Crombet, L., *Modeling of a Li-Ion battery pack for structural and crash loads*, Unpublished Internal Document, AVL List GmbH, Released on 7.7.2017.
- [30] Pandiyanayagam, G. *et al.*, *Experimental and modeling studies towards random vibration* SIAT 2011, 2011.
- [31] Liu, H. *et al.*, *Rolling bearing fault detection based on the teager energy operator and Elman neural network*, Mathematical Problems in Engineering, 2013.
- [32] Rahman, M. M. *et al.*, *Finite element based vibration fatigue analysis of a new two-stroke linear generator engine component*, International Journal of Mechanical and Materials Engineering, 2007.
- [33] Shin, K., Hammond, J., *Fundamentals of signal processing for sound and vibration engineers*, John Wiley & Sons, West Sussex, England, 2008.
- [34] Nieslony, A., Macha, E., *Spectral method in multiaxial random fatigue*, Lecture notes in Applied and Computational Mechanics, 2007.
- [35] Kumar, M. S., *Analyzing random vibration fatigue*, ANSYS Advantage, 2007.
- [36] FEMFAT Spectral User Manual, Magna, 2017.
- [37] Bishop, N. W. M, Sherratt, F., *Fatigue life prediction from power spectral density data*, Environmental Engineering, Vol 2, 1989.
- [38] Londhe, A. *et al.*, *Evaluation of vehicle systems structural durability using PSD based fatigue life approach*, SAE 2012 World Congress & Exhibition, 2012.
- [39] Su, H., *CAE virtual durability tests of automotive products in the frequency domain*, SAE 2008 World Congress & Exhibition, 2008.



- 
- [40] MathWorks Documentation, <https://nl.mathworks.com/help/signal/ug/power-spectral-density-estimates-using-fft.html>
- [41] Abaqus Analysis User's Guide, Dassault Systemes, 2016.
- [42] Teixeira, G. *et al.*, *Random vibration fatigue: Frequency domain critical plane approaches*, ASME International Mechanical Engineering Congress and Exposition, 2013.
- [43] Kong, Y. S. *et al.*, *Vibration fatigue analysis of carbon steel coil spring under various road excitations*, Fatigue & Fracture of Engineering Materials & Structures, 2003.
- [44] Teixeira, G. *Random vibration fatigue - A study comparing time domain and frequency domain approaches for automotive applications*, SAE 2014 World Congress & Exhibition, 2014.
- [45] Engin, Z., Coker, D., *Comparison of equivalent stress methods with critical plane approaches for multiaxial high cycle fatigue assessment*, Procedia Structural Integrity, Volume 5, 2017.
- [46] Carpinteri, A. *et al.*, *A multiaxial fatigue criterion for random loading*, Fatigue & Fracture of Engineering Materials & Structures, 2003.
- [47] Moura, A. *et al.*, *A review of spectral and conventional methods for cycle counting and fatigue life estimation. Extension to finite element analysis*, Proceedings of the 7th International Conference on Mechanics and Materials in Design, 2017.
- [48] Mršnik, M. *et al.*, *Frequency-domain methods for a vibration-fatigue-life estimation - Application to real data*, International Journal of Fatigue, Volume 47, 2013.
- [49] Quigley, J. P. *et al.*, *Review and assesment of frequency-based fatigue damage models*, SAE International Journal of Materials and Manufacturing-V125-5, 2016.
- [50] Halfpenny, A. *et al.*, *Vibration fatigue analysis of components on rotating machinery under sine and swept-sine-on-random loading*, HBM Prenscia, Technology Centre, 2017.
- [51] Halfpenny, A. *et al.*, *Frequency domain approach for fatigue life estimation from finite element analysis*, International Conference on Damage Assesment of Structures, 1999.
- [52] Du Bois, P. *et al.*, *Vehicle crashworthiness and occupant protection*, American Iron and Steel Institute, 2004.

- [53] Pouranvari, M., Marashi, S. P. H., *Key factors influencing mechanical performance of dual phase steel resistance spot welds*, Science and Technology of Welding and Joining, 2010.
- [54] Pouranvari, M., Marashi, S. P. H., *Effect of weld nugget size on overload failure mode of resistance spot welds*, Science and Technology of Welding and Joining, 2007.
- [55] Lin, S. H. et al., *Failure modeling of spot welds under complex loading conditions for crash applications*, International Body Engineering Conference & Exhibition and Automotive & Transportation technology Congress. 2002.
- [56] Radakovic, D. J., Tumuluru, M., *Predicting resistance spot weld failure modes in shear tension tests of advanced high-strength automotive steels*, Welding Journal, American Welding Society, 2008.
- [57] Khan, M. I. et al., *Effects of weld microstructure on static and impact performance of resistance spot welded joints in advanced high strength steels*, Science and Technology of Welding and Joining, 2008.
- [58] Wood, P., *Characterising spot weld behaviour in shear and tension for a range of sheet steels and gauges at low and high strain rates*, Conference: Annual International Workshop on Dynamic Behaviour of Structures and Materials, Interaction and Friction June 2011, ENIM, Metz, France
- [59] Chao, Y. J., *Ultimate strength and failure mechanism of resistance spot weld subjected to tensile, shear, or combined tensile/shear loads*, Journal of Engineering Materials and Technology, Volume 125, 2002.
- [60] Markiewicz, E. et al., *Material behaviour law identification for the various zones of the spot-weld under quasi-static loading*, International Journal of Materials and Product Technology 16(6-7), 2001.
- [61] Ha, J. et al., *Failure Characteristics of Spot Welds of AHSS under Quasi-static Conditions*, Experimental and Applied Mechanics, Volume 6, 2011.
- [62] Song, J. H. et al., *Effect of tensile speed on the failure load of a spot weld under combined loading conditions*, International Journal of Modern Physics B, 2008.

- [63] Yoda, S. *et al.*, *Development of a method to predict the rupture of spot welds in vehicle crash analysis*, Welding & Joining & Fastening Friction Stir Welding-SP-2034, SAE 2006 Transactions Journal of Passenger Cars: Mechanical Systems-V115-6, 2006.
- [64] Wung, P., *A force-based failure criterion for spot weld design*, Experimental Mechanics 41(1):107-113, 2001.
- [65] Wung, P., *A method for spot welded structure analysis*, Fatigue and Failure of Spot Welds and Weld Joints-SP-1621, 2001.
- [66] Hu. X. *et al.* *Comparison of explicit and implicit finite element methods in the quasi-static simulation of uniaxial tension*, Communications in Numerical Methods in Engineering, 1994.
- [67] Rusinski, E. *et al.*, *Tests of thin-walled beams joined by spot welding*, Journal of Materials Processing Technology, Volumes 157-158, 2004.
- [68] Al-Rifaie, A., *Quasi-static analysis of beam-to-column end plate connections*, International Journal of Civil, Environmental, Structural, Construction and Architectural Engineering, 2017.
- [69] Prior, A. M., *Applications of implicit and explicit finite element techniques to metal forming*, Journal of Materials Processing Technology, Volume 45, 1994.
- [70] Jones, N., *Quasi-static analysis of structural impact damage*, Journal of Constructional Steel Research, Volume 33, 1995.
- [71] Markiewicz, E. *et al.*, *Macro-modeling of spot weld strength and failure: Formulation and identification procedure based on pure and mixed modes of loading*, Engineering Computations, 2017.
- [72] Weyer, S. *et al.*, *Modeling of self-piercing rivets using fasteners in crash analysis*, Abaqus User's Conference, 2006.
- [73] Combescure, A. *et al.*, *A 'global' finite element model for the simulation of failure of spot welded assemblies during impact*, Computational Fluid and Solid Mechanics, 2003.
- [74] Timoshenko, S. P., *History of Strength of Materials: With a Brief Account of the History of Theory of Elasticity and Theory of Structures*, Dover Publications, Inc, New York, 1953.

# A Appendix: Effect of spot weld model, mesh refinement and mesh alignment on fatigue behavior of spot-welded specimens

The Rupp/LBF method originally requires spot welds to be represented with a stiff bar or beam element directly connected to the shell element nodes (so-called Point to point method), which generally causes singularity of forces and moments transferred through the weld nugget [18, 19]. Moreover, Point to point method is mesh-dependent, i.e. since the beam/bar element has to be perpendicular to the shell mesh, this type of connection requires congruent shell meshes. Due to the recent developments, *nCode DesignLife* and *FEMFAT Spot* support various FE spot weld models, including ACM and beam elements connected to the shell mesh via coupling elements. Since *nCode DesignLife* and *FEMFAT Spot* documentation recommend that the spot-welded sheets are discretized using rectangular, coarse shell element meshes, a series of FE models with different mesh densities and mesh alignment was generated, as shown in Figure A.1 and Figure A.2. Simultaneously with analyzing the effect of the mesh refinement and the mesh alignment, the effect of the spot weld model representation was as well examined. Three different FE models were created (Figure 3.1). However, only *FEMFAT Spot* supports the connection of B31 element representing the weld nugget to surrounding shell elements via 'spider' of B31 elements.

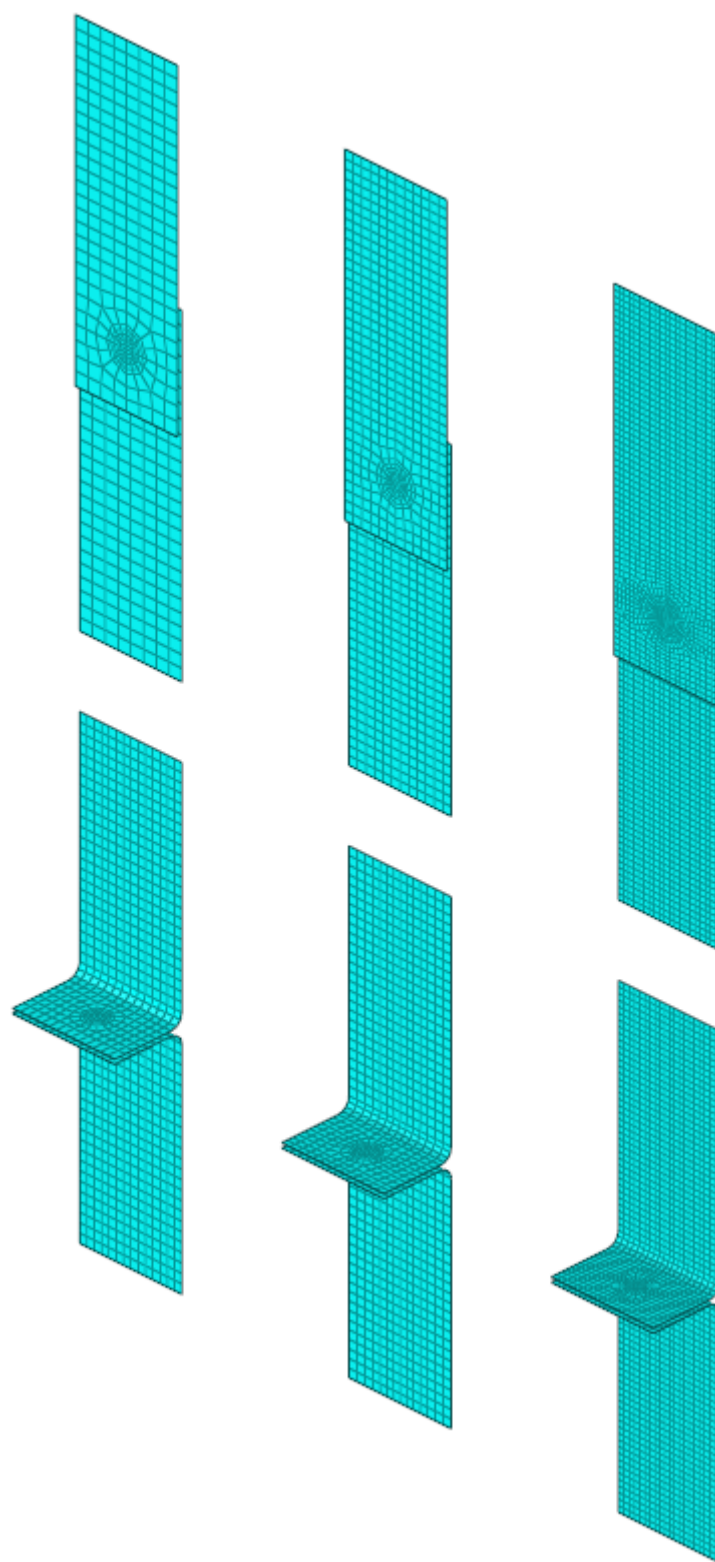
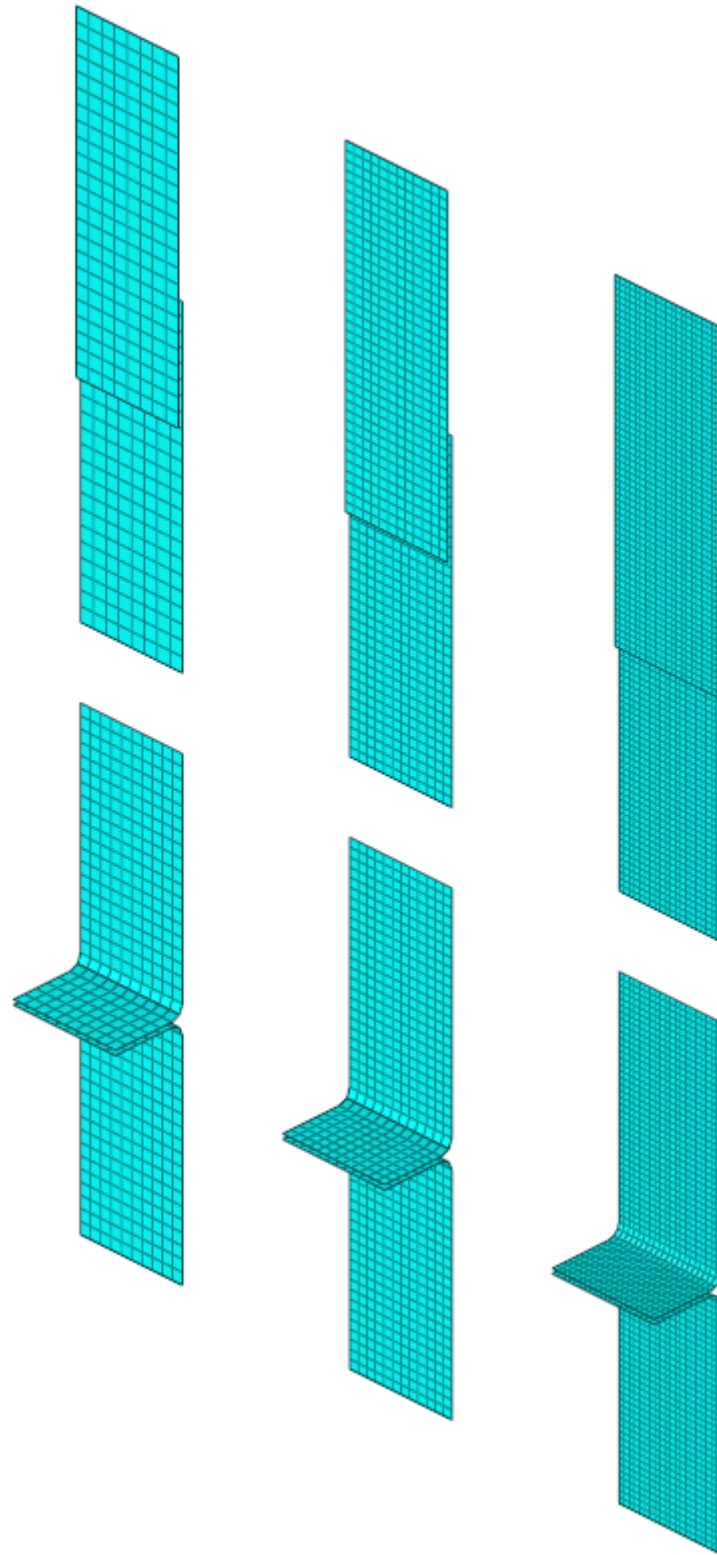


Figure A.1: Specimen FE model: Effect of mesh refinement around the nugget perimeter



**Figure A.2: Specimen FEA model: Rectangular shell element meshes**

Moreover, Table A.1 displays the results of the fatigue life evaluation of tensile shear specimen with respect to the shell element size for the load amplitude  $F_a=1800$  N obtained using *nCode DesignLife*.

**Table A.1:** The effect of mesh refinement around the nugget circumference on the fatigue life of tensile shear specimen using *nCode DesignLife*

<b>Mesh<sup>22</sup></b>	<b>Spot model</b>	<b>B31+ kinematic coupling</b>	<b>ACM</b>
M5		254200	255600
M3		244700	244600
M2		244300	240200

The following table displays the comparison between the results obtained using M5 and M2 finite element meshes.

**Table A.2:** Comparison of obtained results (*nCode DesignLife*)

<b>Mesh</b>	<b>Number of cycles to failure</b>	<b><math>E_{\text{rel}}</math></b>
M5 B31+KIN_COUP	254200	-
M2 B31+KIN_COUP	244300	4.05%
M5 ACM	255600	-
M2 ACM	240200	6.41%

Table A.3 displays the effect of mesh refinement on the fatigue life of tensile shear specimen in the case of rectangular shell mesh, whereas Table A.4 shows the comparison of obtained results. The analysis is performed for the load amplitude equal to 1800 N.

**Table A.3:** The effect of mesh alignment on the fatigue life of tensile shear specimen using *nCode DesignLife*

<b>Mesh<sup>23</sup></b>	<b>Spot model</b>	<b>B31+ kinematic coupling</b>	<b>ACM</b>
M5R		256000	266400
M3R		243000	264900
M2R		242800	244400

**Table A.4:** Comparison of obtained results (*nCode DesignLife*)

<b>Mesh</b>	<b>Number of cycles to failure</b>	<b><math>E_{\text{rel}}</math></b>
M5R B31+KIN_COUP	256000	-
M2R B31+KIN_COUP	242800	5.43%
M5R ACM	266400	-
M2R ACM	244400	9.18%

<sup>22</sup>M5 refers to approximate element size of 5 mm, whereas M3 and M2 refer to approximate shell element sizes of 3 mm and 2 mm.

<sup>23</sup>R refers to rectangular mesh alignment.

Since the relative difference between the obtained results does not exceed 10%, it is concluded that the force-based approach implemented in *nCode DesignLife* is insensitive to mesh refinement. Moreover, Table A.5 display the comparison of the results obtained using M5 and M5R shell mesh.

**Table A.5: Comparison of obtained results (*nCode DesignLife*)**

Mesh	Number of cycles to failure	$E_{\text{rel}}$
M5 B31+KIN_COUP	254200	-
M5R B31+KIN_COUP	256000	-0.7%
M5 ACM	255600	-
M5R ACM	266400	-4.5%

As evident, the force-based fatigue life assessment method implemented in *nCode DesignLife* is insensitive both to mesh refinement and mesh alignment. In addition, the following table displays the comparison between the results obtained using B31+KIN\_COUP and ACM.

**Table A.6: Comparison of obtained results (*nCode DesignLife*)**

Mesh	Number of cycles to failure	$E_{\text{rel}}$
M5R B31+KIN_COUP	256000	-
M5R ACM	266400	-3.9%

Since the relative difference between the obtained results does not exceed 10%, it is concluded that the force-based method implemented in *nCode DesignLife* is insensitive to spot weld finite element representation.

Furthermore, the following table displays the results of the force-based fatigue life evaluation of coach peel specimen with respect to the shell element size for the load amplitude  $F_a=225$  N obtained with *FEMFAT Spot*.

**Table A.7: The effect of mesh refinement around the nugget circumference on the fatigue life of coach peel specimen using *FEMFAT Spot***

Spot model Mesh	B31+ kinematic coupling	B31+ 'spider' of B31 elements	ACM
M5	323101	368731	310645
M3	301400	364211	294456
M2	301233	362564	292122



Moreover, Table A.8 shows the comparison between the results obtained using M5 and M2 finite element meshes.

**Table A.8: Comparison of obtained results (*FEMFAT Spot* force-based approach)**

Mesh	Number of cycles to failure	$E_{\text{rel}}$
M5 B31+KIN_COUP	323101	-
M2 B31+KIN_COUP	301233	7.25%
M5 B31+'spider' of B31	368731	-
M2 B31+'spider' of B31	362564	1.7%
M5 ACM	310645	-
M2 ACM	292122	9.42%

Furthermore, Table A.9 displays the effect of mesh alignment on the fatigue life of coach peel specimen in the case of rectangular shell mesh, whereas Table A.10 shows the comparison of obtained results. The analysis is performed for the load amplitude equal to 225 N using the force-based method implemented *FEMFAT Spot*.

**Table A.9: Effect of mesh alignment on fatigue life of coach peel specimen (*FEMFAT Spot* force-based approach)**

Spot model Mesh	B31+ kinematic coupling	B31+ 'spider' of B31 elements	ACM
M5R	312109	342367	287626
M3R	297265	339871	283446
M2R	293858	339253	282008

**Table A.10: Comparison of obtained results (*FEMFAT Spot* force-based approach)**

Mesh	Number of cycles to failure	$E_{\text{rel}}$
M5R B31+KIN_COUP	312109	-
M2R B31+KIN_COUP	293858	6.21%
M5 B31+'spider' of B31	342367	-
M2 B31+'spider' of B31	339253	0.91%
M5R ACM	287626	-
M2R ACM	282008	1.99%

As evident, the force-based fatigue life assessment method implemented in *FEMFAT Spot* is insensitive both to mesh refinement. In addition, the following table displays the comparison between the results obtained using M5R and M5 shell element meshes.

Table A.11: Comparison of obtained results (*FEMFAT Spot* force-based approach)

Mesh	Number of cycles to failure	$E_{\text{rel}}$
M5 B31+KIN_COUP	323101	-
M5R B31+KIN_COUP	312109	3.52%
M5 B31+'spider' of B31	368721	-
M5R B31+'spider' of B31	342367	7.7%
M5 ACM	310645	-
M5R ACM	287626	8%

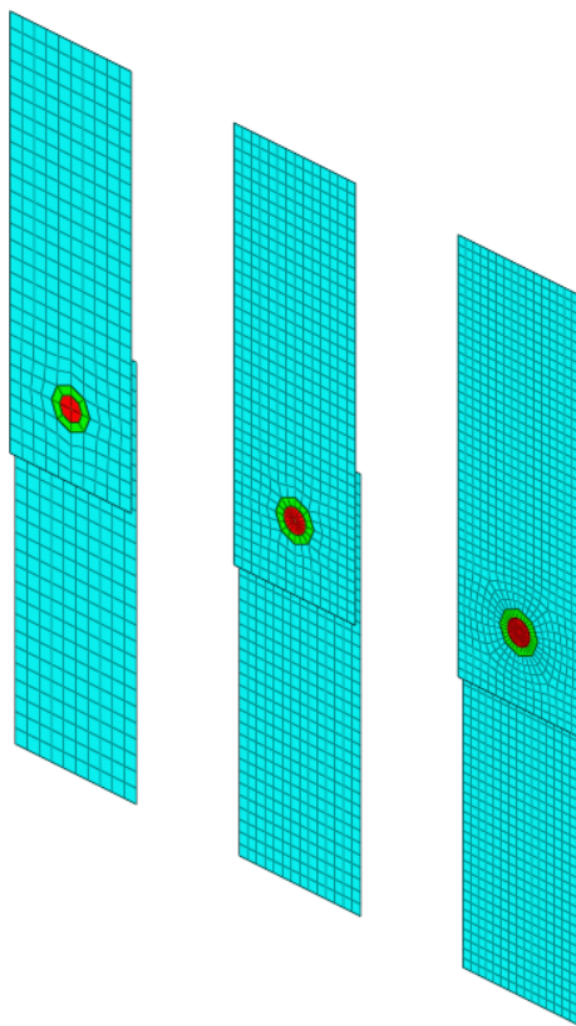
As evident, the force-based fatigue life assessment method is insensitive to mesh alignment. Moreover, the following table displays the effect of spot weld finite element representation in *FEMFAT Spot*. It is important to emphasize that the results obtained using both B31+KIN\_COUP and B31+'spider' of B31 elements are compared to the results obtained using ACM.

Table A.12: Comparison of obtained results (*FEMFAT Spot* force-based approach)

Mesh	Number of cycles to failure	$E_{\text{rel}}$
M5R ACM	287626	-
M5R B31+KIN_COUP	312109	-7.8%
M5R B31+'spider' of B31	342367	-15.9%

As evident, when comparing the fatigue results obtained using ACM and B31+KIN\_COUP, the relative difference does not exceed 10%. However, the relative difference between the results obtained using ACM and B31+'spider' of B31 exceeds 10%. Thus, it is concluded that the spot weld model representation has a greater influence on the force-based fatigue life prediction using *FEMFAT Spot* compared to the fatigue life prediction with *nCode DesignLife*.

Furthermore, the effect of mesh refinement on the stress-based fatigue life prediction implemented in *FEMFAT Spot* was evaluated, whereas Figure A.3 shows different finite element meshes used in the analysis.



**Figure A.3: Specimen FE model: Effect of mesh refinement around the nugget circumference**

The von Mises stress values and corresponding number of cycles to failure with respect to the number of shell elements in the outer row for  $F_{max}=6700$  N are listed in Table A.13, whereas Figure A.4 graphically displays the convergence of the von Mises stress.

**Table A.13: Effect of mesh refinement on the stress-based fatigue life prediction of tensile shear specimen**

Number of S4R	$\sigma_{MISES}$ , MPa	Cycles to failure
8	311.475	369003
16	366.648	234246
32	375.863	210386

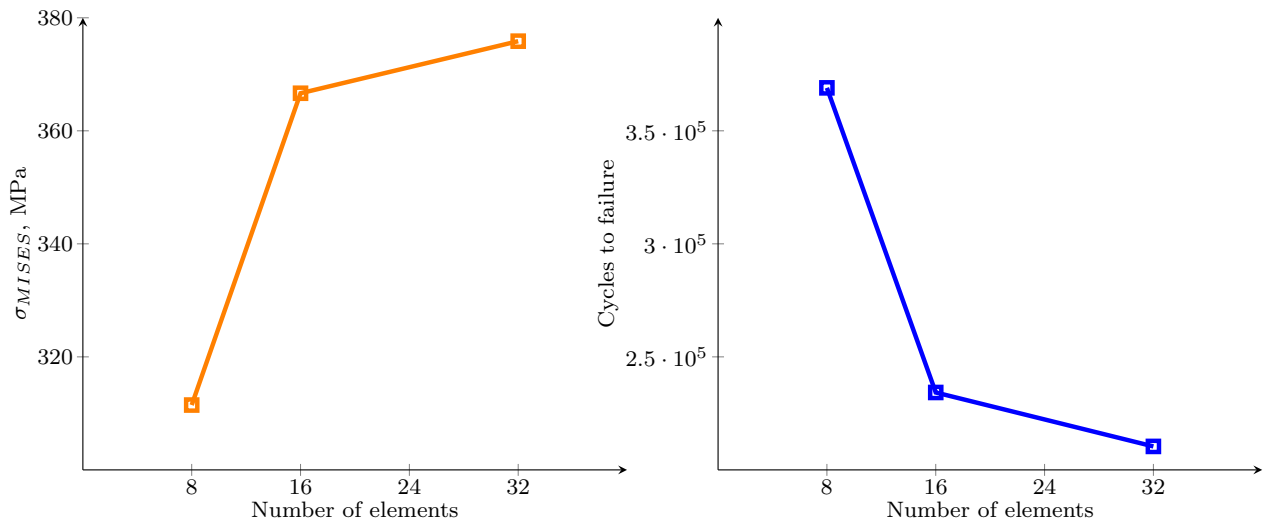


**Figure A.4: Effect of mesh refinement on the stress-based fatigue life prediction**

As evident, the decrease of shell element size leads to the increase of von Mises stress and thus the decrease of the number of cycles to failure. Therefore, the size of the outer row shell elements has a significant impact on the stress-based fatigue life prediction of spot-welded structures. To summarize, the presented results lead to the following conclusions:

- The force-based approach implemented in *nCode DesignLife* is insensitive to mesh alignment, mesh refinement and the spot weld model representation.
- The force-based fatigue life assessment implemented in *FEMFAT Spot* is insensitive to mesh refinement and mesh alignment. However, the performed research leads to the conclusion that the spot weld finite element representation has a greater influence on the predicted fatigue life using *FEMFAT Spot* compared to *nCode DesignLife*
- The stress-based approach implemented in *FEMFAT Spot* is greatly influenced by the shell element size. That is to say, the decrease of shell element size leads to the increase of von Mises stress and thus the decrease of the number of cycles to failure.

## B Appendix: Effect of restraint diameter in *FEMFAT Spot*

Compared to the Rupp/LBF method, the force-based fatigue life assessment method implemented in *FEMFAT Spot* offers the possibility to change the value of restraint diameter  $D$  of the circular plate. The default value of restraint diameter  $D$  in *SPOT Database*<sup>24</sup> is equal to 42 mm. However, *FEMFAT Spot* recommends the modification of restraint diameter depending on the geometric characteristics of the observed structures [23]. Therefore, the effect of restraint diameter is evaluated. For analysis purposes, the nominal weld diameter is equal to 7 mm, whereas the nominal sheet thickness is equal to 1.6 mm. Figure B.1 displays the effect of restraint diameter on the fatigue behavior of spot-welded specimens.

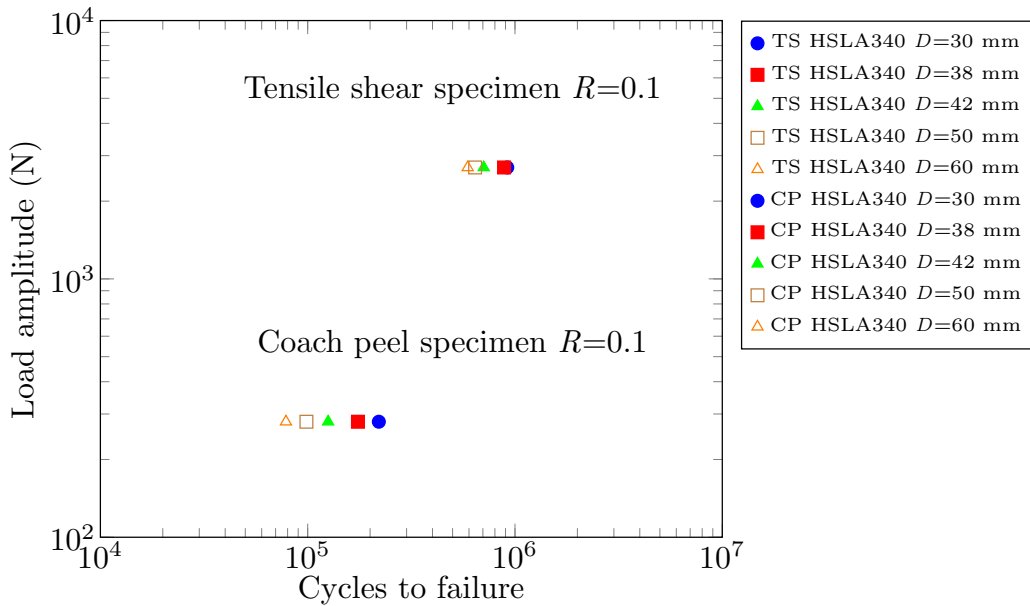


**Figure B.1: Effect of restraint diameter on the fatigue life of spot-welded specimens**

As evident, the increase of restraint diameter leads to the overestimated structural stresses and thus the conservative results.

<sup>24</sup>*SPOT Database* provides the basic interrelations essential for the preprocessing and durability analysis of spot-welded structures. Moreover, *SPOT Database* can be customized to suit specific application requirements.